# Terahertz Laser Radiation Induced Opto-Electronic Effects in HgTe Based Nanostructures

DISSERTATION

zur Erlangung des Doktorgrades der Naturwissenschaften

doctor rerum naturalium

(Dr. rer. nat.)

Fakultät für Physik

Universität Regensburg

vorgelegt von

Dipl.-Phys. Christina Zoth

aus Göttingen

im Jahr 2014

Die Arbeit wurde von Prof. Dr. Sergey D. Ganichev angeleitet.

Das Promotionsgesuch wurde am 11. Juni 2014 eingereicht.

**Prüfungsausschuss:**

| | |
|---|---|
| Vorsitzender: | Prof. Dr. Gunnar S. Bali |
| 1. Gutachter: | Prof. Dr. Sergey D. Ganichev |
| 2. Gutachter: | Prof. Dr. Christian Schüller |
| weiterer Prüfer: | Prof. Dr. Thomas Niehaus |

# Contents

# 1 Introduction

The spin of electrons and holes in solid state systems attracts growing attention in modern research. This is stimulated by the hope that the spin degree of freedom in semiconductor systems can be utilized for new spin based electronics, namely *spintronics* [1, 2]. The success of spintronics depends on the ability to create, manipulate and detect, as well as to transport and store spin orientations [3]. Possibilities of spin manipulation are e.g., the application of light or an electric field to a semiconductor heterostructure. A promising physical effect which can be exploited for this kind of spin manipulation is the spin orbit interaction [4, 5]. Therefore, semiconductors which are characterized by a strong spin orbit interaction form a suitable system for spintronic applications [6].

A very promising candidate is mercury telluride, which has recently advanced into the focus of condensed matter research. In particular, the strong spin orbit interaction in mercury telluride is responsible for its unique energy spectrum yielding very fascinating effects [7–13]. Herein, without changing the material it is possible to obtain an inverted and normal parabolic band structure, as well as a linear one. The latter state is described by the Dirac theory of massless fermions [12]. In mercury telluride this Dirac-like dispersion can be realized in different manners: either by layered quantum well structures with a characteristic quantum well width or in topological insulator systems. The main difference lies in the spin degeneracy of the Dirac cone and the topology of the band structure in real space. In the former case the linear band structure is formed by unpolarized two dimensional Dirac fermions. This state is not bound to any spatial limitation [13–15]. In case of topological insulators the Dirac states only emerge at the edges or on the surface of a two or three dimensional mercury telluride system, respectively. Furthermore the states demonstrate a spin polarization [10]. This gives rise to the existence of dissipationless spin polarized transport along the one dimensional edge channels or the two dimensional surface states, as back scattering with spin flip is prohibited [10, 12, 16].

An interesting and powerful access to the study of spin related phenomena is provided by opto-electronic techniques. In particular, using radiation in the terahertz range the observation of effects of carrier redistribution in momentum space becomes possible e.g., photogalvanic effects [17]. Moreover, the measurements of opto-electronic effects build a bridge between the two fields of transport and optical phenomena [1]. The fundamental theory of these phenomena e.g., photogalvanic effects, photoconductivity or quantum transport are introduced in Chapter 2. Chapter 3 contains details about the experimental setup and gives an overview of the investigated samples.

The observation and study of the terahertz radiation induced magnetogyrotropic photogalvanic effect in various mercury telluride quantum well systems forms the core of this thesis. Herein several new phenomena are observed. In order to understand this opto-electronic and spin dependent effect, results for a well established semiconductor system will be presented in advance as this will substantially help to understand the observations for the mercury telluride structures. For this purpose quantum well structures based on cadmium telluride and indium arsenide with a diluted amount of magnetic manganese are investigated [18,19]. The results will be illustrated and discussed in Chapter 4.

In Chapters 5 and 6 the results of the opto-electronic measurements on mercury telluride based quantum well nanostructures are presented. In the scope of this thesis, the first investigations of cyclotron resonance assisted photocurrents and photoresistance on a Dirac fermion system are performed: the results which are presented and discussed in Chapter 5 for a mercury telluride sample with the critical quantum well width give experimental proof that the structure under investigation is indeed characterized by a Dirac-like energy spectrum [14, 15]. It is shown that nonlinear transport experiments can be utilized to probe the dispersion of two dimensional Dirac fermions.

Moreover, oscillations in the terahertz induced cyclotron resonance assisted photocurrent and photoresistance are observed for all types of band structure, namely for normal and inverted parabolic, as well as linear [20]. These oscillations are induced by the variation of an external magnetic field. The corresponding experimental observations are presented in Chapter 6. It will be demonstrated that they originate from the crossing of the Fermi level with

Landau levels. This consecutive crossing results in the oscillations of spin polarization and electron mobilities in the spin subbands (cones), which are related to the de Haas-van Alphen and Shubnikov-de Haas effect.

Finally, Chapter 7 gives a conclusion of the main outcome of this work.

# 2 Theoretical Basics

This thesis is devoted to mercury telluride (HgTe), in particular to effects concerning the special band structure of the material. Therefore, it is crucial to understand the main characteristics of the dispersion and its dependency on the width of the HgTe layer. These relations will be introduced in the first section of this chapter as a simplified model of band ordering. The HgTe samples are investigated by means of high frequency nonlinear opto-electronic phenomena, namely terahertz induced photogalvanic and photoconductivity effects. Hence, the following section will also depict the fundamental model of photocurrent generation in parabolic semiconductor quantum well structures which is based on an asymmetric spin dependent distribution of a charge carrier ensemble in momentum space. Additional effects induced by terahertz radiation are photoconductivity and cyclotron resonance, which will be introduced in the third and forth section of this chapter. For interpretation and analysis of the experimental results given in Chapters 5 and 6 quantum transport phenomena are needed. Therefore, the last section will illustrate the Shubnikov-de Haas and de Haas-van Alphen effect.

## 2.1 Band Structure of Mercury Telluride

HgTe belongs to the group of II-VI semiconductors and crystallizes in zinc-blende structure [21]. In quantum well (QW) structures, sandwiched between layers of cadmium telluride (CdTe), HgTe features an unique and very interesting dispersion, which can be influenced in an extraordinary way. While the conduction band of bulk CdTe is formed by $s$-states located at the group II atoms and the valence band by $p$-states at the group VI atoms, the situation for bulk HgTe is vice versa, yielding an inverted band ordering around the $\Gamma$ point of the Brillouin zone [12, 22]. This effect of an inverted band structure is induced by the strong spin orbit interaction in this material [22, 23] and is depicted in Fig. 1. For bulk CdTe the $\Gamma_6$ band is $s$-type and lays energetically above the $p$-type $\Gamma_8$ bands. These present conduction and valence band, respectively. In case of bulk HgTe the picture is quite different: the $p$-type $\Gamma_8$ bands and the $s$-type $\Gamma_6$ band are inverted compared to bulk CdTe. The
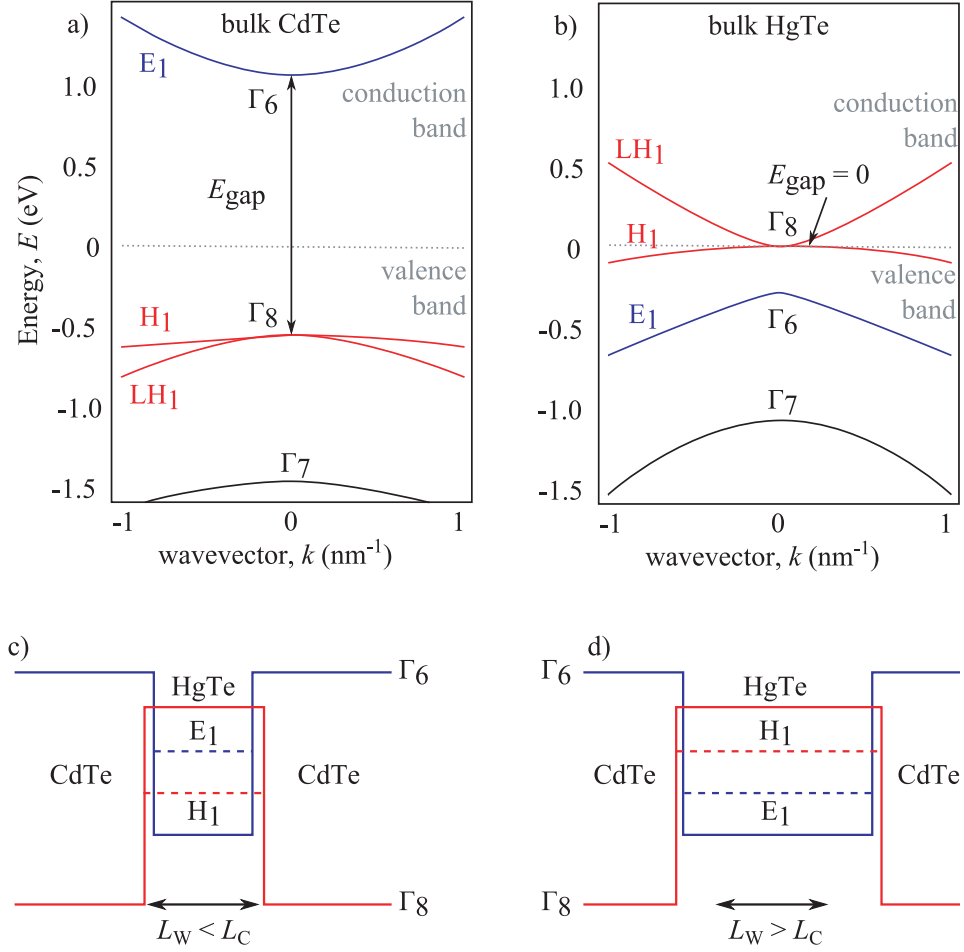
**Figure 1:** Energy spectrum of (a) bulk CdTe with a normal band ordering and band gap $E_{gap}$, as well as of (b) bulk HgTe with an inverted band ordering and zero band gap between valence and conduction band, $H_1$ and $LH_1$, respectively. The band ordering for CdTe/HgTe QWs is depicted in (c) and (d): for QW widths $L_W$ smaller than the critical width $L_C$ the electronic structure is normal, whereas in case of $L_W > L_C$ it is inverted. Picture according to Ref. [11].

conduction and valence band consist of the light hole band $LH_1$ and the heavy hole band $H_1$ of the $\Gamma_8$ bands and yield a zero gap system [18].

In HgTe based heterostructures this band ordering changes compared to the HgTe bulk material. Due to confinement effects $LH_1$ and $H_1$ are separated by an energy gap and conduction and valence band are now formed of the heavy

hole $H_1$ and the electron $E_1$ band [22]. According to Ref. [11] only these two spin degenerated bands $E_1\pm$ and $H_1\pm$ are relevant, as they are close to the Fermi energy.

The corresponding effective Hamiltonian near the $\Gamma$ point is given by

$$
\begin{aligned}
H_{eff}\,(k_x, k_y) &= \begin{pmatrix} H(k) & 0 \\ 0 & H^*(-k) \end{pmatrix} \\
H &= \epsilon(k) + d_i(k)\sigma_i,
\end{aligned}
\tag{1}
$$

where $\sigma_i$ are the Pauli matrices and

$$
\begin{aligned}
d_1 + id_2 &= A(k_x + ik_y), \\
d_3 &= M - B(k_x^2 + k_y^2), \\
\epsilon_k &= C - D(k_x^2 + k_y^2).
\end{aligned}
\tag{2}
$$

Here $k_x$ and $k_y$ are momenta in the plane of the two dimensional electron gas and $A, B, C$ and $D$ are material specific constants. $M$ is the Dirac mass parameter, indicating the order of bands. In conventional semiconductors e.g., CdTe, this parameter $M$ is positive ($E_1$ lays over $H_1$). However, for HgTe having an inverted band structure ($H_1$ lays over $E_1$) this parameter is negative. Hence, in HgTe/CdTe QW structures the Dirac mass parameter $M$ can be tuned from positive to negative values simply by varying the QW width $L_W$. At a special QW width $L_C$ the mass parameter $M$ is zero and a topological quantum phase transition occurs, where the system merges from normal to inverted band ordering. At this point the structure is characterized by the Dirac equation for massless particles [12]. This dependency of $E_1$ and $H_1$ on the QW width $L_W$ is shown in Fig. 2 (a). Figure 1 (c) and (d) show the positions of the two bands ($H_1$ and $E_1$) in a CdTe/HgTe QW for $L_W$ smaller and larger than the critical width $L_C$. In the former case the band ordering of CdTe dominates, consequently the band structure is normal, whereas in the latter the bands have the ordering of HgTe, namely an inverted band structure. Note, that the band ordering can additionally be tuned by temperature and strain for bulk and two dimensional HgTe structures, as well as by the fraction $x$ in $Hg_{1-x}Cd_xTe$ crystals, for review see Ref. [22, 24–26]. At the touching point of

the bands $E_1$ and $H_1$, indicated in Fig. 2 (a), the electronic structure of the system is formed by a mixture of the two bands and shows a linear dispersion. This so-called Dirac cone is depicted in Fig. 2 (b), where the colors indicate the mixing of bands. A red shading stands for a dominant $H_1$ state, whereas in blue regions the dominant state is $E_1$. Purple shading is a mixture of both. According to Refs. [11, 15] the Dirac cone is formed by the four states

$$
\begin{aligned}
|E1, +1/2\rangle &= f_1(z)\,|\Gamma_6, +1/2\rangle + f_4(z)\,|\Gamma_8, +1/2\rangle\,, \\
|H1, +3/2\rangle &= f_3(z)\,|\Gamma_8, +3/2\rangle\,, \\
|E1, -1/2\rangle &= f_1(z)\,|\Gamma_6, -1/2\rangle + f_4(z)\,|\Gamma_8, -1/2\rangle\,, \\
|H1, -3/2\rangle &= f_3(z)\,|\Gamma_8, -3/2\rangle\,,
\end{aligned}
\tag{3}
$$

where $f_1(z)$, $f_3(z)$ and $f_4(z)$ are the envelope functions, $z$ is the growth direction, $|\Gamma_6, \pm 1/2\rangle$, $|\Gamma_8, \pm 1/2\rangle$ and $|\Gamma_8, \pm 3/2\rangle$ are the basis functions of the $\Gamma_6$ and $\Gamma_8$ band. These are degenerated for $k = 0$, and are coupled by an effective
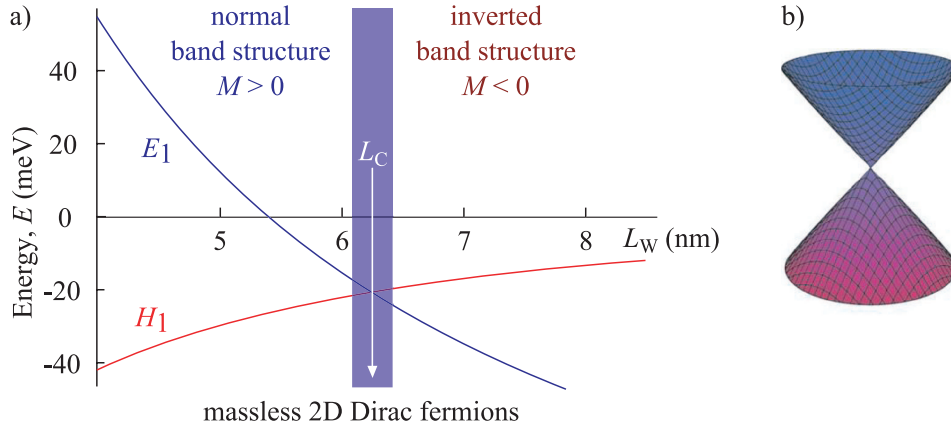


**Figure 2:** (a) Energy of the $E_1$ and the $H_1$ band depending on the QW width $L_W$ with the crossing point of bands at $L_W = L_C$. At this point the band structure is characterized by a linear behavior, where two dimensional massless Dirac fermions are predicted to occur. (b) shows the Dirac cone for the critical width $L_C$. Colors indicate the mixing of bands: while red stands for a dominant $H_1$ state, blue corresponds to the $E_1$ state. Shades in between (purple) indicate a mixture of both. Picture according to Ref. [11].

Hamiltonian at $k \neq 0$. Consequently, the spin-up and -down bands are formed by a mixture of the different states of Eq. (3).

This Dirac-like dispersion can be achieved in different HgTe based systems. The main subject of Chapter 5 is this linear band structure which has its origin in the critical QW width $L_C$. Another possibility is provided by quantum phase transitions at the interface of HgTe to materials with normal band structure. In case of a two dimensional system a Dirac-like dispersion arises at the edges, whereas for three dimensional systems it occurs at the surfaces of HgTe. These systems with edge and surface states belong to the class of topological insulators, where dissipationless transport is possible by the mentioned states. As topological insulators are not the subject of this thesis, their properties will not be illustrated in more detail. For review see Refs. [10, 12].

## 2.2  Photogalvanic Effects

Terahertz (THz) radiation induced effects are very useful and efficient for the investigation of semiconductor structures [17]. The photon energy in this spectral range is much smaller than the energy gap of conventional semiconductors. Hence, no free carriers are generated across the band gap by absorption of photons. As a consequence, effects based on the redistribution of carriers in momentum space are observable. This redistribution results in a *dc* electric current without external bias [17]. An example are THz radiation induced photocurrents. Phenomenologically it is convenient to describe such *dc* currents by writing the coordinate and time dependent electric current density $\boldsymbol{j}(\boldsymbol{r}, t) = \sigma \boldsymbol{E}(\boldsymbol{r}, t)$ as an expansion of powers of the electric field

$$\boldsymbol{E}(\boldsymbol{r}, t) = \boldsymbol{E}(\omega, \boldsymbol{q})e^{-i\omega t + i\boldsymbol{qr}} + \boldsymbol{E}^*(\omega, \boldsymbol{q})e^{i\omega t - i\boldsymbol{qr}}, \tag{4}$$

at radiation frequency $\omega$ and photon wavevector $\boldsymbol{q}$ as [27]:

$$
\begin{aligned}
j_\alpha(\boldsymbol{r}, t) = {} & \left[ \sigma_{\alpha\beta}^{(1)} E_\beta(\omega, \boldsymbol{q}) e^{-i\omega t + i\boldsymbol{qr}} + c.c. \right] \\
& + \left[ \sigma_{\alpha\beta\gamma}^{(2')} E_\beta(\omega, \boldsymbol{q}) E_\gamma(\omega, \boldsymbol{q}) e^{-2i\omega t + 2i\boldsymbol{qr}} + c.c. \right] \\
& + \sigma_{\alpha\beta\gamma}^{(2)} E_\beta(\omega, \boldsymbol{q}) E_\gamma^*(\omega, \boldsymbol{q}) + ....
\end{aligned}
\tag{5}
$$

Herein, Greek indices are Cartesian coordinates and *c.c.* stands for the complex conjugate. Eq. (5) is limited to second order effects only. While the first term on the right-hand side describes the linear transport, the second and third term refer to second order electric field effects: the former term is responsible for second harmonic generation, the latter one for time independent contributions, which yield *dc* currents in response to the radiation's *ac* electric field. The first two terms are out of scope of this thesis which deals with nonlinear transport phenomena proportional to the square of the electric field ($\propto E_\beta(\omega, \boldsymbol{q})E_\gamma^*(\omega, \boldsymbol{q})$). The lowest order of non vanishing terms for the current density $\boldsymbol{j}$ relevant for the experimental observations of this thesis is given by [17]

$$j_\lambda = \sum_{\mu,\nu} \chi_{\lambda\mu\nu} E_\mu E_\nu^*, \tag{6}$$

where $E_\nu^* = E_\nu^*(\omega) = E_\nu(-\omega)$ is the complex conjugate of $E_\nu$ and $\boldsymbol{\chi}$ is a third rank tensors. Equation (6) corresponds to the photogalvanic effect (PGE), whose sum on the right-hand side can be also written with $E_\mu E_\nu^*$ as a sum of symmetric and antisymmetric product

$$E_\mu E_\nu^* = \{E_\mu E_\nu^*\} + [E_\mu E_\nu^*], \tag{7}$$

yielding the photocurrent density to

$$j_\lambda = \sum_{\mu,\nu} \chi_{\lambda\mu\nu} \{E_\mu E_\nu^*\} + \sum_{\mu,\nu} \chi_{\lambda\mu\nu}[E_\mu E_\nu^*]. \tag{8}$$

The photogalvanic effect is decomposed into the linear and circular photogalvanic effect (LPGE and CPGE), given by the first and second sum on the right-hand side.

By applying an external magnetic field $\boldsymbol{B}$, all the characteristic features of the LPGE and CPGE change and new phenomena arise e.g., the magnetogyrotropic photogalvanic effect (MPGE). This effect will be introduced in the following, as it is the relevant mechanism of current generation for almost all findings presented in the experimental Chapters 4 to 6 of this thesis. It will be discussed briefly with the help of a simplified phenomenological description and then on the basis of a microscopic model.

Within the linear approximation of the magnetic field strength $\boldsymbol{B}$, the current density for the magnetic field induced photocurrent is given by [28, 29]

$$j_\alpha = \sum_{\beta,\gamma,\delta} \phi_{\alpha\beta\gamma\delta} B_\beta \left\{ E_\gamma E_\delta^* \right\} + \sum_{\beta,\gamma} \mu_{\alpha\beta\gamma} B_\beta \hat{e}_\gamma E^2 P_{circ}. \tag{9}$$

Here, the fourth rank pseudotensor $\boldsymbol{\phi}$ is symmetric in the last two indices and $\boldsymbol{\mu}$ is a third rank tensor. The first sum on the right-hand side is induced by linear components of radiation and even by unpolarized light, whereas the second sum requires circularly polarized radiation. This effect only occurs in gyrotropic media which are characterized by the lack of inversion symmetry and where nonzero components of third rank tensors exist [17, 30, 31]. Gyrotropic media have second rank pseudotensors as invariants. This means that the gyrotropic point group symmetry does not distinguish between polar vectors e.g., current or electron momentum and axial vectors e.g., magnetic field or spin [30]. This is the case for quantum well structures based on zinc-blende semiconductors e.g., HgTe QWs.

Besides this phenomenological description, the MPGE can also be explained by a microscopic model. Starting point is an electron gas homogeneously heated up by Drude absorption of THz radiation. In gyrotropic media the electron-phonon interaction contains an additional, asymmetric spin dependent term and is given by [5]

$$V_{kk'} = V_0 + \sum_{\alpha,\beta} V_{\alpha\beta} \sigma_\alpha (k_\beta + k_\beta'), \tag{10}$$

where $V_0$ describes the conventional spin independent scattering. $\boldsymbol{V}$ is a second rank pseudotensor, $\sigma_\alpha$ represents the Pauli matrices and $\boldsymbol{k}$ ($\boldsymbol{k'}$) is the initial (scattered) wavevector. Note, that microscopically this additional term which is proportional to $\sigma_\alpha(k_\beta + k_\beta')$ has the same origin as the structure and bulk inversion asymmetry [6, 32–34]. This asymmetry in the electron-phonon interaction results in nonequal relaxation rates for positive and negative wavevectors within one energy subband. This is depicted in Fig. 3 (a) and (b) for the spin-down and -up subband. The difference in the arrows' thickness corresponds to the probability $W_{kk'} \propto |V_{kk'}|^2$ of electron-phonon scattering. This scattering probability is unequal for positive and negative $\boldsymbol{k}$ within one subband and

leads to an asymmetric carrier distribution in $\boldsymbol{k}$-space. Each subband yields an electron flux $\boldsymbol{j}_{\pm}$, where + and - stand for spin-up and -down. This effect is called zero bias spin separation [5]. The two electron fluxes are of equal strength but oppositely directed ($\boldsymbol{j}_{+} = -\boldsymbol{j}_{-}$). Thus, the total electric current is zero, but a pure spin current $\boldsymbol{j}_s$ is created given by [5]

$$\boldsymbol{j}_s = \frac{1}{2}(\boldsymbol{j}_- - \boldsymbol{j}_+). \tag{11}$$

By applying an external magnetic field $\boldsymbol{B}$ the two subbands split up energetically due to the Zeeman effect. The difference in energy is given by [35]

$$\Delta E_Z = g\mu_B B, \tag{12}$$

where $g$ is the effective Landé factor of the material and $\mu_B$ is the Bohr magneton. As a result one of the subbands is now preferentially occupied. This results in an imbalance of the two electron fluxes and therefore, they do not cancel each other out anymore (see Fig. 3 (c)). This gives rise to a net electric
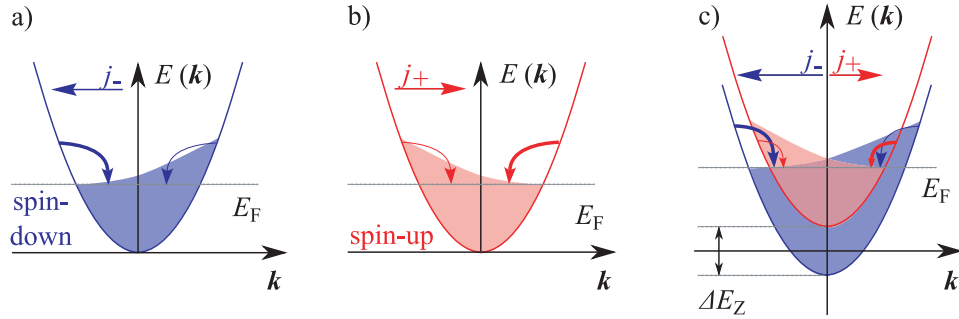
**Figure 3:** Asymmetric relaxation process of a homogeneously heated two dimensional electron gas for (a) spin-down and (b) spin-up subbands. This effect is called the zero bias spin separation. The difference in the arrows' thickness corresponds to the scattering probability of electrons by phonons, which is unequal for positive and negative $\boldsymbol{k}$ within one subband. This yields an asymmetric carrier distribution and consequently an electron flux $\boldsymbol{j}_{\pm}$ in each subband. By applying an external magnetic field the subbands split up energetically due to the Zeeman effect. This results in an imbalance between the electron fluxes $\boldsymbol{j}_+$ and $\boldsymbol{j}_-$ and is depicted in (c).

current $\boldsymbol{j}_Z$ which is proportional to the Zeeman splitting $\Delta E_Z$ and consequently linear in $B$ [29]:

$$\boldsymbol{j}_Z = -e\frac{\Delta E_Z}{E_F}\boldsymbol{j}_s = 4eS\boldsymbol{j}_s. \tag{13}$$

Equation (13) is valid for a degenerated two dimensional electron gas and for a low degree of spin polarization, namely for $\Delta E_Z/2 << E_F$, with Fermi energy $E_F$ [5, 28]. $S$ is the magnitude of the average spin along the direction of $B$ and is given by $S = \frac{n_+ - n_-}{2(n_+ + n_-)}$, with carrier density $n_\pm$ in spin-up and -down subband. For a degenerated two dimensional system the average spin is given by $S = \frac{-\Delta E_Z}{4E_F}$ [5].

Note, that there is a second microscopic mechanism contributing to the MPGE which is related to the spin dependent indirect optical excitation of carriers due to THz absorption in the presence of an external magnetic field. This effect can be explained analogue to the asymmetric relaxation process described above [5, 17].

## 2.3 Photoconductivity Effect

Besides THz radiation induced photocurrents, the radiation also results in a change of conductivity of the semiconductor. For radiation in the THz range and neglecting effects of impurity ionization, this phenomenon is limited to one band as the photon energy is too small for the generation of free carriers across the band gap. Hence, the carrier density $n$ can be assumed to be constant and the photoconductivity $\Delta\sigma$ is solely given by the change of mobility $\Delta\mu$ according to [17, 35]

$$\Delta\sigma = |e|n\Delta\mu, \tag{14}$$

with elementary charge $e$ and with respect to the *dark* conductivity without radiation $\sigma_0 = |e|n\mu_0$. $\mu_0$ is the mobility in the *dark* i.e., without THz radiation. The change of mobility $\Delta\mu$ originates from the change of the carriers' temperature due to electron gas heating by THz absorption. This absorption is drastically enhanced under cyclotron resonance conditions (see Section 2.4),

causing an intensified two dimensional electron gas heating. Therefore, measurements of the photoconductivity represent one of the established methods (next to radiation transmittance, see Section 3.3.4) of determining the effect of cyclotron resonance [14, 36].

## 2.4 Cyclotron Resonance

Free carriers moving in a two dimensional layer with an external magnetic field applied perpendicular to the QW plane experience a deflection due to the Lorentz force $\boldsymbol{F}_L = q[\boldsymbol{v} \times \boldsymbol{B}]$. The carriers are bound to circular orbits in $\boldsymbol{k}$-space normal to the magnetic field with an angular frequency given by

$$\omega_c = \frac{qB}{m^*}. \tag{15}$$

Herein, $m^*$ is the effective electron (hole) mass and $q$ is the charge, which is equal to -$e$ for electrons and +$e$ for holes [37]. High frequency radiation of exactly this angular frequency $\omega_c$ results in a resonant absorption, namely the effect of cyclotron resonance (CR). The power absorbed by the free carriers for circularly polarized radiation is given by [35]

$$P^\pm(\omega) \propto \frac{1}{1 + (\omega \pm \omega_c)^2 \tau^2}, \tag{16}$$

where the signs stand for right- ($\sigma^+$) and left-handed ($\sigma^-$) circular polarization and $\tau$ is the momentum relaxation time. For linearly polarized light, which is a superposition of $\sigma^+$ and $\sigma^-$ polarization, the absorbed power adds up to [35, 37]

$$P^{linear}(\omega) \propto \frac{1}{1 + (\omega + \omega_c)^2 \tau^2} + \frac{1}{1 + (\omega - \omega_c)^2 \tau^2}. \tag{17}$$

A necessary requirement in order to observe CR is $\omega_c \tau \gg 1$. This condition guarantees that the free carriers can perform a whole orbit before being scattered by e.g., impurities. In quantum mechanics, for $k_B T < \hbar \omega_c$, the effect of CR can be considered as a resonant transition between successive Landau levels (see Section 2.5) [35].

When the resonance condition is fulfilled ($\omega = \omega_c$) and $\omega_c \tau \gg 1$ two cases have to be distinguished: electrons and holes differ in their direction of rotation for

a fixed magnetic field polarity. Hence, electrons and holes only absorb one kind of circularly polarized radiation [38].

Considering holes and positive magnetic fields ($q = +e > 0$, $B > 0$, consequently $\omega_c > 0$ according to Eq. (15)) the resonant absorption of light is only given for $\sigma^-$ polarization. The situation for electrons is vice versa. In the case of linearly polarized light, the effect of cyclotron resonance occurs for both carrier types and magnetic field polarities.

## 2.5   Quantum Transport Phenomena

The application of high magnetic fields perpendicular to a two dimensional quantum well plane at low temperatures ($k_B T < \hbar\omega_c$ [39]) leads to a quantization of the energy spectrum into discrete Landau levels. In that case each Landau level corresponds to a discrete $\delta$ peak in the density of states [39]. In a realistic system these levels are broadened due to finite temperatures and scattering. This is sketched in Fig. 4 (b).

The energy of the $l$-th Landau level for a parabolic energy spectrum is given by [6, 40]

$$E_l = \hbar\omega_c(l + \frac{1}{2})  \tag{18}$$

with $l \in \mathbb{N}_0$, yielding a distance between two neighbored Landau levels $l$ and $l \pm 1$ of $\Delta E_{l,l\pm 1} = \hbar\omega_c$. Taking into account Zeeman splitting according to Eq. (12) the number of carriers on each spin split Landau level is given by $n_{LL} = |e|B/h$. For an electron gas with carrier density $n$ the number of filled Zeeman split Landau levels (so-called filling factor $v$) is given by [40]

$$v = \frac{n}{n_{LL}} = \frac{nh}{|e|B},  \tag{19}$$

with Planck constant $h$. If $n$ is fixed the Fermi energy $E_F$ oscillates as a function of the applied magnetic field [40, 41]. These oscillations i.e., the jumps of $E_F$ depend on the density of states $\nu_\pm$ [39]. If there are e.g., $l$ Landau levels completely populated and the $(l + 1)$-st is partly filled, thus the Fermi energy $E_F$ lies within the level $l + 1$. If $B$ increases the Landau level $l + 1$ shifts up
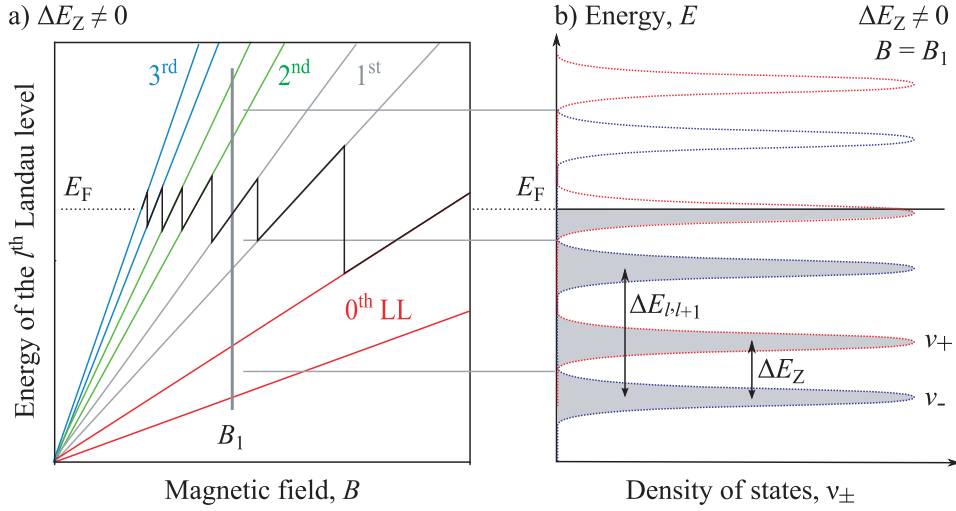
**Figure 4:** Sketch of (a) spin splitted Landau levels and Fermi energy $E_F$ as a function of the magnetic field $B$ for a parabolic dispersion and (b) density of sates $\nu_\pm$ for a fixed $B = B_1$ with Landau level and Zeeman splitting, $\Delta E_{l,l+1}$ and $\Delta E_Z$.

in energy and is emptied. Thus, $E_F$ falls back onto the level below [39]. This is sketched for an ideal system with $\delta$ function Landau levels in Fig. 4 (a). Herein, every jump of the Fermi energy corresponds to a filling factor $\upsilon$: even filling factors correspond to jumps between two Landau levels of different $l$, whereas odd filling factors stand for jumps within a Zeeman split Landau level.

By variation of the magnetic field strength $B$, the Landau levels and corresponding peaks in the density of states are pushed through the Fermi energy. This consecutive crossing of $E_l$ and $E_F$ can also be induced by keeping $B$ fixed and varying $E_F$. Either results in an oscillating behavior of many physical parameters which are periodic in $1/B$. In this work oscillations of the mobility of free carriers and their magnetic momenta are of interest, namely the Shubnikov-de Haas and the de Haas-van Alphen effect.

*Shubnikov-de Haas Effect*   Figure 4 (b) indicates that the density of states at $E_F$ varies with the magnetic field $B$. If $E_F$ lies in between two Landau levels, the density of states at $E_F$ is zero, whereas it has a maximum when $E_F$ is in the middle of a broadened Landau level. This can be directly seen in a

system's longitudinal resistance $R_{xx}(B)$ which is illustrated in Fig. 5 (a) for a 8 nm HgCdTe QW Hall bar structure at 4.2 K. The resistance has a minimum when $E_F$ lies between two Landau levels (zero density of states) and is finite when it lies within a Landau level [39]. This oscillating behavior of $R_{xx}$ as a function of $B$ is the Shubnikov-de Haas (SdH) effect. Furthermore, Fig. 5 (a) demonstrates that for low magnetic fields $R_{xx}(B)$ is constant. This is due to the fact that when $B$ goes to 0, the Landau levels decrease their distance in such a way that they eventually overlap. In this case $E_F$ always lies within this constant density of states and the resistance becomes constant [40].

Each minimum of $R_{xx}(B)$ can be related to a filling factor $\upsilon$ (indicated in the figure) which plotted against $1/B$ yields a straight line with a slope of $hn/e$. This is shown in the inset of Fig. 5 (a). Hence, the Shubnikov-de Haas oscillations are periodic in $1/B$. The analysis of the oscillations can provide information about the carrier density, occupation of higher subbands, which can be seen by two different frequencies in the SdH oscillations, or the evolution of Zeeman spin splitting [39]. The latter can be seen in Fig. 5 (a): for magnetic fields larger than $\approx 2.76$ T (value corresponds to tiny dip between filling factors 10 and 12) even and odd filling factors are observed. This indicates the resolution of the Zeeman splitting of Landau levels.


*De Haas-van Alphen Effect*   Another effect similar to the Shubnikov-de Haas effect originates from a periodic change of the total energy of the free carriers with the magnetic field, namely the de Haas-van Alphen effect. This can be detected experimentally as oscillations of the material's magnetic momentum $\mu_m = -\partial E / \partial B$ [41]. For matters of simplification the spin is neglected in the following. The variation of the total energy of free carriers is depicted in Fig. 5 (b).

For $B = 0$ T the density of states is continuous (regions I and IV). When a magnetic field is applied the carriers squeeze onto discrete Landau levels. For the magnetic field $B_1$ depicted in region II the system has the same energy as for zero magnetic field (region I): the number of carriers which raise their energy is equal to the number of carriers which degrade their energy in order to divide onto the Landau levels. When $B$ is increased to a value of $B_2$, the

total energy of the system increases as the highest carriers shift energetically up (region III). For $B_3$ the system's total energy is back to the initial one (as in I, II or IV) as the uppermost carriers have to decrease in energy (region V) [41]. Consequently, the total energy has a minimum at points such as $B_1$, $B_3$, ... and maximum points at $B_2$, .... This oscillation in energy with a periodicity of $1/B$ can be seen in the free carriers' magnetic momentum and hence, in their spin $S$, as $\mu_m \propto S$.
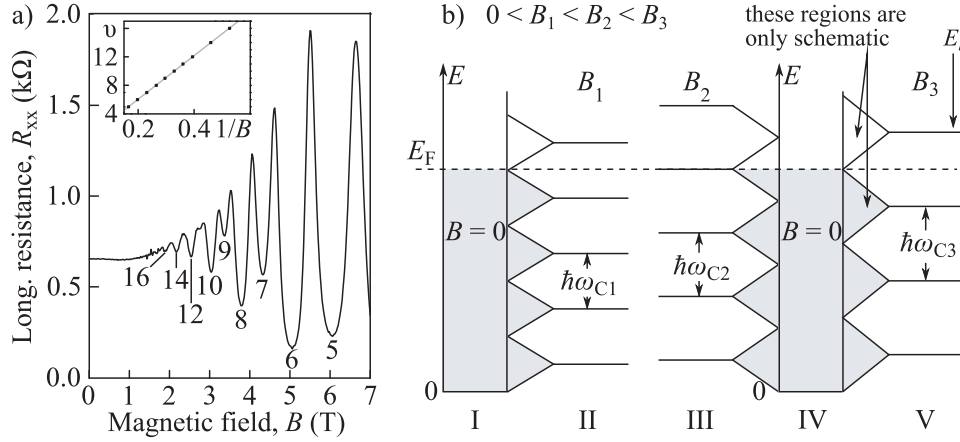


**Figure 5:** (a) Measurement of Shubnikov-de Haas oscillations in the longitudinal resistance $R_{xx}$ of a 8 nm HgCdTe Hall bar sample. Numbers indicate filling factors $\upsilon$. The inset shows the filling factor $\upsilon$ as a function of the inverse magnetic field $1/B$. The de Haas-van Alphen effect is depicted in (b) as a simplified model of the free carriers' total energy; the Zeeman effect is neglected. Whereas the density of states is continuous for $B = 0$ T (regions I and IV), it splits into Landau levels when a magnetic field is applied. In the case of $B_1$ (II) and $B_3$ (V) the total energy is the same as for $B = 0$ T as the same amount of carrier decrease their energy, as increase it. For $B_2$ the total energy is increased as the uppermost carriers shift energetically up (III).

# 3   Experimental Methods

This chapter is devoted to the experimental methods used for the investigations in this work. In order to give a clear picture of the performed measurements the whole experimental setup is depicted first. Then the studied samples are introduced, which can be divided into two groups: diluted magnetic semiconductor (DMS) QW structures and - forming the core of this thesis - HgTe based QW structures. In the third section of this chapter the different measurement techniques are illustrated. These comprise mere electrical and optical, as well as opto-electronic measurement techniques. As the variation of polarization of the THz radiation plays an important role for some of the studied effects e.g., cyclotron resonance, two types of waveplates will be presented.

## 3.1   Experimental Setup

The experimental setup used for the measurements includes a laser system, an optical cryostat with a superconducting split coil magnet, as well as optical chopper systems and other devices. They are all combined in a complex structure, which will be introduced in the following. The whole experimental setup can be seen in Fig. 6.

The laser system consists of an electrically pumped continuous wave (*cw*) *PL5*[1] $CO_2$ gas laser, emitting in the mid-infrared (MIR) range, and a *295FIR*[1] gas laser. This is optically excited by the $CO_2$ gas laser and emits in the far-infrared range (FIR). The THz radiation of the FIR laser is line tunable and its wavelength depends on the kind of gas filled into the cavity, as well as on the exact wavelength of the exciting MIR radiation. For this thesis a wavelength of 118.8 $\mu$m was used. The parameters of the operating laser system are given in Tab. 1.

The $CO_2$ gas laser belongs to the group of vibrational and rotational gas lasers and is one of the most important representatives of the group of molecular lasers. It is longitudinal electrically excited and delivers a power of approximately 35 W. The emitted wavelength can be tuned around and between the

---

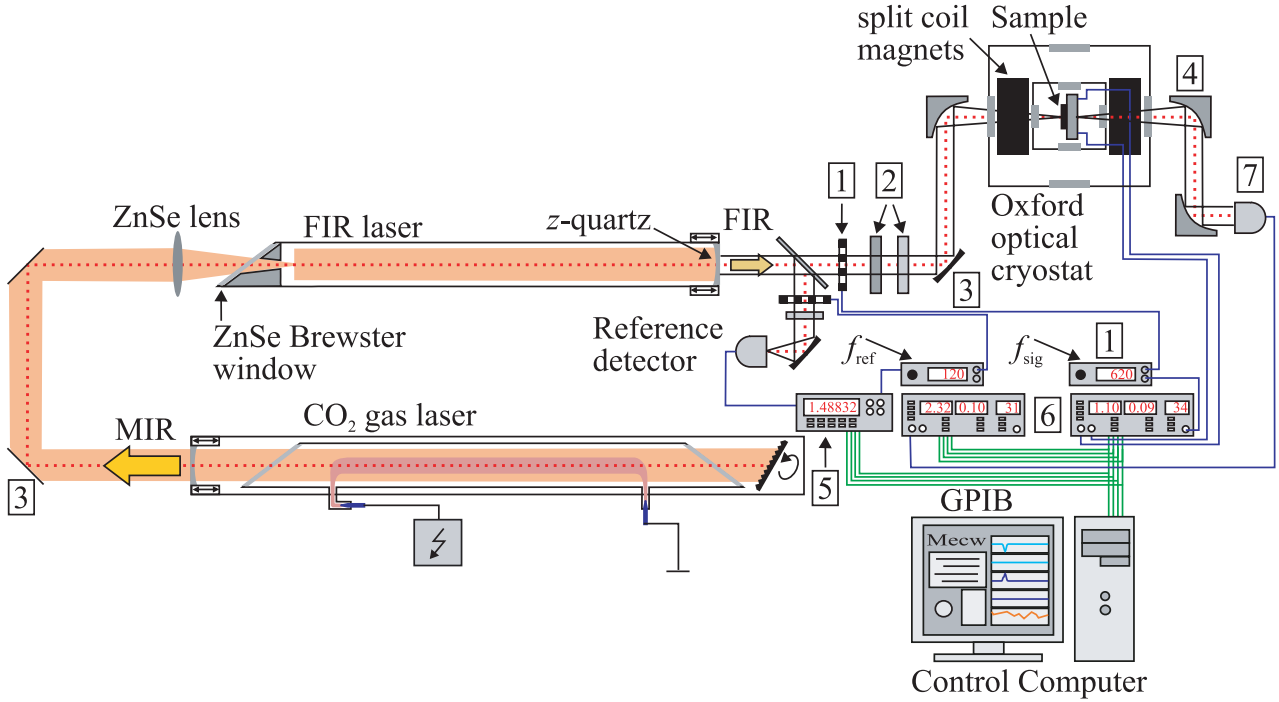[1]Edinburgh Instruments, Livingston, UK

**Figure 6:** Experimental setup with MIR ($CO_2$) and FIR gas laser system. The optical path is sketched as a red line. Most devices are labeled in the picture. 1: optical chopper, 2: waveplates or other optical devices, 3: planar mirror, 4: parabolic mirror, 5: digital multimeter, 6: lock-in amplifier, 7: Golay cell. A detailed description is given in the text. Picture modified after Ref. [42].

lines of 9.4 and 10.4 $\mu$m. These lines belong to two different optical active transitions between vibrational modes of the $CO_2$ molecule. The line tuning is possible as these vibrational modes split up into different rotational modes [17, 43]. The output radiation is not used for experiments, but acts only as an optical pump source for the second molecular gas laser. Hence, the radiation is deflected by two planar mirrors and focused by a zinc selenide (ZnSe) lens through a polarizing ZnSe Brewster window mounted on top of a steel cone into the cavity of the FIR laser system. The Brewster window ensures linearly polarized light, with the $\boldsymbol{E}$-field vector being aligned horizontally. The incoming MIR radiation excites a vibrational state of the molecule of the second gas laser system having a permanent electric dipole moment.

| $\lambda$ MIR laser ($\mu$m) | FIR laser gas | $\lambda$ ($\mu$m) | $f$ (THz) | $E_{\hbar\omega}$ (meV) | $P$ (mW) |
|---|---|---|---|---|---|
| 9.695 | methanol | 118.8 | 2.53 | 10.35 | 60 |

**Table 1:** Parameters of the operating laser system: excitation wavelength $\lambda$ of the $CO_2$ gas laser; laser gas of the FIR laser system; wavelength $\lambda$, frequency $f$, photon energy $E_{\hbar\omega}$ and power $P$ of the emitted THz radiation.

This is sketched in Fig. 7 (a) for a symmetrical top molecule, where $K$ is the projection of the angular momentum $J$ on the symmetry axis of the molecule. Assuming that the vibrational relaxation is slow enough, lasing transitions occur between rotational states only emitting radiation in the FIR range [17]. The cavity of the FIR laser is closed by a silver coated $z$-quartz window, which is transparent for wavelengths with frequencies in the THz range, but reflects the MIR radiation and so ensures a monochromatic output. The transversal mode shape can be adjusted by variation of the resonator length via screws at the silver coated quartz window. It can be monitored by thermal paper or by a *Pyrocam III*[2] in order to verify that the beam has a Gaussian shape (see Fig. 7 (b)). The emitted monochromatic FIR radiation of the molecular gas laser is directed through a beam splitter, consisting of Mylar[3]. The reflected part of the beam ($\approx 15\%$) is used as a reference signal in the analysis of the measurements and allows to monitor the stability of the laser. It is modulated by a *300CD*[4] optical chopper with a frequency of $f_{ref} = 140$ Hz and directed to a pyroelectric reference detector *LIE-329-Y*[5] by a planar mirror. This reference signal $U_{ref}$ is measured by a *KI2000*[6] digital multimeter and sent to a control computer running a LabVIEW[7] program. This LabVIEW program controls the whole experimental setup and records all measured data. It was written by Wolfgang Weber[8] and Sergey Danilov[8]. The main part of the beam ($\approx 85\%$) is transmitted through the beam splitter and is modulated by a second *300CD*[4] optical chopper at a frequency of $f_{sig} = 620$ Hz. At this

---

[2]pyrometer for temperature detection, Spiricon Inc., Logan, UT, USA
[3]a polyester film made from stretched polyethylene terephthalate
[4]Scitec Instruments, Wiltshire, UK
[5]Laser Components, Olching, Germany
[6]Keithley Instruments, Germering, Germany
[7]Laboratory Virtual Instrumentation Engineering Workbench
[8]Terahertz Center, Regensburg, Germany

point additional devices e.g., waveplates or analyzers can be inserted into the optical path. The integration of a step motor, which is operated by LabVIEW and rotates the mounted waveplates step wise, is possible. The beam is then deflected by a planar mirror and is focused by a parabolic[9] one into a *Spectromag SM4000-8*[10] optical cryostat. The inner windows of this cryostat are made of $z$-cut quartz, the outer windows are fabricated of TPX[11]. As these are transparent for THz and visible light, the latter are covered with a black polyethylene sheet to prevent illumination of the sample with ambient light. The sample is located in the middle of the cryostat between two superconducting split coil magnets, allowing magnetic fields up to 7 T perpendicular to the sample's surface. The magnetic field can by controlled by an *IPS120-10*[10]

---

[9]focal length $f = 22.5$ cm, Kugler GmbH, Salem, Germany
[10]Oxford Instruments, Abingdon, UK
[11]polymethylpenten
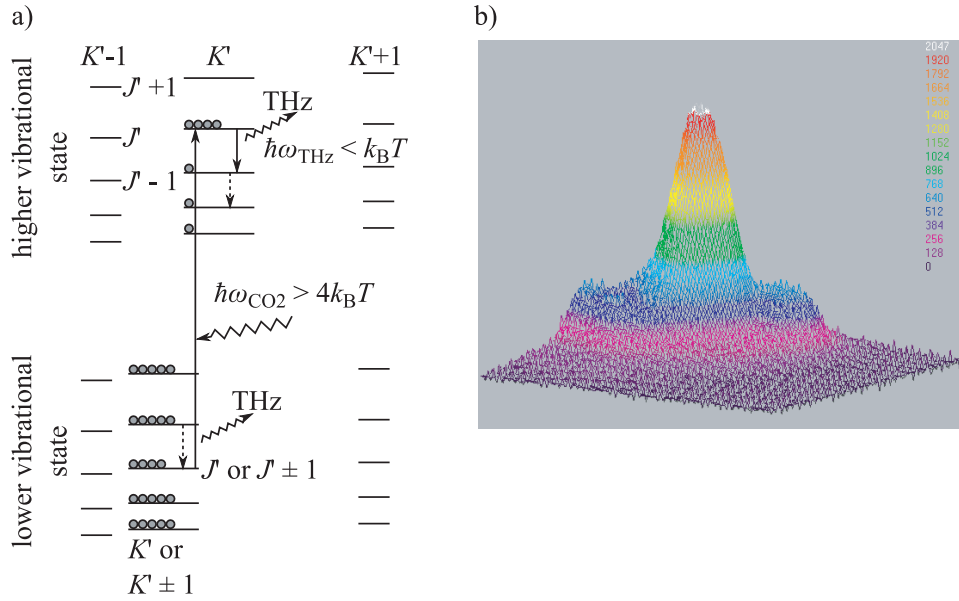


**Figure 7:** (a) Scheme of optically pumped THz transitions in a symmetric top molecule. Electrons are excited to a higher vibrational mode by the incoming $CO_2$ gas laser radiation, yielding a population inversion in both states. Relaxation transitions occur between the rotational modes of both vibrational states, emitting radiation in the THz range. (b) Spatial beam shape with an average power of $\approx 60$ mW, recorded with the *Pyrocam III*[2].

power supply. The temperature at sample position can be varied from liquid helium temperature ($T = 4.2$ K) up to room temperature, is maintained and measured by a *LS332*[12] temperature controller. A wiring system connects the sample with two *SR830 DSP*[13] lock-in amplifiers, with an input resistance of 10 MΩ, allowing the measurement of two different voltage drops across the sample (compare Section 3.2 and 3.3). A part of the radiation is transmitted through the sample and leaves the cryostat on the other side. It is then parallelized and focused, both by a parabolic mirror[14], to a Golay cell detector[15], whose output can be recorded via lock-in technique. The lock-ins are connected to the control computer via GPIB[16] as well as the reference detector by a digital multimeter, temperature and magnetic field controller and step motor unit. As mentioned before, all variables are recorded and can be set by the LabVIEW program.

## 3.2 Investigated Samples

In the framework of this thesis two different groups of semiconductor structures were investigated: HgTe based quantum well heterostructures of similar layer design, but different QW widths $L_W$ and two diluted magnetic semiconductor QW structures. Their designs and properties will be introduced in the following.

### 3.2.1 Mercury Telluride Quantum Well Samples

The main part of this thesis is devoted to photocurrents in HgTe based QW structures. The samples were provided by Nikolai N. Mikhailov[17] and Sergey A. Dvoretsky[17]. They were grown by molecular beam epitaxy (MBE) onto a (013) oriented gallium arsenide (GaAs) substrate [44]. These (013) grown QWs belong to the $C_1$ point group possessing no symmetry restriction. The HgTe

---

[12]Lake Shore Cryotronics, Westerville, OH, USA
[13]Stanford Research Systems, Sunnyvale, CA, USA
[14]focal length $f = 22.5$ cm, Kugler GmbH, Salem, Germany
[15]Artas GmbH, Zeitlarn, Germany
[16]General Purpose Interface Bus
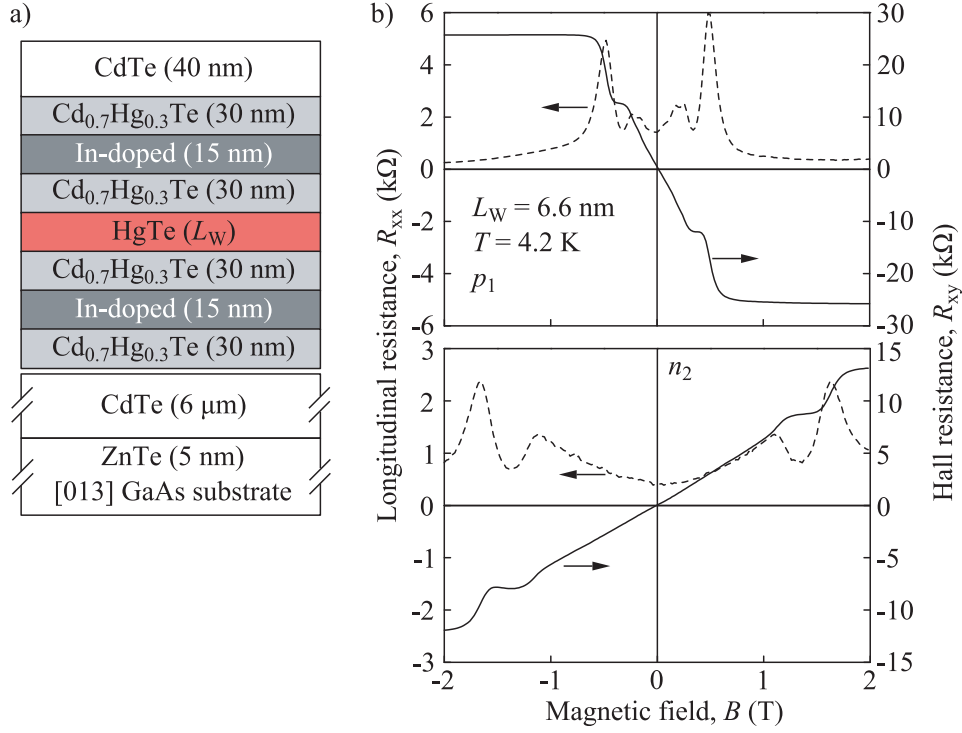[17]Institute of Semiconductor Physics, Novosibirsk, Russia

**Figure 8:** (a) shows a cross section of the layer design of the investigated HgTe based QW samples. The QW layer with width $L_W$ is indicated in red. (b) depicts a typical result of a magneto-transport measurement by which all samples were characterized. The results of a 6.6 nm wide HgTe QW are presented for two different carrier types and densities $p_1$ and $n_2$ (see Chapter 5). The upper panel corresponds to a $p$-type sample, while the lower one shows a $n$-type behavior. Solid lines show the Hall resistance $R_{xy}$ with Hall plateaus, dashed lines are the longitudinal resistance $R_{xx}$ with Shubnikov-de Haas oscillations. They scale on the right and left, respectively.

QW is sandwiched between two layers of $Cd_{0.7}Hg_{0.3}Te$. Figure 8 (a) shows an exemplary cross section. Depending on the QW width $L_W$ the band structure can change its ordering, as described in Section 2.1. This makes it possible to divide the samples into three groups of band structure: normal and inverted parabolic as well as linear.

The samples were prepared in different designs e.g., large area square shaped samples and Hall bars (see Fig. 9). These various designs are due to the different kind of measurements performed on the samples. While Hall bar structures

| width $L_W$ (nm) | design | gating | band structure |
|:---:|:---:|:---:|:---:|
| 5 | square | no | normal |
| 6.4 | Hall bar | no | linear |
| 6.6 | Hall bar | yes & no | linear |
| 6.6 | square | no | linear |
| 8 | Hall bar* | no | normal |
| 8 | square | no | inverted |
| 21 | square | no | inverted |

**Table 2:** QW width $L_W$, design, gating and band structure of the investigated HgTe QW samples. *The QW contains cadmium: $Hg_{0.86}Cd_{0.14}Te$.

show best resolved Shubnikov-De Haas oscillations and quantum Hall plateaus, they are not ideal for photocurrent or transmission measurements. For this purpose the samples have to be large enough to ensure no illumination of the contacts or samples' edges. Both can both give rise to other signals superimposing the investigated effects. Therefore, radiation transmittance, as well as photocurrent experiments are mainly studied on large area $5\times5$ mm$^2$ square samples, where the indium (In) contacting was done at the samples' edges and corners only (see next section).

An overview of the studied HgTe QW samples, their design and band structure is given in Tab. 2. All the samples have been characterized by magneto-transport measurements, as described in Section 3.3.1. Carrier densities are given in Chapters 5-6, where the experimental results are presented.

*Normal Parabolic Band Structure*   Two samples with normal band structure were investigated. The first one is a pure HgTe QW with a width $L_W = 5$ nm, which is smaller than the critical width $L_C$. Hence, it is characterized by a normal parabolic band ordering where the $E_1$ band lies above the $H_1$ band as known from conventional semiconductors (e.g., GaAs, CdTe or InAs). The sample's design is a large area square with an edge length of 5 mm. Eight ohmic In contacts are soldered to the corners and to the middle of the edges (compare Fig. 9 (a) and (b)). These ohmic contacts are connected to the pins

of an eight-pin chip carrier via gold wires, which allow the measurement of the voltage drops induced by bias or THz radiation.

The second sample is a 8 nm HgCdTe QW Hall bar structure. It has a 14% Cd content in the QW, in contrast to all other pure HgTe QWs. As a consequence, the transition from normal to inverted parabolic band structure is obtained for wider QWs than for pure HgTe QWs [26, 45]. In case of the here investigated $Hg_{0.86}Cd_{0.14}Te$ sample with a width of $L_W = 8$ nm the dispersion is normal parabolic. The Hall bar structure is depicted in Fig. 9 (c) and (d). It is 50 $\mu$m wide, with distances between the contacts of 100 and 250 $\mu$m. The contact pads of the Hall bar are soldered in the same way as the contacts of the square sample i.e., via In contacts and gold wires. The sample is mounted on an eight-pin chip carrier.

*Linear Band Structure*  Increasing the QW width $L_W$ the $E_1$ and $H_1$ bands touch each other at a critical width $L_C$ of approximately 6-7 nm (see Fig. 2 (a)) [11,13,46]. At this point the dispersion shows a linear, Dirac-like behavior. For this thesis a quantum well width of 6.6 nm was selected. Samples in both shapes, Hall bar and square, were investigated. Two Hall bar structures were available, prepared with and without gate. A gate enables a controllable way of carrier density variation. Therefore, an isolating layer of 100 nm silicon dioxide ($SiO_2$) and 200 $\mu$m silicon nitride ($Si_3N_4$) is used with a metallic gate layer of titanium gold (TiAu) deposited on top. The gate layer can be biased via a pin of the eight-pin chip carrier to which it is connected by a gold wire.

*Inverted Parabolic Band Structure*  As a last group samples with a QW width $L_W$ larger than the critical width $L_C$ were under study. For this case the electron band $E_1$ and heavy hole band $H_1$ are exchanged in contrast to conventional semiconductors e.g., CdTe. Hence, they are characterized by an inverted band ordering. Two samples were available, with widths of 8 and 21 nm. The samples' design is a 5×5 mm$^2$ square shape. The contacting is done in the same way as described above.
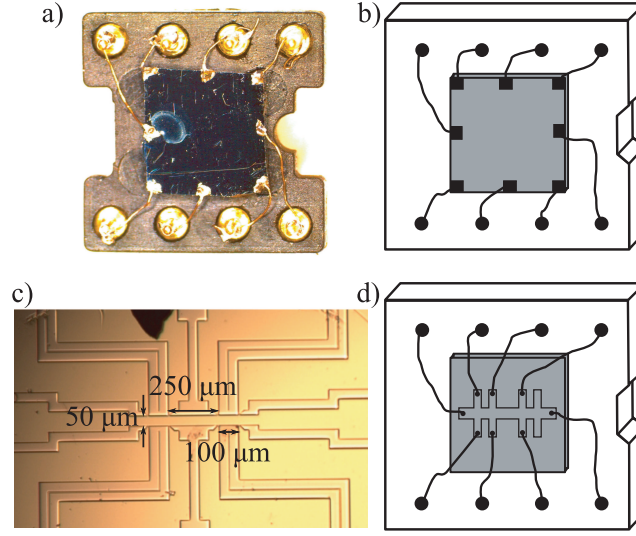
**Figure 9:** (a) shows a picture of a square shaped sample mounted on a chip carrier. It is connected to the pins via gold wires and In soldering. (b) gives a schematic drawing of (a). (c) depicts a Hall bar structure with a width of 50 $\mu$m and distances between contacts of 100 and 250 $\mu$m. (d) shows the wiring of the Hall bar sample on a chip carrier.

### 3.2.2 Diluted Magnetic Semiconductor Samples

In DMS structures paramagnetic ions e.g., manganese ($Mn^{2+}$), are introduced into the host material. These $Mn^{2+}$ ions provide magnetic moments, which give the opportunity of a controllable variation of the magnetic properties of the semiconductor. This can be done by e.g., using different host materials, changing the $Mn^{2+}$ concentration or varying the temperature. In the following, two DMS samples are investigated with different host materials: a CdTe based and an indium arsenide (InAs) based QW structure. Both samples are (001) MBE grown QW structures on a GaAs substrate. They are fabricated as large area squares of the same dimensions and contact preparation as the HgTe samples (see Section 3.2.1). Their properties are summarized in Tab. 3 of Section 4.1. (001) grown CdTe and InAs QW structures belong to the $C_{2v}$ symmetry group. Both have two mirror planes perpendicular to the QW and a $C_2$ axis parallel to the growth direction. Depending on the host material (CdTe, II-VI or InAs, III-V) the $Mn^{2+}$ ions result in different electrical properties.

Among the DMS materials Cd(Mn)Te is one of the most intensely studied semi-conductor heterostructures. The sample was provided by the group of Tomasz Wojtowicz[18]. The 10 nm wide Cd(Mn)Te QW is embedded between two layers of $Cd_{0.7}Mg_{0.3}Te$ (see Fig. 10 (a)). During the growth process three monolay-ers of $Cd_{0.86}Mn_{0.14}Te$ were inserted applying digital alloy technique [47–49]. CdTe belongs to the group of II-VI semiconductors. In this case the $Mn^{2+}$ is electrically neutral as it substitutes $Cd^{2+}$, which has the same valence. But it provides a localized spin of 5/2 [18]. The sample is iodine (I) doped and characterized by a $n$-conductivity.

The second DMS sample has an InAs host material. InAs is, in contrast to CdTe, a narrow band gap material just like HgTe. The structure is MBE grown by Dieter Schuh[19] and Ursula Wurstbauer[19] and has a 4 nm wide In(Mn)As QW embedded in a 20 nm $In_{0.75}Ga_{0.25}As$ channel. Fig. 10 (b) depicts a cross section of the structure with a $Mn^{2+}$ doping layer grown before the QW. Due to segregation processes the QW features a limited $Mn^{2+}$ concentration [50–52]. InAs belongs to the III-V semiconductor group. Therefore, the $Mn^{2+}$

---

[18]Institute of Physics, Warsaw, Poland
[19]Terahertz Center, Regensburg, Germany
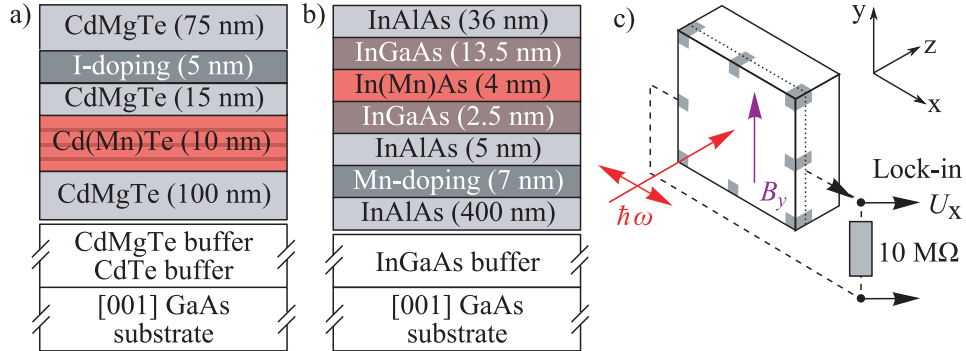


**Figure 10:** (a) depicts a schematic cross section of the Cd(Mn)Te sample. Herein, three monolayers of $Cd_{0.86}Mn_{0.14}Te$ were inserted during the growth of the 10 nm wide QW. (b) shows the In(Mn)As structure which has a $Mn^{2+}$ doping layer inserted before the QW. Due to segregation of the manganese during the growth process, the 4 nm wide QW has a limited concentration of $Mn^{2+}$. In (c) the experimental geometry is sketched, with inplane magnetic field and normal incidence of radiation.

ions provide free holes in addition to the localized magnetic moments as they substitute In$^{3+}$. This results in a $p$-type conductivity of the In(Mn)As DMS sample [50, 53].

## 3.3  Electrical and Optical Measurement Techniques

At this point the different measurement techniques, which were used in this work, will be introduced. These comprise magneto-transport measurements, analysis of THz radiation induced photocurrents and photoconductivity (photoresistance), as well as the detection of the transmitted radiation through the sample.

### 3.3.1  Characterization via Magneto-Transport Measurements

Standard magneto-transport measurements were performed for every sample in order to determine carrier type and density. For this kind of measurement the sample was $ac$ biased with 1 V. The current was limited by a 1 MΩ resistor giving an $ac$ current of 1 $\mu$A through the sample. An external magnetic field was applied normal to the QW plane. The signals $U_x$ and $U_y$ were measured with lock-in technique via a voltage drop over a 10 MΩ load resistor (compare Fig. 11 (a)). These signals correspond to the Hall and longitudinal resistance, respectively, using $R = U/I_{ac}$. In most cases a Van-der-Pauw geometry was used. An exemplary result of such a measurement, which was performed on a 6.6 nm HgTe QW sample (see Chap. 5), is depicted in Fig. 8 (b) for two different carrier types and densities. Well pronounced Shubnikov-de Haas oscillations and quantum Hall plateaus can be seen in the longitudinal ($R_{xx}$) and Hall ($R_{xy}$) resistance. The different slopes of the Hall resistance indicate the different carrier types: holes in the upper panel and electrons in the lower one. To achieve a controllable variation of the carrier density some samples were prepared with a gate (compare Section 3.2) or the effect of persistent photoconductivity was used [14, 54]: by illuminating the sample with a red light emitting diode ($\lambda = 630$ nm) for a defined time $t_i$ the carrier density can be changed. This process can be undone by heating the samples up to $\approx 150$ K. In the following this procedure is referred to as *optical doping* [54, 55].
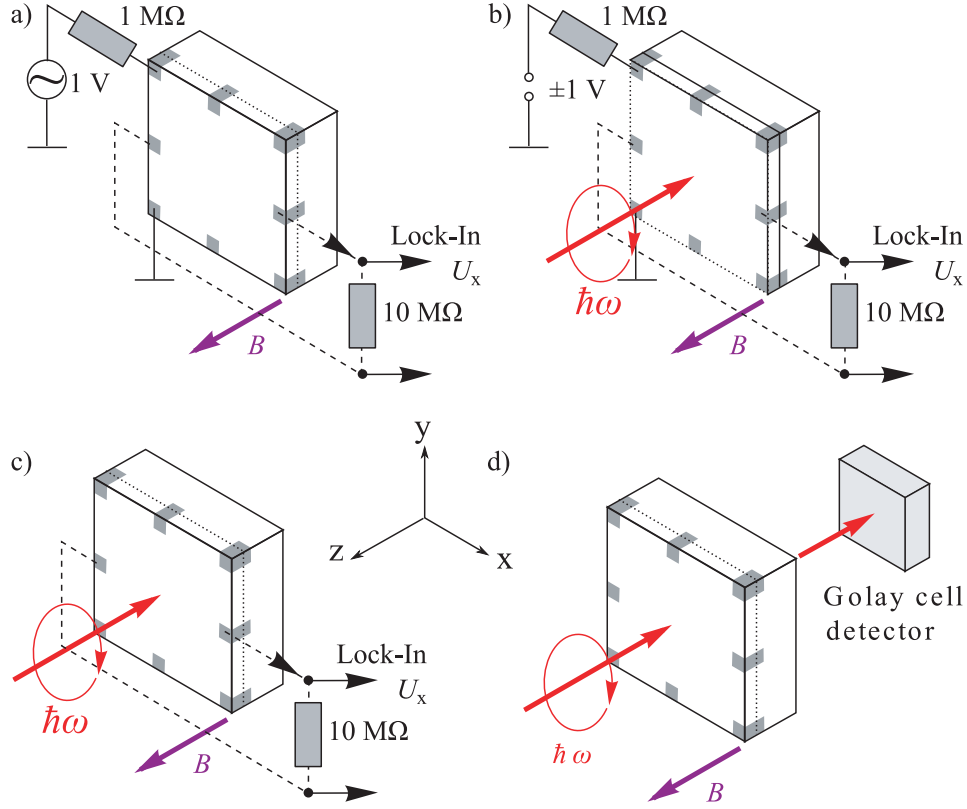
**Figure 11:** Overview of the different measurement setups with a magnetic field $B$ applied normal to the sample's surface for (a) magneto-transport, (b) photoconductivity (photoresistance), (c) photocurrent and (d) radiation transmission. In (a) an *ac* current is sent through the sample and two voltage drops $U_x$ and $U_y$ (the latter is not shown) are measured. These signals are proportional to the Hall and longitudinal resistance. The setup for (b) is similar but with a *dc* current and THz radiation of normal incidence. For (c) the sample is unbiased but also with THz radiation. For (a)-(c) the signals $U_i$, with $i = x, y$, are measured as a voltage drop over a 10 MΩ load resistor via lock-in technique. Note, that the $y$ direction can be measured analog to the $x$ direction which is indicated in the figure. (d) presents a pure optical measurement, where the transmitted radiation through the sample is detected by a Golay cell detector.

### 3.3.2 THz Radiation Induced Photocurrents

For the measurement of photocurrents the unbiased sample was illuminated under normal incidence with THz radiation. An external magnetic field was applied perpendicular to the sample's surface. This radiation induces photocurrents, which were measured analog to Section 3.3.1, via a voltage drop over a 10 MΩ load resistor applying lock-in technique. The corresponding setup is depicted in Fig. 11 (c). In order to eliminate fluctuations of the laser power during a measurement the signals $U_x$ and $U_y$ were normalized by the recorded reference signal $U_{ref}$. Then they were multiplied with the power calibration factor $P_{calib}$ given in units of (V/W) according to $(U_i \times P_{calib})/U_{ref}$ in (V/W) with $i = x, y$. The calibration factor was obtained with a *Vector H410*[20] powermeter by measuring the averaged laser output power $P$ and normalizing it to a mean value of reference signal $U_{ref}$.

Note, that for the DMS samples, with $C_{2v}$ symmetry, photocurrents are forbidden for normal incidence of light and a perpendicular magnetic field [24]. Therefore, the study of THz radiation induced photocurrents was done with an inplane magnetic field. This is shown in Fig. 10 (c).

### 3.3.3 Measurement of Photoresistance

As a complementary measurement studies of the photoresistance (or photoconductivity) $\Delta R$ were performed. $\Delta R$ corresponds to the change of the sample's resistance when illuminating the structure with THz radiation. In order to distinguish between the two THz radiation induced effects of photocurrent and photoresistance, the sample was biased individually either with a positive or a negative *dc* electric current of $|I_{dc}| = 1$ μA ($\pm 1$ V, 1 MΩ). The magnetic field $B$ and the propagation direction of the THz radiation were aligned normal to the sample's surface. The voltage drops $U_{i,\pm}$, with $i = x, y$, for both currents $\pm I_{dc}$ were recorded as sketched in Fig. 11 (b). While the effect of photoresistance (photoconductivity, $U_{i,\pm}^{PC}$) is dependent on the current direction through

---

the sample, the photogalvanic effect ($U_{i,\pm}^{PGE}$) is not effected. Consequently, the difference of these two signals divided by the current, given by

$$\Delta R_i = \frac{U_{i,+} - U_{i,-}}{2I_{dc}} = \frac{(U_{i,+}^{PC} + U_{i,+}^{PGE}) - (-U_{i,-}^{PC} + U_{i,-}^{PGE})}{2I_{dc}}, \qquad (20)$$

corresponds to the change of resistance. It is inverse proportional to the change of conductivity and to the difference in mobility $\mu$ (see Section 2.3). These measurements are performed in addition to opto-electronic photocurrent measurements - the main topic of this work - and provide access to additional information e.g., on cyclotron resonance [36].

### 3.3.4 Measurement of Radiation Transmittance

For a further understanding measurements of radiation transmission were performed, which is a standard method for the identification of the effect of cyclotron resonance. The corresponding setup is shown in Fig. 11 (d) with the magnetic field and the propagation direction of the THz radiation aligned normal to the QW plane. Radiation transmittance is a sheer optical measurement technique; the sample was therefor without bias and no wiring was needed. A Golay cell[21] behind the sample detected the transmitted part of light and gave the signal to a lock-in amplifier. As the Golay cell is a very slow detector the modulation frequency $f_{sig}$ of the radiation was reduced to $f_{tm} \approx 30$ Hz. Due to high thermal noise on the one hand and a slight hysteresis effect of the detector on the magnetic field on the other hand, every transmission measurement was recorded twice (for both magnetic field sweeping directions) and averaged afterwards.

---

[21]Artas GmbH, Zeitlarn, Germany

## 3.4   Development and Characterization of THz Waveplates

As the variation of the polarization state of radiation is important for many aspects of this work, in particular for the cyclotron resonance assisted measurements, it was necessary to use waveplates suitable for the THz range and of best possible quality.

In cooperation with *Tydex*[22] a special waveplate was developed applicable for a wide spectral region in the THz range, which is called achromatic waveplate. The analysis of the conversion of linearly to circularly polarized light was done by rotating an analyzer mounted in a stepmotor unit behind the waveplate and measuring the transmitted radiation intensity with a *LIE-329-Y*[23] pyroelectric detector. Setup and results can be seen in Fig. 12 (a) and (c) for a wavelength of $\lambda = 118.8$ $\mu$m. The transmitted radiation intensity is almost independent of the angle $\beta$ of the analyzer. This means that the *Tydex* achromatic waveplate demonstrates a high quality of polarization conversion to circularly polarized light. Similar results were obtained for other wavelengths with frequencies in the THz range. Details can be seen in Ref. [56].

In addition a waveplate made for a wavelength of $\lambda = 118.8$ $\mu$m from *QMC Instruments*[24] was verified. It features a special anti-reflection coating which increases the transmittance behavior of the $z$-cut quartz plates. As the plates had no indication of the optical axis it had to be determined experimentally. For this purpose the linearly polarized radiation passes through the waveplate and then through an analyzer, aligned parallel or perpendicular to the initial linear polarization. The transmitted radiation is then detected with a *LIE-329-Y*[22] pyroelectric detector as a function of the angle $\varphi'$. The angle $\varphi'$ of the waveplate is varied in 2° steps from 0 to 360° perpendicular to the propagating direction of the radiation. This setup can be seen in Fig. 12 (b). The signal of the transmitted radiation is measured for both grid alignments. This is shown in Fig. 12 (d). The two touching points at $\varphi' \approx 67$ and 157° correspond to circularly polarized radiation. For this case the horizontal and vertical linearly

---

[22]St.Petersburg, Russia

[23]Laser Components, Olching, Germany

[24]West Sussex, UK

polarized part of light have the same intensity. In order to analyze the quality of the waveplate the same measurement as for the achromatic waveplate was done (see Fig. 12 (a)). The result is shown in Fig. 12 (e). With a deviation from the mean signal of only 7% the waveplate demonstrates an excellent quality.

Many measurements of this thesis were carried out with right- or left-handed circularly polarized radiation. In these cases the waveplate from *QMC Instruments* was used.
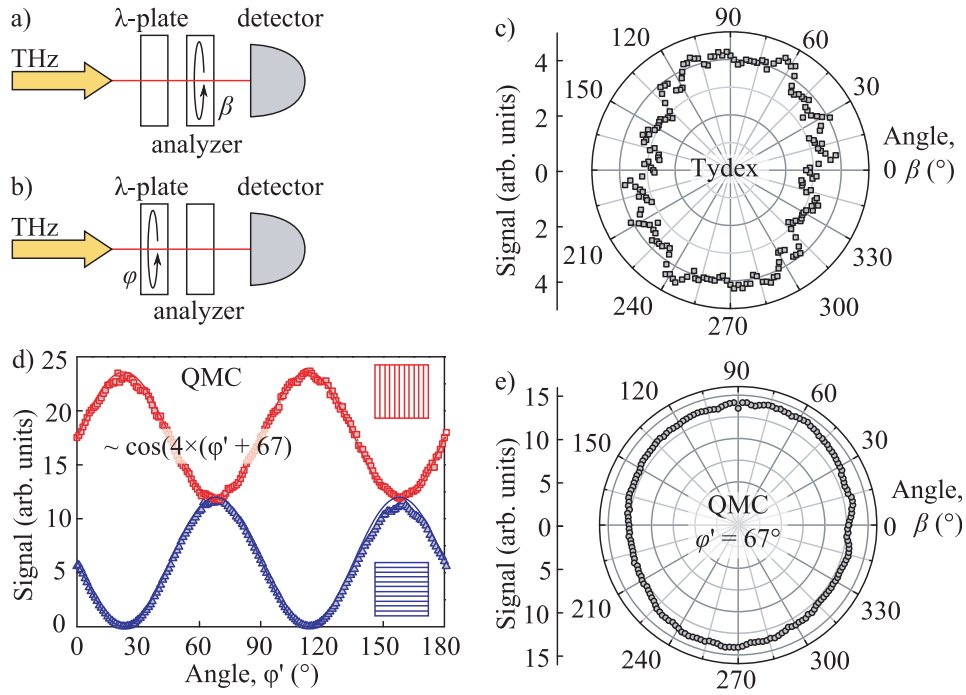


**Figure 12:** (a) and (b) show the setup for the analysis of the waveplates' quality and estimation of the optical axis. (c) depicts the transmitted laser intensity in dependency of the analyzer rotation angle $\beta$ for the achromatic waveplate from *Tydex* for a wavelength of $\lambda = 118.8 \ \mu$m. In (d) the transmitted radiation is detected depending on the rotation angle $\varphi'$ of the *QMC Instruments* waveplate for two different grid positions of the analyzer and $\lambda = 118.8 \ \mu$m. (e) shows the same as (c) but for the *QMC Instruments* waveplate. The alignment of the waveplate is chosen as $\varphi' = 67°$ which corresponds to the first touching point in (d), where the transmitted part of radiation is fully circularly polarized.

# 4 Magnetogyrotropic Photogalvanic Effect in a Diluted Magnetic Semiconductor Hetero-structure

The magnetogyrotropic photogalvanic effect is a rather novel opto-electronic method for the investigation of semiconductor heterostructures. In order to understand its spin dependent origin a well established semiconductor system will be analyzed before turning to the core of this thesis - the study of THz radiation induced photocurrents in HgTe based QW systems. A suitable candidate for this are diluted magnetic semiconductor heterostructures as they are well characterized and provide an opportunity to control the sample's magnetic properties. In this chapter the experimental observations for a Cd(Mn)Te and In(Mn)As DMS sample will be presented and discussed by means of the MPGE (compare Section 2.2). The results are published in Ref. [19]. Only a part of the experimental results of Ref. [19] are presented here.

## 4.1 Experimental Results

The THz radiation induced photocurrents in the unbiased DMS samples were measured as a function of a magnetic field $B_y$ applied in the QW plane for different fixed temperatures. In addition, measurements of the temperature dependency of the photocurrents for a given magnetic field value were performed. As the measured directions $x$ and $y$ show a similar behavior, only the photocurrent $j_x$ normalized by the laser power $P$ will be discussed here. Furthermore, the observed currents have been shown to be an odd function of the magnetic field. Therefore, the presented curves are limited to positive $B_y$ only. For excitation linearly polarized light was applied normal to the QW plane with a wavelength of 118.8 $\mu$m.

Figure 13 (a) shows the THz radiation induced currents $j_x/P$ measured in the Cd(Mn)Te sample for temperatures of 1.8, 4.2, 8 and 40 K as a function of the inplane magnetic field. Note, that some curves are multiplied by a factor for a better comparison, indicated near the corresponding curve. For high temperatures or for low temperatures and small magnetic fields, the magnitude of the

photocurrent shows a linear behavior (solid lines in Fig. 13 (a)). Whereas, for low $T$ and high $B_y$ the current saturates with increasing magnetic field and for $T = 1.8$ K even shows a decrease for magnetic fields larger than $\approx 3$ T. The maximum current of -0.74 $\mu$A/W is observed for $T = 1.8$ K and $B_y = 3$ T. In general the amplitude of $j_x/P$ decreases drastically with increasing $T$. In order to study this temperature dependency further, additional measurements were performed at a constant inplane magnetic field of 2 T. The photocurrents were measured while cooling down the sample slowly from 150 to 1.8 K. This is depicted in Fig. 14 (a). The amplitude increases strongly by more than two orders of magnitude in the investigated temperature range. The current has a positive maximum of +7.4 nA/W at approximately 21.4 K, changes sign at about 13 K (inset in Fig. 14 (a)) and exhibits an absolute maximum value of -0.69 $\mu$A/W at 1.8 K.



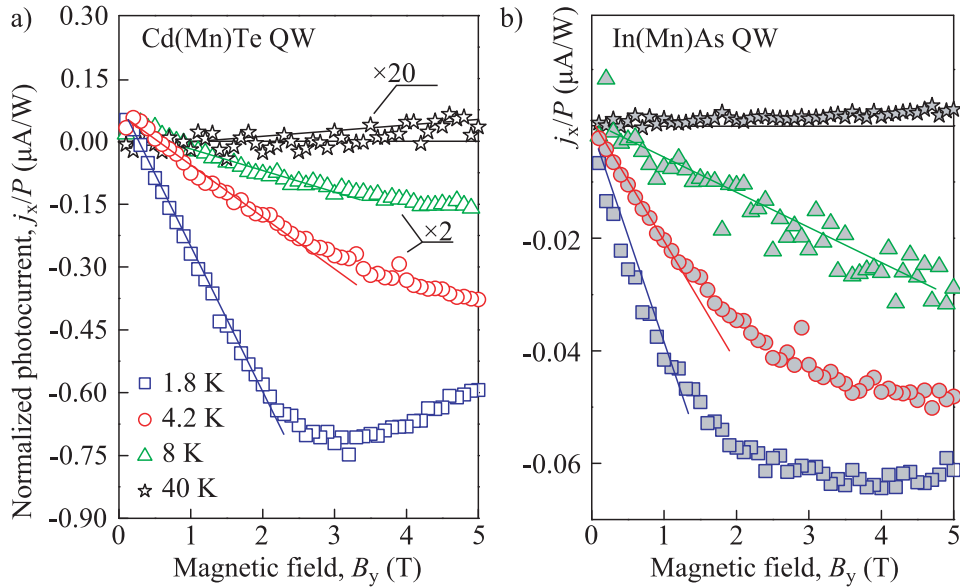**Figure 13:** Magnetic field dependency of the normalized photocurrent $j_x/P$ for the (a) Cd(Mn)Te and (b) In(Mn)As QW sample at different temperatures. The THz radiation was linearly polarized with a wavelength of 118.8 $\mu$m. Note, that some curves in (a) are multiplied by a constant factor for a better comparison. The factors are indicated in the figure. Solid lines are guides for the eye.

For the In(Mn)As sample the photocurrents as a function of the magnetic field at constant temperatures (Fig. 13 (b)) and of the temperature at a fixed magnetic field (Fig. 14 (b)) show similar behaviors as for the Cd(Mn)Te structure. The linear dependency on $B_y$ for small magnetic fields is observed for the whole temperature range and is indicated by solid lines in Fig. 13 (b). For $T = 1.8$ K the current saturates at a value of approximately -64.0 nA/W for fields larger than $\approx 3$ T. Furthermore, the amplitude of the current drastically increases when the sample is cooled down from 150 to 1.8 K. It has a maximum amplitude of -55.2 nA/W at approximately 2 K and 2 T. In contrast to the Cd(Mn)Te sample, however, there is no obvious change of sign in the whole temperature range (see inset in Fig. 14 (b)).
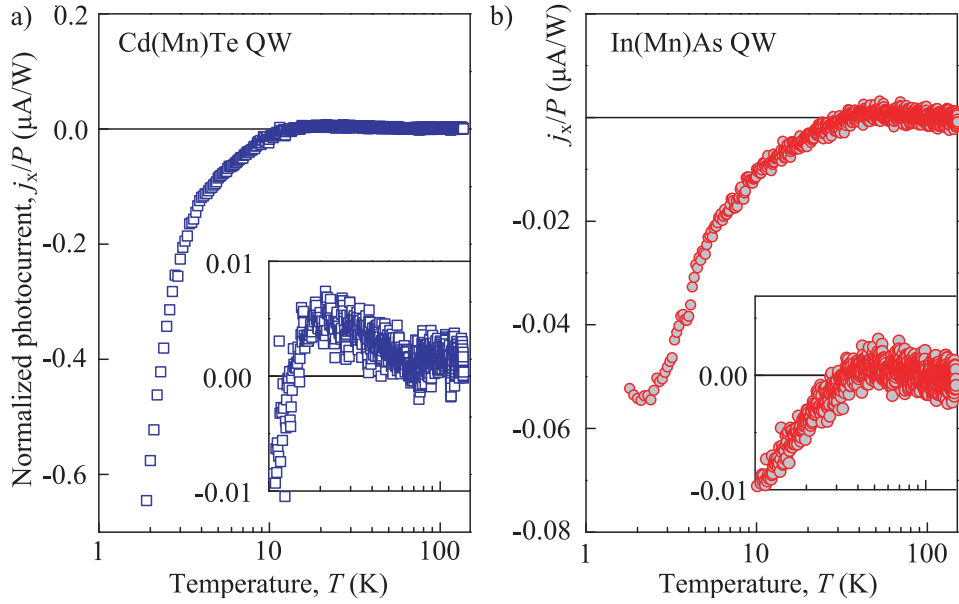


**Figure 14:** Temperature dependency of the normalized photocurrent $j_x/P$ at a fixed magnetic field value of $B_y = 2$ T. The incident radiation was linearly polarized with a wavelength of 118.8 $\mu$m. Panel (a) and (b) correspond to the Cd(Mn)Te and the In(Mn)As DMS QW sample. The insets depict a zoom of the photocurrent in the temperature range of 10 to 150 K. While the photocurrent of the Cd(Mn)Te sample shows a zero crossing at approximately 12 K, no change of sign is detected for the In(Mn)As sample.

Similar results have been obtained for different wavelengths with frequencies even ranging into the microwave spectrum. These findings are not presented here but can be viewed in Refs. [19, 57, 58]. In addition, experimental observations on different DMS heterostructures are discussed in the mentioned references. These structures comprise CdTe and InAs based DMS samples varying e.g., in the manganese concentration or layer design and include $n$-type In(Mn)As hybrid structures as well.

| sample | carrier density (cm$^{-2}$) | mobility (cm$^2$/Vs) | design |
|--------|------------------|------------------|--------|
| Cd(Mn)Te | $6.2 \times 10^{11}$ ($n$-type) | 16000 | square |
| In(Mn)As | $4.4 \times 10^{11}$ ($p$-type) | 2000 | square |
|  | effective $g$ factor | $N_0\alpha_{e/h}$ (eV) | $\bar{x}$ |
| Cd(Mn)Te | -1.64 | 0.22 | 0.013 |
| In(Mn)As | -15 | -1 | 0.01 |

**Table 3:** Parameters of the two investigated DMS samples. Carrier density and mobility are obtained at 4.2 K without illumination. Effective $g$ factor and exchange integral $N_0\alpha_{e/h}$ for electrons (e) and holes (h) are obtained from Ref. [18] and Refs. [59, 60] for Cd(Mn)Te and In(Mn)As, respectively. $\bar{x}$ represents the effective manganese concentration in the QW [19, 50].

## 4.2   Discussion

The experimental results of the THz radiation induced photocurrents in DMS structures can be well explained by the magnetogyrotropic photogalvanic effect. In fact, they provide a direct experimental proof for the spin related mechanism based on the zero bias spin separation (see Section 2.2). Spin polarized current generation is possible by illuminating an unbiased QW structure with THz radiation. This results in a homogeneous heating of the electron gas. The relaxation of carriers is asymmetric in $\boldsymbol{k}$-space and yields an electron flux in each spin subband $\boldsymbol{j}_+$ (spin-up) and $\boldsymbol{j}_-$ (spin-down) of equal strength but oppositely directed. For zero magnetic field these fluxes form a pure spin current according to Eq. (11). By the application of an external magnetic field these two fluxes get unbalanced and result in a measurable net electric current

$j_Z$, which is proportional to the Zeeman splitting (see Eq. (13)). This proportionality was the reason to choose DMS structures in order to establish the spin dependent features of the MPGE as the Zeeman splitting can be varied in a controllable way via the magnetic properties of the DMS system. This can be done e.g., by choosing different host materials or by variation of the $Mn^{2+}$ concentration or temperature. Due to the interaction of the free carriers with the $Mn^{2+}$ ions there is an additional term in the Zeeman splitting:

$$E_Z = E_Z^{intr.} + E_Z^{Giant} = g\mu_B B + \bar{x} S_0 N_0 \alpha_{e/h} B_{5/2}(\frac{5\mu_B g_{Mn} B}{2k_B(T_{Mn} + T_0)}). \quad (21)$$

The first term on the right-hand side corresponds to the intrinsic Zeeman splitting (see Eq. (12)). The second term stems from the exchange interaction of electrons (holes) with the $Mn^{2+}$ ions and is often referred to as Giant Zeeman term. Herein, $\bar{x}$ is the effective average $Mn^{2+}$ concentration, $N_0 \alpha_{e/h}$ is the exchange integral for electrons (holes) and $B_{5/2}(\xi)$ is the modified Brillouin function [18, 41]. This modified Brillouin function describes the magnetization behavior of the manganese spin system. It is characterized by a strong temperature dependency and a saturating behavior at high external magnetic fields and low temperatures [18]. $g_{Mn}$ is the effective Landé factor of manganese, $k_B$ the Boltzmann constant and $T_{Mn}$ the temperature of the $Mn^{2+}$ spin system. $S_0$ and $T_0$ take into account the Mn-Mn antiferromagnetic interaction. The MPGE yields a photocurrent proportional to the Zeeman splitting ($j_Z \propto E_Z$), consequently all the characteristics of the studied photocurrents can be explained by Eq. (21) e.g., the drastic change of the amplitude with the temperature, the change of sign (in case of Cd(Mn)Te) and the saturation. All these findings result from the interplay of intrinsic and Giant Zeeman contribution, depending on which part dominates.

For high temperatures $E_Z^{intr.}$ dominates. Hence, the current has a pure linear dependency on $B_y$ and only a weak dependency on $T$. By contrast, for low temperatures the current is driven by $E_Z^{Giant}$ which saturates for high magnetic fields. In the case of Cd(Mn)Te these two contributions have different signs ($g < 0, N_0\alpha_e > 0$) [18]. This results in the observed zero crossing (see inset in Fig. 14 (a)). At this point both contributions have the same magnitude, thus $E_Z^{intr.} = E_Z^{Giant}$. For the In(Mn)As sample both terms are negative
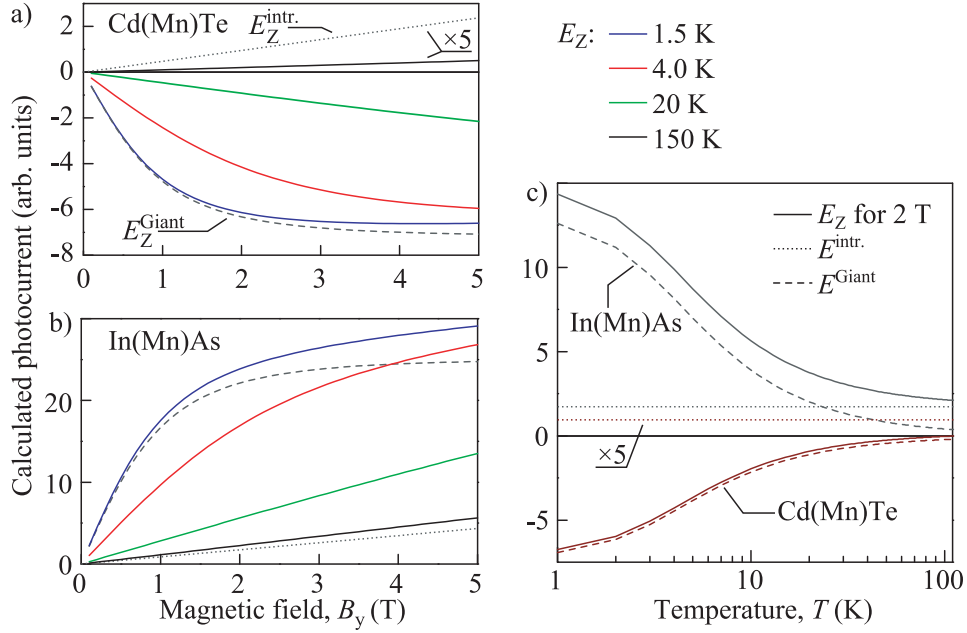
**Figure 15:** (a) Magnetic field dependency of the calculated photocurrent contributions $E_Z^{intr.}$ (dotted) and $E_Z^{Giant}$ (dashed, $T = 1.5$ K) for Cd(Mn)Te. Here, $E_Z^{intr.}$ is assumed to be temperature independent. The sum of both terms, $E_Z$, is shown for temperatures of 1.5, 4.0, 20 and 150 K. For a better comparison the curves of $E_Z$ for 150 K and $E_Z^{intr.}$ are multiplied by a factor of 5. (b) depicts the same calculated contributions for In(Mn)As. (c) presents the temperature dependency of the calculated photocurrent contributions, as well as the sum for a magnetic field value of 2 T. All curves are calculated using Eq. (21) and the parameters from Tab. 3.

$(g < 0, N_0 \alpha_h < 0)$ [59–62]. Hence, the photocurrent exhibits no change of sign (see inset in Fig. 14 (b)).

Figure 15 depicts theoretical calculations of the photocurrent contributions for both samples after Eq. (21). These are in very good agreement with the measured curves shown in Figs. 13 and 14. The curves are obtained for literature values of parameters which are summarized in Tab. 3. Note, that the current $\boldsymbol{j}$ is only proportional to $E_Z$ so that the definite sign of the measured photocurrent does not have to be the same as for the calculations (e.g., Figs. 13 (b) and 15 (b)).

The observed increase of the photocurrent with a decrease of temperature can not be explained by the Giant Zeeman effect alone: additional measurements of photoluminescence for the Cd(Mn)Te sample yield a value for Zeeman spin splitting of 2.6 meV for 3 T and 4.2 K. The intrinsic value, which is valid for higher temperatures, is given by $g\mu_B B = $ -0.28 meV. Hence, the current should increase by a factor of approximately 10 when the sample is cooled down from e.g., 40 to 4.2 K at 3 T. By contrast, the THz radiation induced photocurrent increases by a factor of approximately 100. This indicates that a second mechanism plays a role for the current generation in DMS structures.

So far only the current generation based on the Zeeman splitting of the electron subbands was considered (MPGE). However, there is a second mechanism for the conversion of the electron fluxes $\boldsymbol{j}_\pm$ which is specific for DMS structures: the spin dependent scattering of carriers by polarized $Mn^{2+}$ spins [18,63]. This effect is described by an extra Hamiltonian which takes into account the electron and manganese ion interaction by a spin dependent scattering potential. The two electron fluxes ($\boldsymbol{j}_+ = -\boldsymbol{j}_-$, from the zero bias spin separation) are proportional to the momentum relaxation time $\tau_\pm$. By applying an external magnetic field the manganese ions get polarized. This leads to different scattering rates for spin-up and -down electrons and to unequal momentum relaxation times $\tau_+ \neq \tau_-$. Consequently the fluxes do not compensate each other anymore yielding an additional net electric current $\boldsymbol{j}_{Sc}$. Assuming that the electron scattering by the $Mn^{2+}$ potential $u$ is larger than the exchange term described by $\alpha$ the second current contribution is given by [63]

$$\boldsymbol{j}_{Sc} = 4e\frac{\alpha}{u}\boldsymbol{j}_s S_{Mn}. \tag{22}$$

Herein, $S_{Mn} = -S_0 B_{5/2}(\xi)$ is the average manganese spin along the magnetic field direction.

Thus, the total net electric current in DMS structures is given by: $\boldsymbol{j} = \boldsymbol{j}_Z + \boldsymbol{j}_{Sc}$. As both contributions have their origin in the polarization state of the $Mn^{2+}$ spin system, the total current $\boldsymbol{j}$ will follow the Brillouin function.

It should be mentioned that for the In(Mn)As DMS sample a tiny positive photocurrent was detected for $T = 40$ K (see Fig. 13 (b)). This observation conflicts with the here presented theory. However, a possible explanation is the

interplay of the negative spin photocurrent of the MPGE and a positive orbital photocurrent [64, 65]. Further investigations are needed in order to verify this explanation and is out of scope of this thesis.

## 4.3   Brief Summary

The results on terahertz radiation induced photocurrents in diluted magnetic semiconductors clearly show that their microscopic origin is due to a spin dependent asymmetric scattering of carriers, yielding a pure spin current. In the presence of an external magnetic field this pure spin current can be converted into a net electric current which is proportional to the Zeeman splitting of the subbands. As the Zeeman splitting in DMS structures is drastically enhanced due to the exchange interaction of free carriers with the manganese ions, the currents receive a giant enhancement, too. In addition, the mechanism of current generation is amplified by the spin dependent scattering of carriers on polarized manganese ions.

# 5 Dirac Fermion System at Cyclotron Resonance

In this chapter studies of cyclotron resonance assisted photocurrents induced by terahertz radiation in HgTe quantum well systems will be presented. It mainly refers to QW structures close to the critical width $L_C$, where the energy spectrum is predicted to be characterized by a linear dependency. Therefore, samples with a QW width of 6.6 nm were selected for the photocurrent measurements. Complementary measurements on THz photoresistance and radiation transmittance were also performed.

The focus of the measurements lies on cyclotron resonance and on the experimental proof of the dispersion linear in $\boldsymbol{k}$ i.e., the results will be discussed in detail by means of CR and band structure theory. Furthermore, a microscopic model for current generation in a Dirac fermion system will be presented. The experimental results of this chapter are published in Refs. [14, 15].

## 5.1 Terahertz Induced Photogalvanic Effects

In the following results for THz radiation induced photocurrents in HgTe QWs without and with an external magnetic field will be presented. In both cases the unbiased sample was illuminated under normal incidence with radiation of a wavelength of $\lambda = 118.8$ $\mu$m at helium temperature. The experimental geometry and signal detection is illustrated in Section 3.3.2.

Three different states of the 6.6 nm QW square shaped sample were studied: the initial state with hole density $p_1$ and two electron density states $n_1$ and $n_2$ achieved by optical doping [14]. For optical doping the sample in its initial state is illuminated with a red light emitting diode ($\lambda = 630$ nm) for a finite time $t_1 \approx 15$ s. By this illumination not only the carrier density but also the carrier type changes to $n_1$ due to the persistent photoconductivity effect [54, 55]. Illuminating the sample further the carrier density saturates after approximately 80 s yielding carrier density $n_2$. Typical results of magneto-transport measurements can be seen in Fig. 8 (b) for the two different illumination states $p_1$ and $n_2$. The figure shows well pronounced Shubnikov-de Haas oscillations in the

longitudinal resistance $R_{xx}$ and Hall plateaus in the Hall resistance $R_{xy}$. The change of carrier type can easily be seen by the different slopes of the Hall resistance in the upper and lower panel.

### 5.1.1  Photocurrents at Zero Magnetic Field

The first measurements of photocurrents in HgTe QWs were performed for samples with a width of 6.6 nm and linearly polarized THz radiation at zero magnetic field. The polarization dependency on the direction of the electric field plane was determined for all three carrier densities. Varying the angle $\alpha$ - given by the linear polarization plane and the $x$ direction, defined in the inset of Fig. 16 (b) - an oscillating photosignal can be detected for $x$ and $y$ direction which follows a sine/cosine dependency according to

$$U_i(\alpha)/P = A + B sin(2\alpha) + C cos(2\alpha), \tag{23}$$

with $i = x, y$. This is shown for $U_y/P$ in $y$ direction in Fig. 16 (a). The fit curves according to Eq. (23) are depicted in Fig. 16 as solid lines. The largest signal is obtained for the carrier density $n_1$ with an average photosignal of 0.91 mV/W. The photosignals of the sample states $p_1$ and $n_2$ have mean values of 0.16 and 0.03 mV/W, respectively. For a better comparison some curves in Fig. 16 (a) were scaled by factors indicated in the figure. The parameters of the studied sample are presented in Tab. 4 giving information on e.g., carrier densities and illumination time $t_i$ of optical doping. The fitting parameters $A$, $B$, and $C$ of Eq. (23) are given in Tab. 6.

In addition to the 6.6 nm QW square sample a structure with a QW width of 21 nm characterized by an inverted parabolic band structure was studied as a reference for this part of the work. Similar to above the carrier density could be increased by optical doping (carrier densities are given in Tab. 4) but for this sample the conductance was $n$-type for both densities ($n_3$ and $n_4$). The obtained results at zero magnetic field $B$ as a function of the angle of the linear polarization plane $\alpha$ is shown in Fig. 16 (b). Experimental conditions were the same as for the 6.6 nm QW and again the photosignal shows an oscillating behavior and can be fitted with Eq. (23). The mean values of the normalized photosignal $U_y/P$ are for both carrier densities in the same order of magnitude
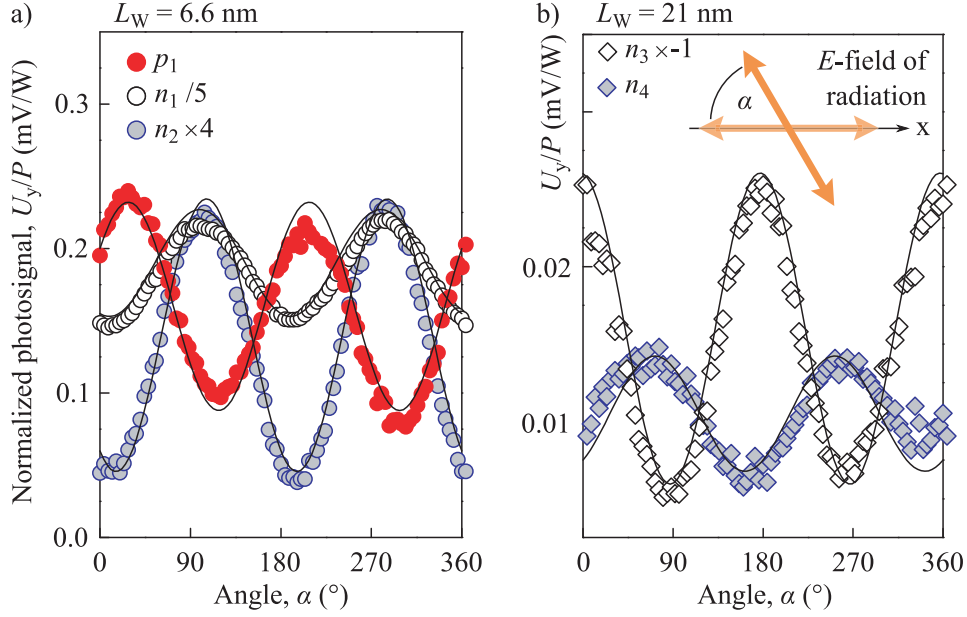
**Figure 16:** THz radiation induced photosignal $U_y$, normalized by laser power $P$, as a function of the angle $\alpha$ at 4.2 K and zero magnetic field for the (a) 6.6 and (b) 21 nm QW square samples. Radiation with a wavelength of 118.8 $\mu$m is applied normal to the QW layer. $\alpha$ describes the angle between the linear polarization plane and the $x$ direction, indicated in (b). Solid lines are fit functions according to Eq. (23) with parameters given in Tab. 6. Note, that some curves are scaled for a better comparison, indicated in the figure.

at -0.016 ($n_3$) and 0.011 mV/W ($n_4$). Exact fitting parameters are summarized in Tab. 6. Note, that the photosignal for $n_3$ was multiplied by -1 for a better comparison.

### 5.1.2   Cyclotron Resonance Assisted Photocurrents

Now photocurrents in the presence of an external magnetic field will be presented, namely under CR conditions. When illuminating the $p$-type 6.6 nm QW square shaped sample with THz radiation and sweeping an external magnetic field $B$ applied perpendicular to the QW plane a resonant photosignal was detected. The photosignals $U_y/P$ in $y$ direction are shown for all types of polarization and $\lambda = 118.8$ $\mu$m in Fig. 17. For linearly polarized radiation the

positions at which the well pronounced peaks occur are -0.44 and +0.40 T (see black curve). The magnitudes for both magnetic field polarities are similar: -9.93 and +7.98 mV/W for negative and positive $B$. When illuminating the sample with right-handed circularly polarized light ($\sigma^+$), the peaks stay at the same magnetic field values, but the photosignal amplitude changes: while the signal is increased for negative magnetic fields, it is decreased for positive $B$ values (see red curve in Fig. 17). In fact the resonant signal is about a factor of 4 larger for negative than for positive magnetic fields. The situation for left-handed circularly polarized light ($\sigma^-$, blue line) is vice versa. The measurements show that for a fixed radiation helicity ($\sigma^-$ or $\sigma^+$) only one dominant resonant peak appears - either for positive or negative $B$ values. Moreover, the normalized photosignal $U_y/P$ which is shown in Fig. 17 is an odd function
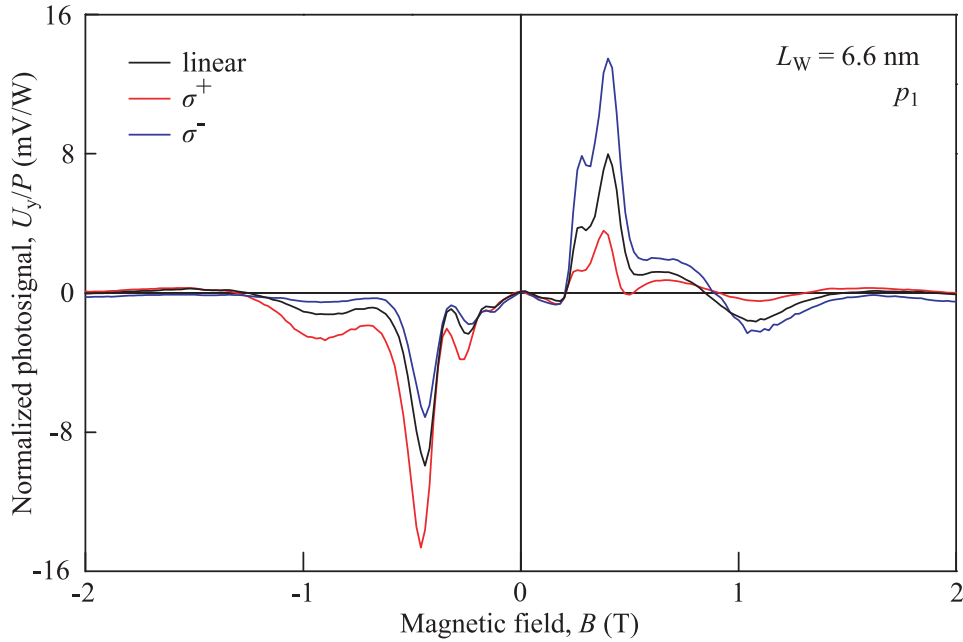


**Figure 17:** Magnetic field dependency of the normalized photosignal $U_y/P$ for the $p$-type 6.6 nm QW square sample at $T = 4.2$ K. THz radiation of $\lambda = 118.8$ $\mu$m was applied perpendicular to the sample with different polarizations: for linearly polarized light (black curve) the peaks for negative and positive $B$ have approximately the same amplitude. By contrast, $\sigma^+$ radiation (red curve) shows a much larger resonance for negative and $\sigma^-$ radiation (blue curve) for positive magnetic field values.

of the magnetic field $B$. A similar behavior is observed for the photosignals $U_x/P$ in $x$ direction (not shown). For reasons of simplification and because the THz radiation induced photocurrent has no predefined direction due to the low symmetry of the sample ($C_1$ point group) [24], in the following only the absolute value of the photosignal is presented. This is done according to $U/P = \sqrt{U_x^2 + U_y^2}/P$ in which both measured voltage drops are considered, as well as the normalization by the laser power $P$.



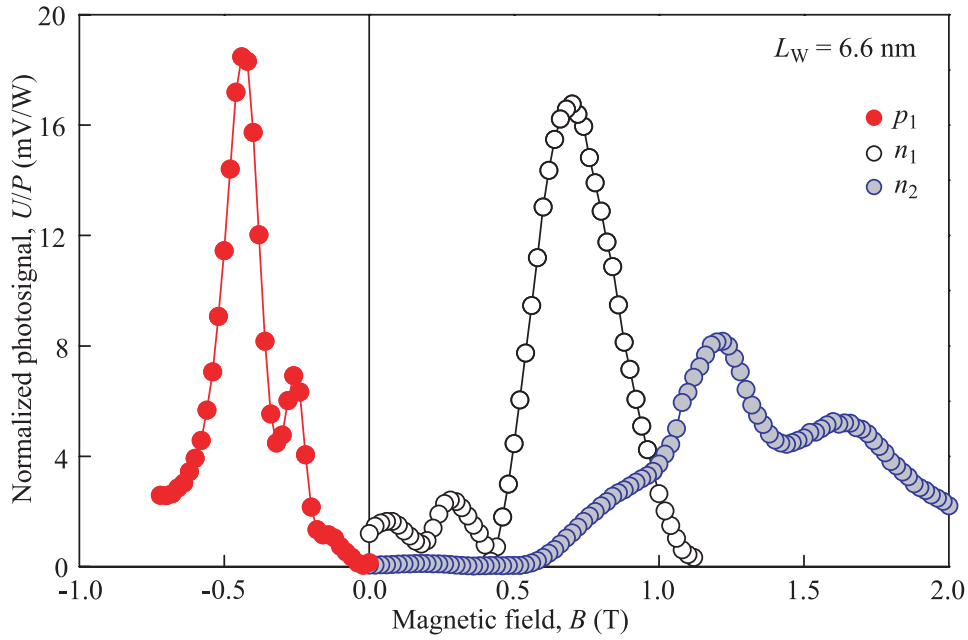**Figure 18:** Magnetic field dependency of the normalized photosignal $U/P$ for the 6.6 nm QW square sample with three different carrier densities. Right-handed circularly polarized radiation with $\lambda = 118.8\ \mu$m was applied normal to the QW layer at $T = 4.2$ K.

This normalized, absolute photosignal is shown for the $p$-type sample and for $\sigma^+$ radiation in Fig. 18 (red curve). Only the data in the vicinity of the pronounced peak position $B_c$ is shown, here at a negative magnetic field value of -0.44 T. The maximum signal $U_{max} = 18.47$ mV/W is by two orders of magnitude larger than at zero magnetic field $U_{B=0} = 0.15$ mV/W. When the carrier density is increased by optical doping to a value of $n_1 \approx 2 \times p_1$, the situation changes dramatically. For right-handed circularly polarized light the

resonant photosignal position $B_c$ jumps from negative to positive magnetic fields to a value of +0.70 T (see Fig. 18, black curve). The amplitude of $U/P$ for $n_1$ has a similar maximum amplitude of 16.76 mV/W, as for $p_1$. Repeating the same measurement for a carrier density of $n_2 \approx 3 \times n_1$ the peak appears at +1.20 T with a peak magnitude of 8.14 mV/W (blue curve). For left-handed circularly polarized light the situation is vice versa: while the $p$-type sample shows a resonant photosignal at positive magnetic fields (+0.38 T), both $n$-type samples show peaks at negative $B$ values (-0.78 and -1.20 T). These resonance positions are given in Tab. 4 as a mean value of $|B_c|$ for both radiation helicities.

In order to characterize the origin of the resonance phenomenon, additional measurements of radiation transmittance and photoresistance (see Section 5.2) were carried out. The setup is illustrated in Section 3.3.4. The results for circularly polarized radiation at a wavelength of $\lambda = 118.8$ $\mu$m and $T = 4.2$ K are depicted in Fig. 19. Sweeping the magnetic field a distinct peak in the normalized transmitted radiation was detected for all three carrier densities. The peak positions correspond to the magnetic field values at which the condition for CR is fulfilled. The most pronounced peak is observed for $n_2$. In that case the normalized transmittance decreases by approximately 25%, whereas

|        | $L_W$ (nm) | carrier density (cm$^{-2}$) | $t_i$ (s) | $\bar{B}_c^{PGE}$ (T) | $\bar{B}_c^{TM}$ (T) |
|--------|------------|------------------------------|-----------|------------------------|------------------------|
| $p_1$  | 6.6        | $1.5 \times 10^{10}$ ($p$-type ) | -         | 0.41                   | 0.42                   |
| $n_1$  | 6.6        | $3.4 \times 10^{10}$ ($n$-type) | 15        | 0.74                   | 0.74                   |
| $n_2$  | 6.6        | $11 \times 10^{10}$ ($n$-type)  | 80        | 1.20                   | 1.16                   |
| $n_3$  | 21         | $18 \times 10^{10}$ ($n$-type)  | -         | 2.28/2.74              | 2.31/2.91              |
| $n_4$  | 21         | $24 \times 10^{10}$ ($n$-type)  | 80        | 2.38/2.74              | 2.31/2.88              |

**Table 4:** Carrier densities and types of the 6.6 and 21 nm QW square samples. The parameters were obtained at 4.2 K for different illumination states of the sample. $t_i$ is the duration of the illumination by a red light emitting diode, used for the optical doping. The last two columns present the magnetic field values of the resonance position $B_c$, observed in the photocurrent and transmission measurements. Magnetic field positions have been averaged over the absolute value of $\bar{B}_c$ for $\sigma^+$ and $\sigma^-$ measurements.
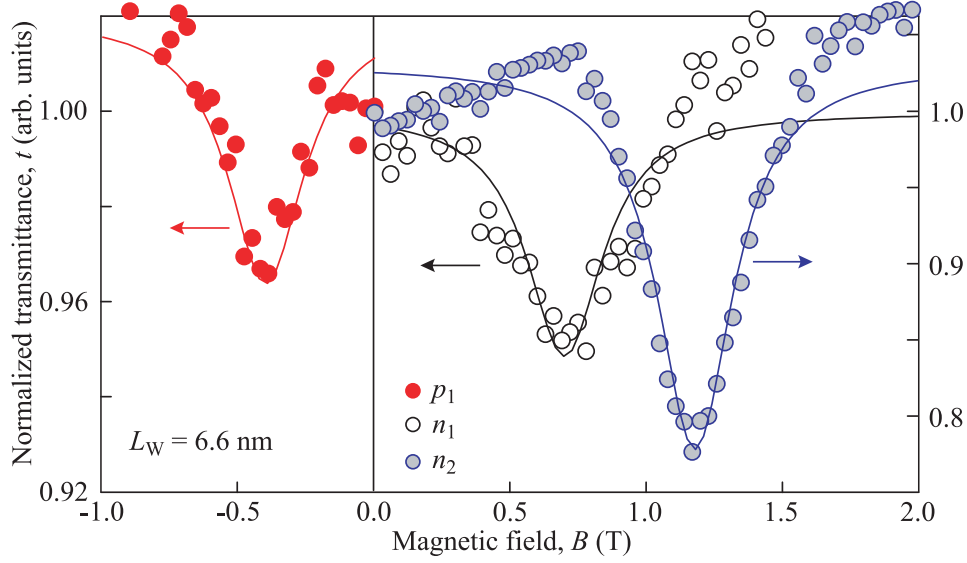
**Figure 19:** Normalized transmittance of circularly polarized radiation as a function of the magnetic field $B$ for the 6.6 nm QW square sample with three different carrier densities. Radiation with $\lambda = 118.8$ $\mu$m was applied normal to the QW layer at $T = 4.2$ K. Note, that the curves of $p_1$ and $n_1$ scale on the left, while the signal for $n_2$ scales on the right. Solid lines are Lorentzian fits according to Eq. (24) with parameters given in Tab. 7. In all three cases a resonant peak can clearly be seen, corresponding to the magnetic field value, where the cyclotron resonance condition is fulfilled.

for $p_1$ and $n_1$ the signal only drops by 4-5%. For this reason the radiation transmission curves for $p_1$ and $n_1$ scale on the left and the one for $n_2$ scales on the right. The center positions $B_c^{TM}$ of the observed resonances are -0.42, +0.72 and +1.17 T for $\sigma^+$ radiation and carrier densities of $p_1$, $n_1$ and $n_2$, respectively. The situation for $\sigma^-$ is vice versa, yielding resonance positions of +0.42, -0.75 and -1.14 T. The center positions are summarized in Tab. 4 as an average of the absolute values of positive and negative cyclotron resonance position. All radiation transmittance data were fitted by Lorentzian curves given by

$$\mathcal{F}(B) = o \pm \frac{2a}{\pi} \frac{w}{w^2 + 4(B - B_c)^2}, \tag{24}$$

with offset $o$, amplitude $a$, width $w$ and center position $B_c$, shown as solid lines in Fig. 19. Exact fitting parameters of Eq. (24) are given in Tab. 7.

A 21 nm QW square sample, characterized by an inverted parabolic band structure, was investigated by THz radiation induced photocurrents and radiation transmittance. The photosignal is shown for $\sigma^+$ radiation with a wavelength of $\lambda = 118.8$ $\mu$m as a function of the magnetic field $B$ in Fig. 20 (a). For the initial carrier density $n_3 = 18 \times 10^{10}$ cm$^{-2}$ two peaks are observed at much higher magnetic fields $B_c$ than for the 6.6 nm QW sample: +2.30 and +2.78 T. For negative magnetic fields the resonant signal is less pronounced and by about a factor of 3 smaller. Therefore, the curves are limited to positive magnetic fields. Increasing the carrier density by optical doping to $n_4 = 24 \times 10^{10}$ cm$^{-2}$ almost no shift of resonance position is observed ($B_c = +2.44$ and +2.78 T), in contrast to the behavior of the 6.6 nm sample. For $\sigma^-$ polarized light the peaks occur at -2.26 and -2.70 T for $n_3$ and at -2.32 and -2.70 T for $n_4$.
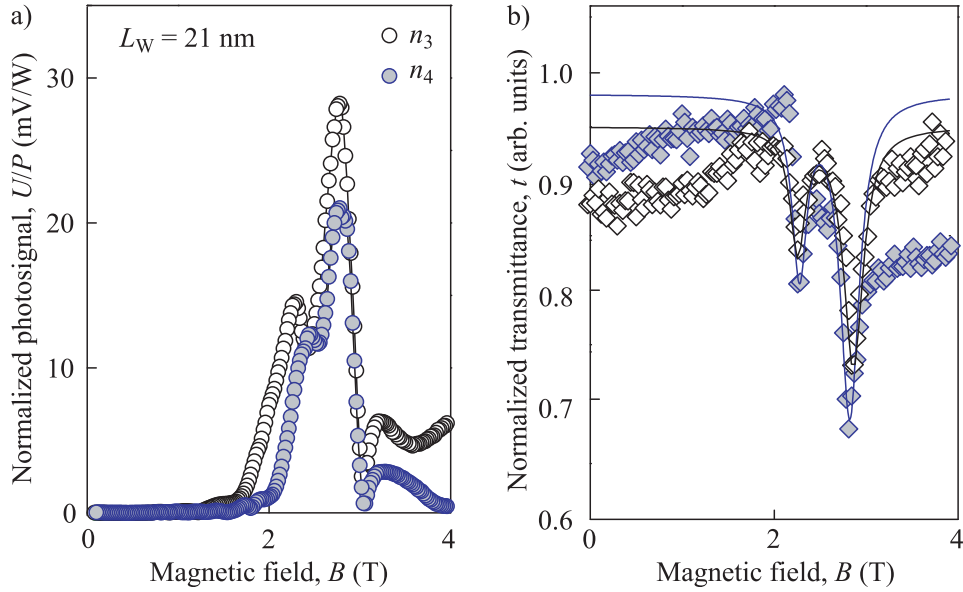


**Figure 20:** (a) Normalized photosignal $U/P$ as a function of the normal applied magnetic field $B$ for the 21 nm QW square sample with two different carrier densities. The sample was illuminated by right-handed circularly polarized light of normal incidence with $\lambda = 118.8$ $\mu$m at $T = 4.2$ K. (b) shows the corresponding measurement of radiation transmittance. Solid lines in (b) are Lorentzian fits according to Eq. (24) with parameters given in Tab. 8.

The results for radiation transmittance are similar to those of the photocurrent measurements and are illustrated in Fig. 20 (b) for right-handed circularly polarized light: the splitting of the resonance is clearly resolved at 2.31 and 2.91 T for $n_3$ and at 2.31 and 2.88 T for $n_4$. The normalized transmittance decreases by $\approx 15\%$ for the first and by $\approx 25\%$ for the second resonant peak. They can be nicely fitted by two Lorentzian curves using Eq. (24). Exact fitting parameters are given in Tab. 8. For negative magnetic fields no cyclotron resonance is detected; for left-handed circularly polarized radiation the situation is vice versa.

The resonance positions estimated from photocurrent and transmittance measurements are given in Tab. 4 as an average value of $|B_c|$ for both radiation helicities.

## 5.2   Photoresistance Measurements

The effect of cyclotron resonance has also been studied by THz photoresistance, which supports the measurements of radiation transmittance of the last section. These measurements were performed in close cooperation with Dimitry Kvon[1] and Vasily V. Bel'kov[2]. Two Hall bar structures with different HgTe QW widths $L_W = 6.4$ and 6.6 nm were investigated; both are close to the predicted critical width $L_C$ [11]. The setup was according to the description in Section 3.3.3 and the obtained results are published in [14].

---

[1]Institute of Semiconductor Physics, Novosibirsk, Russia
[2]Ioffe Institute, St.Petersburg, Russia

|       | $L_W$ (nm) | carrier density (cm$^{-2}$) | $B_c$ (T) |
|-------|-----------|-----------------------------|-----------|
| $n_5$ | 6.6       | $1.7 \times 10^{10}$        | 0.29      |
| $n_6$ | 6.6       | $7.2 \times 10^{10}$        | 1.03      |
| $n_7$ | 6.4       | $1.8 \times 10^{10}$        | 0.40      |

**Table 5:** Carrier densities of the 6.4 and 6.6 nm QW Hall bar samples obtained at 4.2 K by magneto-transport measurements and corresponding magnetic field values $B_c$ of the cyclotron resonance position.

Illuminating the biased 6.6 nm QW Hall bar sample in its initial state $n_5$ with THz radiation and sweeping an external magnetic field a resonant change of the resistance was observed. This is shown in Fig. 21 (a) for linearly polarized THz radiation of $\lambda = 118.8\ \mu$m. The resonance with an amplitude of $\Delta R_x = 2.73\ \Omega$ is detected at a magnetic field value of $+0.29$ T and corresponds to the position of cyclotron resonance. When the initial carrier density is increased to a value of $n_6 \approx 5 \times n_5$ by optical doping the cyclotron resonance position $B_c$ shifts to a value of $+1.03$ T. Here $\Delta R_x$ is given by 4.88 $\Omega$.

The 6.4 nm Hall bar sample with carrier density $n_7$ shows a change of resistance of $\Delta R_x = 2.36\ \Omega$ at a CR position of $+0.40$ T. This is shown in Fig. 21 (b).

The carrier densities and the corresponding CR positions $B_c$ are given in Tab. 5. All curves can be properly fitted by a Lorentzian curve according to Eq. (24),
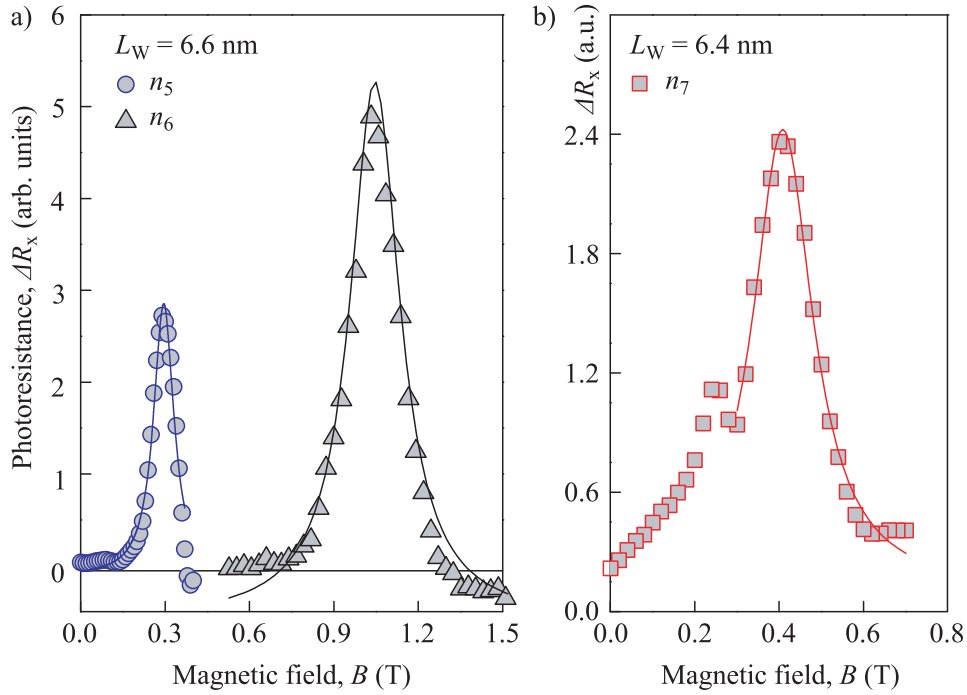


**Figure 21:**  Magnetic field dependency of THz photoresistance $\Delta R_x$ at 4.2 K and for $\lambda = 118.8\ \mu$m. (a) shows the results for the 6.6 nm QW Hall bar sample with two different carrier densities $n_5$ and $n_6$. (b) presents $\Delta R_x$ for the 6.4 nm QW Hall bar sample with carrier density $n_7$. Solid lines are Lorentzian fits according to Eq. (24).

depicted in Fig. 21 as solid lines. The exact fitting parameters are given in Tab. 9.

## 5.3   Discussion

The resonant THz radiation induced photocurrents of Section 5.1.2, as well as the surprising dependency of the resonance position on the carrier density are the main topic of this discussion. The same dependency was observed in radiation transmittance (see Section 5.1.2) and photoresistance (see Section 5.2) measurements, too. These results will be analyzed by cyclotron resonance theory and with reference to the unique band structure of HgTe (see Section 2.4 and 2.1). Furthermore, a microscopic model of current generation in systems characterized by a linear band structure will be presented which was developed parallel to the experimental work by Grigory V. Budkin[3] and Sergey A. Tarasenko[3] [15]. But before the CR assisted photocurrents will be discussed, photocurrents at zero magnetic field will be briefly addressed.

In the following only the main theoretical outcome of Ref. [15] will be introduced, as a detailed derivation of the equations is out of scope of this thesis.

### 5.3.1   Photocurrents at Zero Magnetic Field

Illumination of a 6.6 and 21 nm HgTe QW square sample with linearly polarized THz radiation results in a measurable electric current. When the angle of the linear polarization plane is varied, the photosignal oscillates as a function of sine and cosine (see Fig. 16). All curves can be well fitted by Eq. (23). Exact parameters of $A$, $B$ and $C$ (offset and prefactors of $\sin 2\alpha$ and $\cos 2\alpha$) are given in Tab. 6. While such a current has not yet been detected in 6.6 nm HgTe QWs, it was observed earlier for 21 nm HgTe QWs (see Refs. [24, 66]). Herein, the current is shown to be caused by the circular and linear photogalvanic effect (for reviews see Refs. [17, 67]). Considering a parabolic dispersion and a $C_1$ point symmetry, the dependency of the photocurrent on the linear polarization state for normal incidence of radiation and zero magnetic field is

---

[3]Ioffe Institute, St.Petersburg, Russia

given by [24]

$$j_x = \left[ X_{xxy} sin(2\alpha) - \frac{X_{xxx} + X_{xyy}}{2} + \frac{X_{xxx} - X_{xyy}}{2} cos(2\alpha) \right] I\eta,$$

$$j_y = \left[ X_{yxy} sin(2\alpha) - \frac{X_{yxx} + X_{yyy}}{2} + \frac{X_{yxx} - X_{yyy}}{2} cos(2\alpha) \right] I\eta,$$

(25)

with third rank tensor $\boldsymbol{X}$, angle of linear polarization $\alpha$, radiation intensity $I$ and radiation absorption coefficient $\eta$. All components of $\boldsymbol{X}$ are linearly independent and may be nonzero, due to the low symmetry of the (013) grown HgTe QWs. Just as in Ref. [24] these equations correspond exactly to the polarization dependency of the photosignal of the 21 nm QW sample (see Fig. 16 (b)). Moreover, they also describe the dependency for the 6.6 nm QW sample very well (see Fig. 16 (a)). For this reason a similar mechanism for the current generation can be expected in both samples, but this would need further measurements and analysis and is out of scope of this thesis.

|  | $L_W$ (nm) | $A$ | $B$ | $C$ |
|---|---|---|---|---|
| $p_1$ | 6.6 | 0.16 | 0.06 | 0.04 |
| $n_1$ | 6.6 | 0.91 | -0.09 | -0.14 |
| $n_2$ | 6.6 | 0.03 | -0.01 | -0.02 |
| $n_3$ | 21 | -0.016 | 0.001 | -0.010 |
| $n_4$ | 21 | 0.011 | 0.002 | -0.003 |

**Table 6:** Fit parameters of Eq. (23) for the photosignal as a function of $\alpha$ for the 6.6 and 21 nm HgTe QW sample (see Fig. 16). Note, that scaling factors are not included in this table.

### 5.3.2   Photocurrents and Photoresistance under Cyclotron Resonance Condition

For a magnetic field applied normal to the quantum well plane the THz radiation induced photosignals show a resonant behavior. This can be seen in Fig. 18 for the 6.6 nm QW sample for all investigated carrier densities $p_1$, $n_1$ and $n_2$. The observed peaks coincide very well with the positions of cyclo-

tron resonance in corresponding measurements of radiation transmittance (see Fig. 19). For an easy comparison both resonance positions $\bar{B}_c^{PGE}$ taken from photocurrent and $\bar{B}_c^{TM}$ obtained by transmission measurements, are summarized in Tab. 4. The average of the absolute value for positive and negative magnetic fields is listed. This good agreement indicates that the photocurrent is cyclotron resonance assisted. Additional support for this assumption comes from the dependency of the photosignal amplitude on the light's helicity for a certain carrier type. In Fig. 17 (hole density $p_1$) the peaks for the $\sigma^+$ photosignal are much more pronounced for negative than for positive magnetic fields. For radiation transmittance measurements the peaks arise for one helicity and magnetic field polarity only (not shown). This is in accordance with the theory of cyclotron resonance (see Section 2.4 and Eq. (16)): when radiation helicity and carrier type of a two dimensional electron (hole) gas are fixed, the power absorption of THz radiation by free carriers is only allowed for one magnetic field polarity.

The measurement of photoresistance is - next to radiation transmission - an established method for investigating the effect of cyclotron resonance. Therefore, it can be assumed that the peaks in the photoresistance (see Fig. 21) correspond to the magnetic field positions of CR.

The peak positions in Fig. 21 (a) for the 6.6 nm QW Hall bar sample show the same extraordinary dependency on the carrier density $n$, as the CR assisted THz radiation induced photocurrents and radiation transmittance (see Figs. 18 and 19). In Fig. 22 (a) the center positions $B_c$ of the photocurrent and photoresistance peaks are plotted as a function of the carrier density $n$, as square and dot data points.

Besides this surprising dependency of $B_c$ on $n$, the magnetic field values of CR are unusual small. Taking into account the used photon energy $E_{\hbar\omega} = 10.35$ meV and the effective mass of electrons in HgTe QWs of $m^*/m_e \approx 0.026$ - 0.034 [68], the magnetic field position of CR can be calculated according to [6]

$$B_c = \frac{E_{\hbar\omega}m^*}{\hbar e},\tag{26}$$

yielding values for $B_c$ between 2.34 and 3.02 T. By contrast, the experimental values are significantly smaller, they are all in the range of $|B_c| = 0.41$ - 1.2 T.

A possible explanation for these unexpected observations (shift of $B_c$ with carrier density and small effective masses) is the special energy spectrum of HgTe QW samples with the critical width $L_C$. This type of structure should have according to Refs. [10, 13] a linear energy spectrum with massless two dimensional Dirac fermions. Indeed, in such systems the cyclotron frequency is given by the well known expression $\omega_c = eB/m_c$. Herein, $m_c$ is the effective cyclotron mass at Fermi energy $E_F$. It is given by [69, 70]
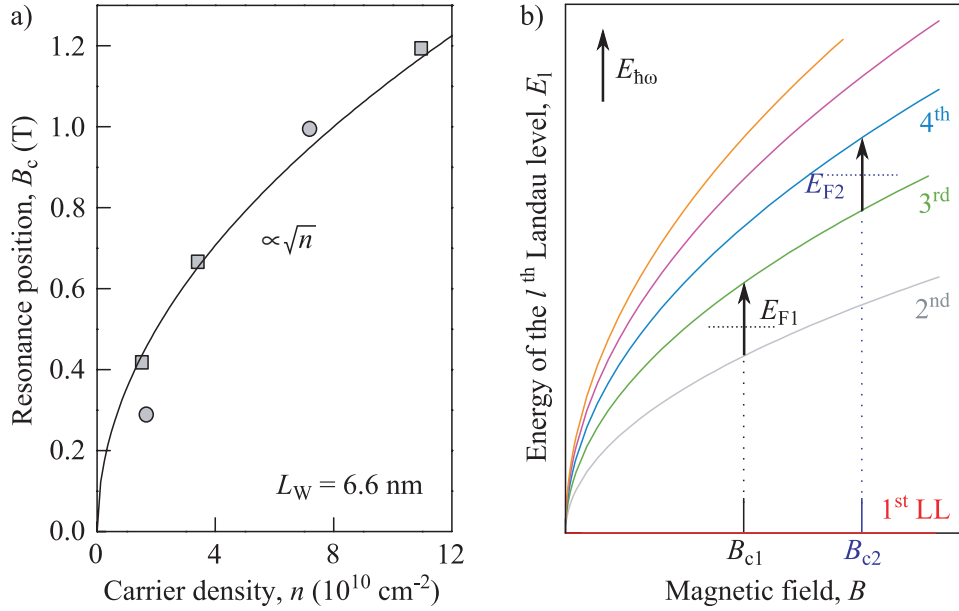
$$m_c = \frac{E_F}{v_{DF}^2},\tag{27}$$



**Figure 22:** (a) Dependency of the resonance position $B_c$ on the carrier density of the 6.6 nm QW samples. Values are taken from photoresistance (Hall bar sample, dots) and photocurrent (square sample, squares) measurements. The data show a square root dependency according to $B_c \propto \sqrt{n}$ (black line). (b) Splitting of Landau levels (LL) as a function of the magnetic field $B$. Zeeman splitting is neglected. Black arrows indicate a fixed photon energy $E_{\hbar\omega}$. In order to fit this energy to two different transitions (e.g., from $2^{nd}$ to $3^{rd}$ and from $3^{rd}$ to $4^{th}$ Landau level for Fermi energy $E_{F1}$ and $E_{F2}$, respectively), the magnetic field has to be increased.

with the constant velocity $v_{DF}$ of Dirac fermions. Taking into account the Fermi energy of massless two dimensional Dirac fermions [15]

$$E_F = \sqrt{2\pi n}(\hbar v_{DF}) \tag{28}$$

the CR position $B_c$ for a linear dispersion can be expressed as

$$B_c = \hbar\omega\frac{\sqrt{2\pi n}}{ev_{DF}}. \tag{29}$$

This dependency can be nicely seen in Fig. 22 (a). Even though the data points were obtained in different types of measurements on different samples and designs all data can be well described with a single curve proportional to $\sqrt{n}$ (Eq. (29)). The origin of this square root dependency can be found in the Landau level splitting of systems with a Dirac-like dispersion. In this special case the $l$-th Landau level is not given by the standard expression of Eq. (18) but by [13, 71–73]

$$E_l = sgn(l)v_{DF}\sqrt{2\,|l|\,\hbar eB}, \tag{30}$$

where $l \in \mathbb{N}$. Accordingly the Landau level splitting is not equidistant and is estimated to be

$$\Delta E_{l,l+1} = v_{DF}\sqrt{2\hbar eB}(\sqrt{l} - \sqrt{(l+1)}), \tag{31}$$

for the $l$-th and ($l$+1)-st Landau level.

The square root dependency of the $l$-th Landau level $E_l$ on the magnetic field $B$ (Eq. (30)) is shown schematically in Fig. 22 (b). For a carrier density $n_1$ with corresponding Fermi energy $E_{F1}$ a transition from second to third Landau level is induced by radiation with a fixed photon energy $E_{\hbar\omega}$. The photon energy is indicated by the black arrow. The magnetic field at which this transition occurs is $B_{c1}$ according to Eq. (31), with $\Delta E_{l,l+1} = E_{\hbar\omega}$. When the carrier density is increased to $n_2$ (Fermi energy $E_{F2}$) a transition from second to third Landau level is not possible anymore as the latter is completely populated for $B_{c1}$. Hence, the position of CR has to shift to a higher magnetic field value $B_{c2}$ in order to fulfill Eq. (31). Consequently the observed shift of the CR position $B_c$ with variation of the carrier density $n$ is a direct evidence that the energy

spectrum of the studied samples with $L_W = 6.6$ nm is that of two dimensional Dirac fermions.

On the basis of these observations the constant electron velocity $v_{DF}$ can be calculated according to Eq. (29). The obtained value of $7.17 \times 10^5$ m/s is almost constant for the different densities. The value is in good agreement with the electron velocity calculated in Ref. [13]. Moreover, the cyclotron masses $m_c$ of the 6.6 nm QW samples can be calculated according to Eq. (27). They are extraordinary small with values in the range of 0.003 to 0.012 $m_e$. They also show - similar to $B_c$ - a square root dependency on the carrier density according to Eq. (27) (not shown).

The significant higher resonance positions of approximately 2.30 and 2.90 T measured for the 21 nm QW sample (Fig. 20) are in accordance with the effect of CR for a QW system with parabolic dispersion. These CR positions correspond to effective masses of 0.026 and 0.032 $m_e$ obtained by Eq. (26) and lie within the range given in Ref. [68]. The negligible dependency of $B_c$ on the carrier density fit to the CR behavior of a normal parabolic dispersion with equidistant Landau level splitting, given by $\Delta E_{l,l+1} = \hbar\omega_c$. In this case the position of the resonance is independent of the Fermi energy as all transitions have the same energetic splitting (compare Section 2.4).

The observed two cyclotron resonance peaks measured by photocurrents and radiation transmittance for this 21 nm QW sample can be due to different effects (see Fig. 20). A similar splitting has also been observed in Ref. [74] in radiation transmittance experiments on a 15 nm HgTe QW. A possible explanation could be a second occupied subband and nonparabolic effects of the band structure [75]. Additional analysis is needed to isolate the origin of this splitting and is out of scope of this thesis.

It should be noted that a decrease of the QW width from 6.6 to 6.4 nm results in a noticeable shift of the resonance position to higher magnetic fields (from +0.29 to +0.40 T, see Fig. 21). This behavior allows the assumption that the latter QW has a narrow energy band gap with Dirac fermions of nonzero mass [14]. The critical width at which a Dirac-like energy spectrum should occur for HgTe QWs is according to Ref. [11] 6.4 nm. In this work the sample with $L_W = 6.6$ nm clearly shows properties of a Dirac-like linear band structure.

This small discrepancy in the critical width - 6.6 nm vs. 6.4 nm - may result from e.g., the different growth directions (the investigated samples in this work are (013) grown, whereas the sample in Ref. [11] is (001) grown), possible strain [76], layer design or substrate (here: GaAs, Ref. [11]: CdTe).

### 5.3.3   Microscopic Picture of Current Generation

On a first view the enhancement of the photosignals in Figs. 17 and 18 seems to stem from cyclotron resonance. For linearly polarized radiation the resonant photosignal shows an odd dependency on the external magnetic field (see Fig. 17). However, CR is an even function in $B$. This can be seen with Eq. (16) by the comparison of radiation absorption at CR position with the absorption far outside the resonance e.g., $\omega = 0$. From that comparison follows that radiation absorption is given by a term $\propto (\omega_c \tau)^2 \propto B^2$.

The momentum scattering time $\tau$ can be estimated from the full width $w$ at half maximum of the transmission measurements according to $\tau = 2m^*/we$, which can be derived with the help of Eqs. (16) and (24). For the 6.6 nm QW sample with carrier density $p_1$ (see Fig. 19) this gives values of $\tau \approx 0.15$ ps and $(\omega_c \tau)^2 = 5.69$. This means that at CR position the photosignal should be enhanced by a factor of 5.69 compared to zero magnetic field.

By contrast, the measured signal at resonance position $B_c = -0.44$ T is approximately two orders of magnitude larger than the signal at zero magnetic field ($U_{max}/P = 18.47$ mV/W and $U_{B=0}/P = 0.16$ mV/W, see Figs. 16 and 18). This large discrepancy leads to the conclusion that the resonant photosignal is not the signal at zero magnetic field enhanced by cyclotron resonance but implies that it is due to another microscopic root cause.

It is now shown that all observed experimental features can be well understood in the framework of the magnetogyrotropic photogalvanic effect (compare Section 2.2). This effect is well known from other systems like diluted magnetic semiconductor structures. Detailed results for DMS samples were reported in Chapter 4. Herein, a current was observed when the sample was illuminated with THz radiation and an external magnetic field was applied. The origin of this current is a spin dependent asymmetric scattering of carriers

in the Zeeman spin split parabolic subbands. The main difference to HgTe QW structures with a width of 6.6 nm is the fact that the latter has a linear band structure. However, the model of the MPGE can be adopted to a linear dispersion as well, which will be illustrated in the following.
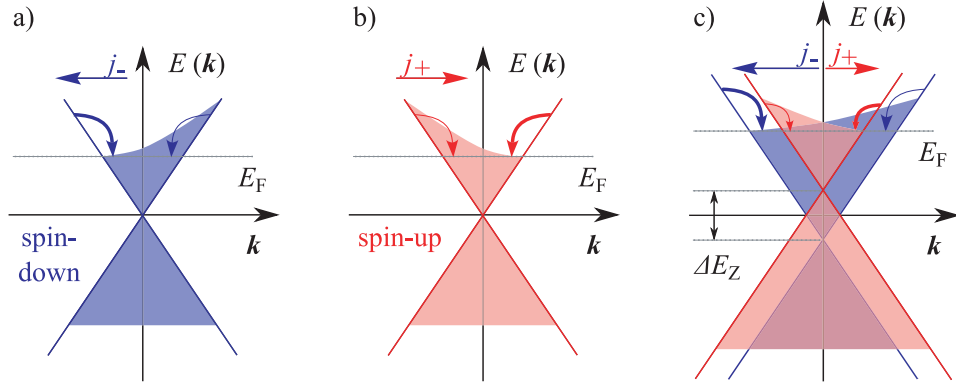


**Figure 23:** (a) and (b) show the spin-down and -up Dirac cone. The Fermi energy $E_F$ indicates up to which energy the cones are populated in equilibrium. The relaxation of the carriers heated by THz radiation is spin- and $k$-dependent, yielding an electron flux $\boldsymbol{j}_\pm$ in each spin cone. The different relaxation rates for positive and negative wave vectors are indicated by the arrows' thickness. c) By applying an external magnetic field the cones shift apart energetically. This Zeeman splitting is indicated by $\Delta E_Z$ and results in an imbalance of the population of the two cones. Consequently, $\boldsymbol{j}_-$ and $\boldsymbol{j}_+$ have different strengths.

The absorption of THz radiation results in a strong heating of the two dimensional electron (hole) gas. The matrix element of the electron-phonon interaction has an additional term for gyrotropic media (e.g., HgTe QWs [31]) which is proportional to the spin and wavevector i.e., $\propto \sigma_\alpha(k_\beta + k'_\beta)$, with Pauli matrices $\sigma$ and initial (scattered) wavevector $\boldsymbol{k}$ ($\boldsymbol{k}'$) (see Eq. (10)). Consequently, the energy relaxation of the carriers heated by THz radiation in each spin cone is asymmetric for positive and negative $\boldsymbol{k}$ (see Fig. 23 (a) and (b) for the spin-down and -up cone). Considering e.g., the spin-down cone ($\sigma < 0$), Eq. (10) yields a higher probability $W_{k,k'} \propto |V_{k,k'}|^2$ for scattering events of electrons with phonons for negative than for positive $\boldsymbol{k}$. Thus, more spin-down electrons with a negative wavevector *move* back towards $\boldsymbol{k} = 0$ resulting in

an electron flux $\boldsymbol{j}_-$ in negative $\boldsymbol{k}$ direction. The situation for the spin-up cone ($\sigma > 0$) is vice versa with a flux $\boldsymbol{j}_+$ in positive $\boldsymbol{k}$ direction. The two electron fluxes are oppositely directed and of equal strength ($\boldsymbol{j}_+ = \text{-}\boldsymbol{j}_-$), hence, they cancel each other out. The total net electric current is zero but a pure spin current is formed defined by Eq. (11).

This pure spin current can be converted into a net electric current by the application of an external magnetic field: the two spin cones split up in energy due to the Zeeman effect, which is illustrated in Fig. 23 (c). One spin cone is now preferentially populated. This results in an imbalance of the electron fluxes and gives rise to a measurable net electric current $\boldsymbol{j}_Z = \boldsymbol{j}_- + \boldsymbol{j}_+$.

Assuming that $E_F \gg k_B T$, $E_F \gg \Delta E_Z/2$ and $\omega_c \tau \gg 1$ the magnitude of the current can be estimated to [15]

$$|\boldsymbol{j}_Z| \propto \frac{ev_{DF}}{E_F \omega_c} \frac{\Delta E_Z}{E_F} \xi I \eta, \tag{32}$$

where $\xi$ takes into account the spin orbit interaction strength and $\eta$ the absorption in the vicinity of CR given by

$$\eta \propto \frac{E_F \tau}{\hbar} \frac{1}{1 + (\omega - \omega_c)^2 \tau^2}. \tag{33}$$

Equations (32) and (33) are valid for both parabolic and linear dispersions. The only difference exists in prefactors which are omitted here. Equation (33) contains the typical Lorentzian behavior of the cyclotron resonance, which can be seen in all measured signals: the photosignals clearly follow the spectral behavior of $\eta$ (see e.g., Fig. 18). Furthermore, the current $\boldsymbol{j}_Z$ given by Eq. (32) is proportional to the Zeeman splitting $\Delta E_Z = g\mu_B B$ and is therefore an odd function in the magnetic field, as shown in Fig. 17. Moreover, the current also depends on the spin orbit interaction strength $\xi$. Since the investigated samples are based on HgTe, which is characterized by a strong spin orbit coupling and a large effective $g$ factor [77], the current is additionally enhanced by these properties. This explains the increase by two orders of magnitude, observed in the experiment on cyclotron resonance assisted photocurrents in Fig. 18 for the $p$-type sample, whereas the radiation absorption only gives a factor of $\approx$ 6.

For the experimental setup, where the signals are measured via the voltage drop over a 10 MΩ load resistor which is much higher than the sample resistance, the photosignal is given by [15]

$$U = \left| j_Z \frac{\omega_c \tau a}{\sigma} \right|, \tag{34}$$

with the sample size $a$ and zero field conductivity $\sigma = e^2 E_F \tau/(2\pi\hbar^2)$. For a fixed radiation wavelength the dependency of the photosignal amplitude on the carrier density is estimated to [15]

$$U \propto \frac{g\tau}{\sqrt{n} v_{DF}^2}. \tag{35}$$

This is in accordance with the results shown in Fig. 18: by increasing the absolute value of the carrier density by approximately a factor of 7 (from $p_1$ to $n_2$) the maximum amplitude of the THz radiation induced photosignal $U/P$ decreases only by a factor of 2.3. This value is in good agreement with the factor $\sqrt{7} = 2.7$ which is obtained with Eq. (35). Thus, the above introduced microscopic model and theory can explain all experimental results of this chapter.

## 5.4   Brief Summary

The linear, Dirac-like character of the band structure of 6.6 nm HgTe QW structures could be verified by means of THz radiation induced photocurrents, THz radiation transmittance, and THz photoresistance assisted by cyclotron resonance. The observed shift of the CR position with variation of the carrier density (see Figs. 18, 19 and 21) can be explained unambiguously with the nonequidistant Landau level splitting of a Dirac fermion system, characterized by a linear dispersion.

In addition a microscopic model based on spin dependent scattering of electrons was introduced for the current generation in Dirac cones, which is related to the magnetogyrotropic photogalvanic effect described in Chapter 4. This microscopic model and the corresponding equations can explain all observed features - especially the large signals - of the photocurrent measurements.

The photocurrent described by Eq. (32) is proportional to the spin orbit interaction strength, the radiation absorption and the Zeeman splitting. All three contributing factors are enhanced in the system under study due to the measurement geometry and the material properties of the samples. Consequently, the measured signals are extraordinary large compared to those of conventional semiconductor structures. Considering the sample's resistance according to $I = U/R$ e.g., for the $n_2$ carrier density of the 6.6 nm HgTe QW sample, a current of 7.3 $\mu$A/W was measured for a magnetic field of +1.2 T. By contrast, for the Cd(Mn)Te DMS sample a maximum current was observed of only 0.69 $\mu$A/W for 3 T (see Fig. 13). Also for GaAs QW structures the typical magnitude of photocurrents is much less and lies in the range of 10 - 100 nA/W [78].

Furthermore, according to Eq. (32) these currents are proportional to the magnetic field, a dependency that is actually observed (see Fig. 17). The Lorentzian like behavior of these photocurrents stems from the spectral behavior of the absorption $\eta$ given in Eq. (33). Furthermore, the rather weak decrease of the photosignals' maximum amplitude with the increase of the carrier density from $p_1$ and $n_2$ (see Fig. 18) is in accordance with Eq. (35).

|       | offset $o$ | center $x_c$ | width $w$ | amplitude $a$ |
|-------|-----------|--------------|-----------|---------------|
| $p_1$ | 1.02 | 0.40 | 0.34 | 0.03 |
| $n_1$ | 1.00 | 0.70 | 0.34 | 0.03 |
| $n_2$ | 1.02 | 1.18 | 0.34 | 0.13 |

**Table 7:** Parameters of the Lorentzian fit curves according to Eq. (24) for the radiation transmission measurements of the 6.6 nm QW square sample (solid lines in Fig. 19).

| peak 1 | offset $o$ | center$_1$ $x_c$ | width$_1$ $w$ | amplitude$_1$ $a$ |
|--------|-----------|------------------|----------------|-------------------|
| $n_3$ | 0.95 | 2.31 | 0.20 | 0.04 |
| $n_4$ | 0.98 | 2.33 | 0.20 | 0.05 |
| peak 2 |  | center$_2$ $x_c$ | width$_2$ $w$ | amplitude$_2$ |
| $n_3$ |  | 2.93 | 0.26 | 0.09 |
| $n_4$ |  | 2.89 | 0.26 | 0.12 |

**Table 8:** Parameters of the Lorentzian fit curves according to Eq. (24) for the radiation transmission measurements of the 21 nm QW square sample (solid lines in Fig. 20 (b)).

|       | $L_W$ (nm) | offset $o$ | center $x_c$ | width $w$ | amplitude $a$ |
|-------|-----------|-----------|--------------|-----------|---------------|
| $n_5$ | 6.6 | -0.13 | 0.30 | 0.09 | 0.41 |
| $n_6$ | 6.6 | -0.52 | 1.04 | 0.21 | 1.75 |
| $n_7$ | 6.4 | 0.11 | 0.41 | 0.17 | 0.64 |

**Table 9:** Parameters of the Lorentzian fit curves according to Eq. (24) for the photoresistance measurements of the 6.6 and 6.4 nm QW Hall bar samples (solid lines in Fig. 21).

# 6 Quantum Oscillations in Mercury Telluride Quantum Wells

In this chapter the studies of quantum oscillation phenomena in HgTe based QW structures are presented and analyzed. The oscillations are detected in photocurrents and in the change of resistance, when illuminating the sample with terahertz radiation and sweeping an external magnetic field. As an important feature their envelope shows a nonmonotonic behavior. In order to get a good general view of these observations different kind of band structures were studied. This was achieved by investigating HgTe QWs with different widths ranging from 5 to 21 nm. Hence, all types of dispersion were available: normal and inverted parabolic, as well as a linear band structure. To explore the origin of the oscillations and the nonmonotonic behavior of their envelope function, the measurements of photocurrents are accompanied by measurements of photoresistance, magneto-transport and radiation transmission. The data are discussed on the basis of a microscopic model for current generation which gives a different view on the magnetogyrotropic photogalvanic effect, already introduced in the previous chapters. Quantum transport phenomena like the Shubnikov-de Haas and de Haas-van Alphen effect will also be considered in order to explain the mechanism of the oscillations. The results of this chapter are published in Ref. [20]. Note, that all photocurrent and photoresistance data i.e., their oscillations, are fully reproducible.

## 6.1 Experimental Results

All investigated samples of this chapter were characterized by standard magneto-transport measurements. The corresponding carrier densities, band stucture and design are summarized in Tab. 10. Furthermore, the samples are consecutively numbered. In particular, some samples (#3, #7) were already investigated in Chapter 5. First the data obtained for the 8 nm HgCdTe QW Hall bar sample #2 will be presented, which show the most pronounced oscillations in the photosignal and photoresistance. After that it will be shown that the os-

cillations can be found in square shaped, pure HgTe QW structures of various widths, too.

| sample | $L_W$ (nm) | band structure | carrier density (cm$^{-2}$) | design | $t_i$ (s) |
|--------|-----------|----------------|------------------------------|--------|-----------|
| #1 | 5 | normal | $24 \times 10^{10}$ | square | - |
| #2* | 8 | normal | $75 \times 10^{10}$ | Hall bar | - |
| #3 | 6.6 | linear | $11 \times 10^{10}$ | square | 80 |
| #4 | 6.6 | linear | $0.5 - 45 \times 10^{10}$ | Hall bar | - |
| #5 | 8 | inverted | $24 \times 10^{10}$ | square | - |
| #6 | 8 | inverted | $31 \times 10^{10}$ | square | 80 |
| #7 | 21 | inverted | $17 \times 10^{10}$ | square | - |

**Table 10:** QW width $L_W$, band structure, carrier density (obtained at 4.2 K) and design of the investigated samples. $t_i$ is the time of illumination with a red LED used for optical doping. Note, that samples #5 and #6 are the same but in two different illumination states. *The QW contains cadmium: $Hg_{0.86}Cd_{0.14}Te$.

### 6.1.1 Results for a Parabolic Dispersion

Exciting the 8 nm HgCdTe QW Hall bar sample #2 with THz radiation and sweeping an external magnetic field a signal was detected which shows a nonmonotonic behavior superimposed by oscillations. The magnetic field and the propagation direction of the linearly polarized THz radiation with $\lambda = 118.8$ $\mu$m were aligned normal to the QW plane. This photosignal $U_x/P$ is depicted in Fig. 24 (a) for $T = 4.2$ K. It features a maximum value at +2.78 T (-3.16 T for negative magnetic fields, not shown). Figure 24 also shows the corresponding longitudinal resistance with well pronounced Shubnikov-de Haas oscillations in black, scaled on the right. It can easily be seen that the oscillations in the photosignal follow the SdH oscillations quite nicely: when numbering the minima positions of the photosignal consecutively from 1 (minimum at $\approx 6.17$ T) to 7 (minimum at $\approx 2.5$ T) and plotting these as a function of the inverse magnetic field $1/B$ they can be nicely fitted by a straight line with a slope of 26.2 T. If the filling factors $v$ (see Section 2.5) of the SdH oscillations are displayed in the same manner they also show a linear behavior

on the inverse magnetic field with a very similar slope of 30.6 T. The good correlation between the two measurements is shown in Fig. 24 (c), where both filling factors $\upsilon$ are plotted vs. the inverse magnetic field. Note, that the signal $U_y/P$ along the $y$ direction shows a similar result. As this is the case for all measurements described in this chapter the presented figures are limited to one direction of voltage drop only (casually the $x$ direction).
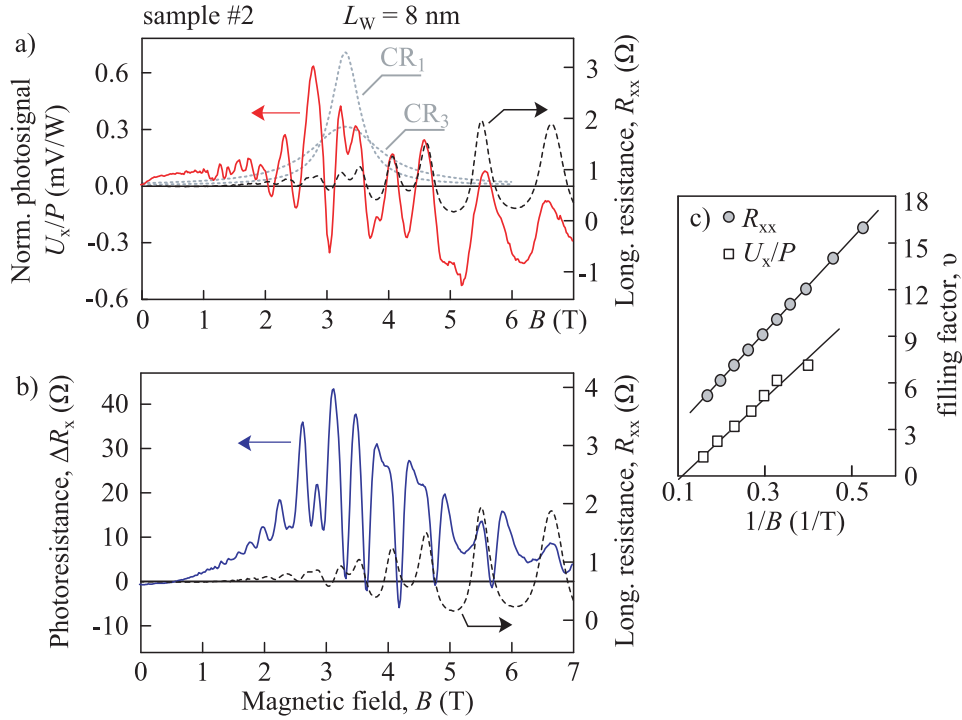


**Figure 24:** Results obtained for the 8 nm HgCdTe QW Hall bar sample #2 excited by linearly polarized radiation of $\lambda = 118.8$ $\mu$m at $T = 4.2$ K. (a) shows the photosignal $U_x$, normalized by radiation power $P$ induced in the unbiased sample. (b) presents the photoresistance $\Delta R_x$ for the biased sample. Black dashed curves show SdH oscillations of the longitudinal resistance $R_{xx}$ which scale on the right; gray dotted lines show the calculated CR absorption profile according to Eq. (45) for two different scattering times $\tau$ (1: 0.74 ps, 3: 0.3 ps, see Section 6.2.2). Filling factor $\upsilon$ vs. inverse magnetic field $1/B$ is depicted in (c) for SdH and photosignal minima. The latter is numbered consecutively with integers from 1 to 7.

A similar dependency is observed in the same sample for the THz photore-sistance $\Delta R_x$ shown in Fig. 24 (b). A maximum signal $\Delta R_x$ is observed for -3.14 and +3.12 T (again only the positive magnetic field range is shown). While oscillations in the photoconductivity with similar features have already been detected in HgTe based and other QW systems [79–81], oscillations in the photocurrent have not been observed so far.

To summarize, for both measurements, photocurrent and photoresistance, os-cillations and a nonmonotonic behavior of their envelope are observed i.e., the envelope has a distinct maximum. The results of Chapter 5 suggest that this maximum might stem from the effect of cyclotron resonance. In order to ver-ify this assumption, additional measurements were performed on large area square shaped samples. The measurements of photocurrent and photoresis-tance for various widths $L_W$ of pure HgTe QWs with a normal and inverted parabolic dispersions all show a similar behavior like sample #2. The results are shown in Figs. 25 - 27 with corresponding radiation transmittance and magneto-transport curves.

Figures 25 (a) and 26 (a) depict the results of the photocurrent and photoresis-tance measurement for the 8 nm pure HgTe QW sample #5. Both curves were obtained for $\sigma_+$ radiation with $\lambda = 118.8$ $\mu$m at liquid helium temperature. The photosignal shows pronounced oscillations and is enhanced in the vicinity of cyclotron resonance. The position of CR at about $B_c = 1.8$ T is detected by radiation transmission which is shown in Fig. 25 (b). The photosignal ex-hibits a maximum signal of 1.37 mV/W at a magnetic field of +2.26 T. For negative magnetic fields almost no signal is detected (not shown). In the case of left-handed circularly polarized light the results are vice versa.

The change of resistance $\Delta R_x$ shows the same features (Fig. 26 (a)). Data for two different measurement techniques are presented: the blue curve in panel (a) was measured by applying a *dc* current of either +1 or -1 $\mu$A and modulated THz radiation (method 1, see Section 3.3.3). The largest signal is detected at 1.94 T with $\Delta R_x = 134.45$ $\Omega$. Panel (b) illustrates the second technique. Herein, the longitudinal resistance $R_{xx}$ was measured via standard magneto-transport measurement (see Section 3.3.1) in the dark and in the presence of unmodulated THz radiation (method 2). These are depicted in black and red,
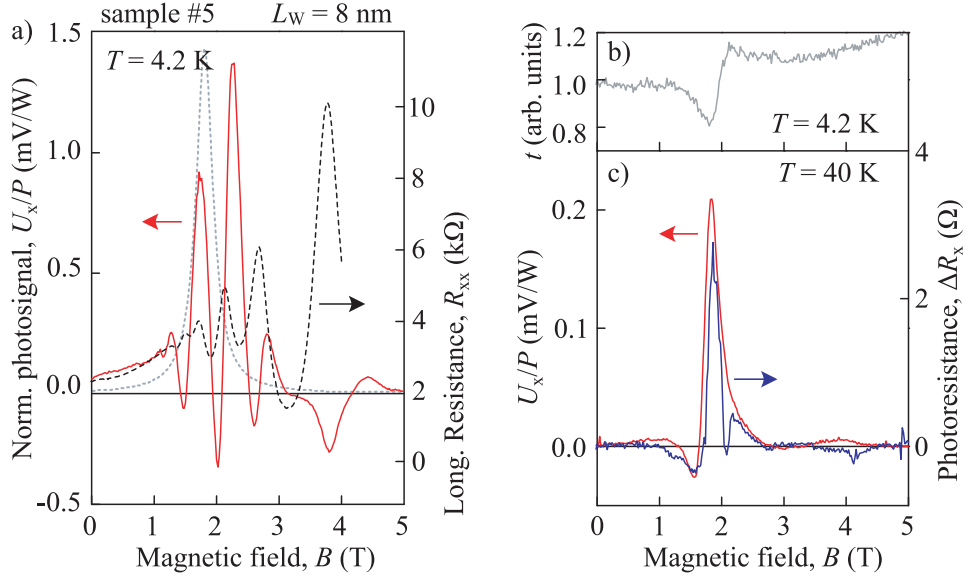
**Figure 25:** Measurements of the 8 nm QW square sample #5 obtained with $\sigma^+$ polarized radiation of $\lambda = 118.8\ \mu$m. The photosignal normalized by radiation power $U_x/P$ vs. the magnetic field $B$ is shown for (a) $T = 4.2$ K and (c) $T = 40$ K. The right scale in (a) presents the longitudinal resistance $R_{xx}$ at 4.2 K. The gray dotted line shows the corresponding calculated CR absorption profile according to Eq. (45) (see Section 6.2.2). The right scale in (c) shows the change of photoresistance $\Delta R_x$ at 40 K. (b) depicts the radiation transmission $t$ of the sample in arbitrary units at 4.2 K.

respectively. The difference of the two measured curves corresponds to the difference of resistance induced by THz radiation, namely the photoresistance $\Delta R_x$. This is shown in Fig. 26 (a), too, as a red line and is in good agreement with the curve obtained by standard method 1: the period of oscillations is the same and the largest signal of 183.88 $\Omega$ is obtained for the same magnetic field value of 1.94 T.

When the temperature was increased the oscillations became less pronounced. For $T = 40$ K they almost vanish revealing only one dominant peak at 1.84 T for the photosignal and at 1.86 T for the photoresistance measurement. This is shown in Fig. 25 (c). These positions coincide very well with the CR position as determined by radiation transmittance. For right-handed circularly polarized radiation the transmission decreases by approximately 20% at the CR position
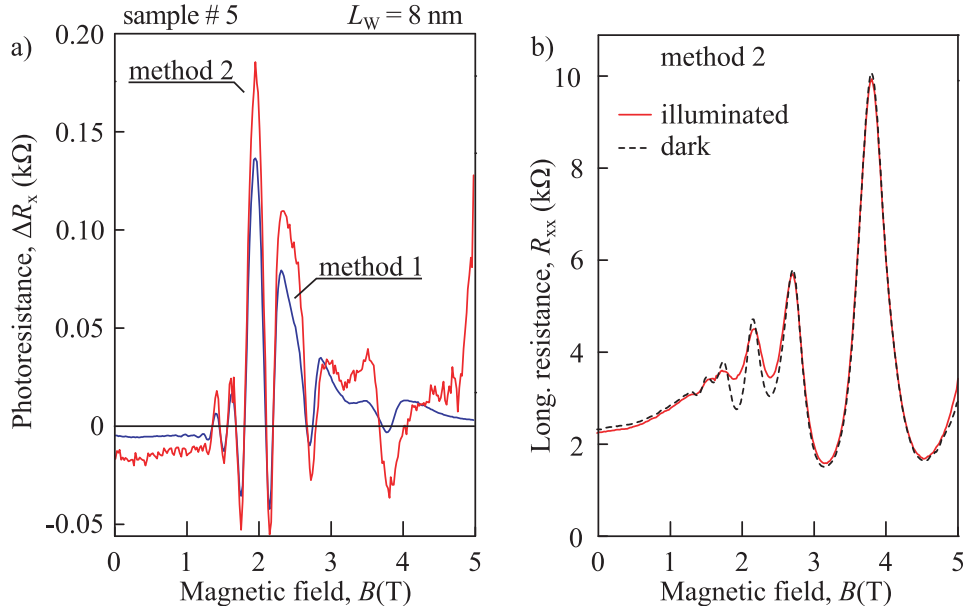
**Figure 26:** Photoresistance measurement of the 8 nm HgTe QW square sample #5 at $T = 4.2$ K and with THz radiation of $\lambda = 118.8\,\mu$m. (a) depicts the change of photoresistance $\Delta R_x$. The blue curve was obtained by method 1 for *dc* bias and modulated $\sigma^+$ radiation. The red curve is the difference of the two curves in (b), presenting the result of method 2 (*ac* current, unmodulated THz radiation). (b) shows the magneto-transport measurement of the longitudinal resistance $R_{xx}$ with well pronounced Shubnikov-De Haas oscillations. $R_{xx}$ was measured with and without unmodulated linearly polarized THz radiation (red and black, respectively).

of $B_c = +1.8$ T (see Fig. 25 (b)). Switching the radiation helicity from $\sigma^+$ to $\sigma^-$ cyclotron resonance occurs at $B_c = $ -1.76 T with a decrease of $\approx 22\%$ (not shown). The cyclotron resonance positions are summarized in Tab. 11 as an average of the absolute value of $B_c$ for both radiation helicities. The values are obtained from the high temperature photocurrent and low temperature radiation transmission measurements.

Similar results were observed for other samples with inverted (#6 and #7) and normal (#1) parabolic dispersion. The characteristic curves of the photosignal for $\sigma^+$ radiation at 4.2 and 40 K are shown for these samples in Fig. 27 (a)-(c). The data are accompanied by measurements of the longitudinal resis-
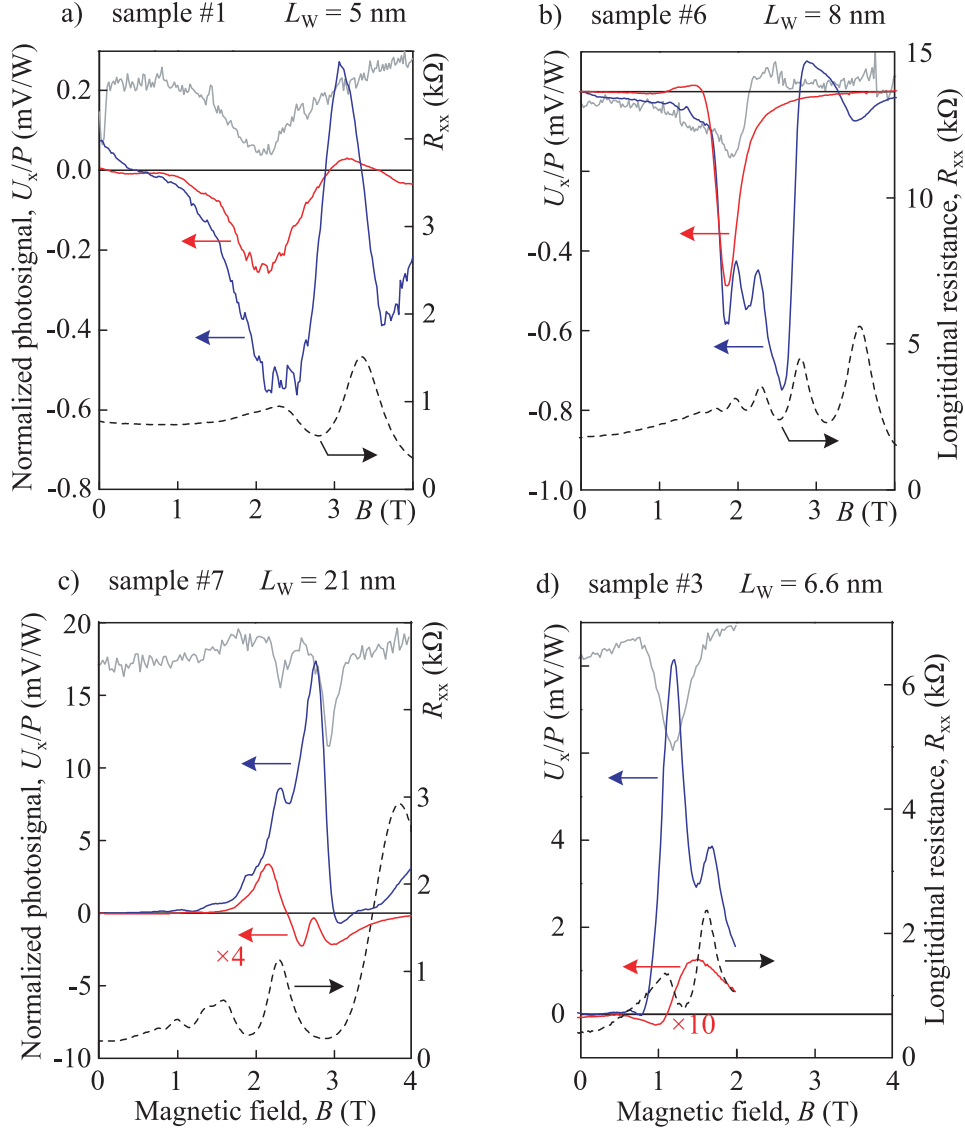
**Figure 27:** Photosignal normalized by radiation power $U_x/P$ (left scale) and longitudinal resistance $R_{xx}$ with SdH oscillations (right scale) for four different QW widths: (a) 5 nm QW sample #1, (b) 8 nm QW sample #6, (c) 21 nm QW sample #7 and (d) 6.6 nm QW sample #3. The photosignals were measured with $\sigma^+$ polarized radiation of $\lambda = 118.8\ \mu$m for two temperatures: $T = 4.2$ K (blue) and $T = 40$ K (red). THz radiation transmission is depicted in gray in arbitrary units. The corresponding longitudinal resistance is shown as a black dashed line with the scale on the right. Both, transmission and longitudinal resistance, were obtained at $T = 4.2$ K.

tance $R_{xx}$ (black curves) and radiation transmittance (gray curves) at helium temperature. All samples show an oscillating behavior of the photosignal at $T$ = 4.2 K which is reduced to a single peak when the temperature is increased to $T$ = 40 K. The latter corresponds to the cyclotron resonance position as identified by radiation transmission measurements. The CR positions $B_c$ are given in Tab. 11 as an average value of $|B_c|$ for right- and left-handed circularly polarized light.

### 6.1.2 Results for a Dirac Fermion System

Finally measurements were carried out for a Dirac fermion system. In Chapter 5 it was shown that the 6.6 nm HgTe QW sample has this special energy spectrum [14, 15]. Figure 27 (d) shows the magnetic field dependency of the photocurrent for the ungated 6.6 nm QW square sample #3. As above, the photosignal was measured for low and high temperature applying right-handed circularly polarized radiation with $\lambda$ = 118.8 $\mu$m: for $T$ = 4.2 K the photocurrent exhibits slight oscillations which reduce to a single peak when $T$ is increased. The THz radiation transmission is shown in gray and demonstrates a clear cyclotron resonance peak at a magnetic field value of $B$ = 1.2 T.

Depending on the carrier density of the QW structure the cyclotron resonance position $B_c$ shifts (see Chapter 5, compare Eq. (29)). This effect is typical for systems with a linear dispersion and is caused by the energy dependency of the effective cyclotron mass $m_c$ (Eq. (27)) and by the variation of Fermi energy (see Chapter 5).

In order to investigate the dependency on the carrier density in more detail additional measurements were performed on the gated 6.6 nm QW Hall bar sample #4. In this sample the carrier density $n$ could be exactly varied by the application of a gate voltage. For this purpose the photosignal $U_x$ was measured for two static positive magnetic field strengths $B$ = 1.5 and 2 T and for linearly polarized THz light with $\lambda$ = 118.8 $\mu$m. These measurements were performed in cooperation with Dimitry Kvon[1] and Vasily V. Bel'kov[2]. The

---

[1]Institute of Semiconductor Physics, Novosibirsk, Russia
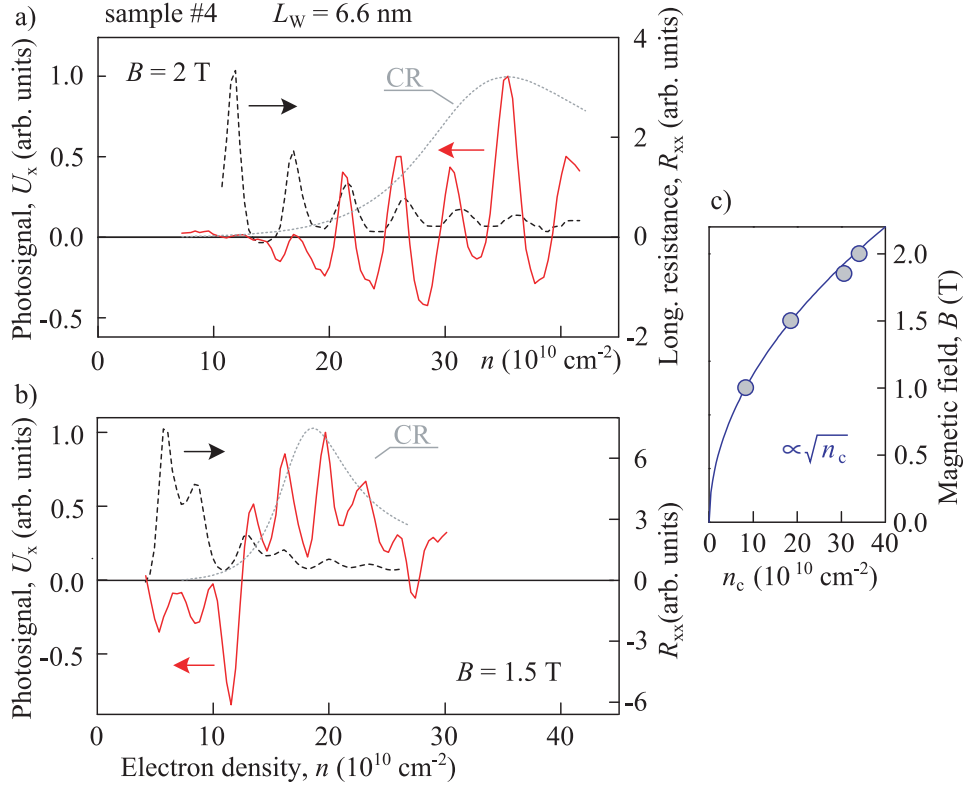[2]Ioffe Institute, St. Petersburg, Russia

**Figure 28:** Photosignal $U_x$ as a function of the carrier density $n$ varied by the gate voltage of the gated 6.6 nm QW Hall bar structure #4. The data were obtained at $T = 4.2$ K and with linear polarized radiation of $\lambda = 118.8$ $\mu$m. (a) and (b) depict the photosignal for two different magnetic fields of $B = 2$ and 1.5 T, respectively. The black dashed lines show the longitudinal resistance with SdH oscillations; the gray dotted lines depict the CR radiation absorption profile calculated according to Eq. (46). (c) shows the magnetic field value of the maximum photosignal as a function of the corresponding electron density showing a $B \propto \sqrt{n_c}$ dependency.

experimental results are shown in Fig. 28 as a function of the electron density $n$. The photosignal measurements were performed at helium temperature with THz radiation of 118.8 $\mu$m and were accompanied by measurements of the longitudinal resistance $R_{xx}$ (left and right scale, respectively). Besides the observed correlation between the oscillations of the photosignal with those of the longitudinal resistance $R_{xx}$ (showing SdH oscillations), the figure indicates a nonmonotonic behavior of the envelope function with a maximum at carrier

density $n_c = 19 \times 10^{10}$ cm$^{-2}$ for $B = 1.5$ T and $n_c = 34 \times 10^{10}$ cm$^{-2}$ for $B = 2$ T. The same measurements were done for magnetic fields $B = 0.5$ and 1.85 T with similar results (not shown). The dependency of $B$ on $n_c$ is shown in Fig. 28 (c) for all four static magnetic fields ($B = 1$, 1.5, 1.85 and 2 T). It demonstrates a proportionality of $B \propto \sqrt{n_c}$.

| sample | $L_W$ (nm) | $\bar{B}_c^{PGE}$ (T) | $\bar{B}_c^{TM}$ (T) |
|:------:|:----------:|:--------------------:|:--------------------:|
| #1 | 5 | 2.66 | 2.08 |
| #2* | 8 | - | - |
| #3 | 6.6 | 1.52 | 1.16 |
| #4 | 6.6 | - | - |
| #5 | 8 | 1.80 | 1.78 |
| #6 | 8 | 1.69 | 1.90 |
| #7 | 21 | 2.18/2.74 | 2.31/2.91 |

**Table 11:** Magnetic field positions $B_c$ of cyclotron resonance for the studied samples observed in transmission (4.2 K) and high temperature photocurrent (40 K) measurements. Listed are the average values of $|B_c|$ for both helicities. *The QW contains cadmium: $Hg_{0.86}Cd_{0.14}Te$.

## 6.2   Discussion

The experimental results for the photocurrent and photoresistance measurements of Section 6.1 show a nonmonotonic behavior superimposed by oscillations when an external magnetic field is applied. Moreover, for a 6.6 nm QW system with a Dirac-like dispersion this behavior could also be observed as a function of the carrier density. In this section a microscopic picture will be presented which allows to describe the origin of the THz radiation induced photocurrents. The model was evolved and calculated by the theoreticians Marina A. Semina[3], Mikhail M. Glazov[3] and Leonid E. Golub[3] and is based on the experimental results of this chapter. It is related to the magnetogyrotropic photogalvanic effect which was introduced and utilized in Chapters 2, 4 and 5.

---

[3]Ioffe Institute, St. Petersburg, Russia

Furthermore, it will be shown that the current can be decomposed into two parts which stem from the de Haas-van Alphen and the Shubnikov-de Haas effect, respectively. Finally the photoresistance will be addressed. As the derivation of the equations of this chapter is out of scope of this thesis only the main theoretical outcome of Ref. [20] will be introduced.

### 6.2.1  Microscopic Picture of Current Generation

When applying an external magnetic field perpendicular to the plane of a two dimensional electron gas, due to the Lorentz force the electrons are forced to move on orbits [39]. Assuming $\omega_c \tau \gg 1$ with cyclotron angular frequency $\omega_c$ and momentum scattering time $\tau$ these orbits can be considered to be closed with cyclotron radius $R_c = v/\omega_c$, where $v$ is the electron velocity [39]. This is depicted in Fig. 29 for spin-up and -down electrons. Note, that $x$ and $y$ are arbitrary chosen directions as there are no predefined directions of the currents due to the low symmetry of the system. Neglecting scattering processes the electrons move on the solid circles. When electron-phonon scattering is taken into account the electron energy decreases: the scattering process results in a displacement of the center of cyclotron orbit by $\Delta x$ and in a reduction of its radius from $R_c$ to $R_c'$ [82, 83]. Hence, the electrons move on the dashed or dotted circles in Fig. 29 depending on the scattering point shown in the figure for a positive and negative wavevector $k_y$. In gyrotropic media e.g., HgTe QW structures, this electron-phonon interaction is spin dependent and given by [20]

$$V_{k'k} = V_0 + V_{zy}\sigma_z(k_y + k_y').$$  (36)

Here, the first term on the right-hand side $V_0$ corresponds to the conventional spin independent scattering, $\boldsymbol{V}$ is a second rank pseudotensor, $\sigma_z$ is the Pauli matrix and $\boldsymbol{k}$ ($\boldsymbol{k}'$) is the initial (scattered) wavevector. Note, that this equation is a special case of Eq. (10). Considering a fixed spin e.g., spin-up in Fig. 29 (a), Eq. (36) results in unequal probabilities for scattering events for $k_y < 0$ and $k_y > 0$: while the probability is decreased in the first case, it is increased in the latter case. This results in an electron flux $j_{x,+}$ in positive $x$ direction of spin-up electrons. The situation for spin-down electrons is vice versa yielding a flux $j_{x,-}$ in negative $x$ direction. In the absence of Zeeman splitting these

fluxes are of equal strength and oppositely directed. Therefore, the net electric current is zero. However, the magnetic field induced Zeeman splitting results in an unequal population of spin-up and -down subband. Hence, $j_{x,+}$ and $j_{x,-}$ do not cancel each other out giving rise to a net *dc* current $j_x = j_{x,+} + j_{x,-}$.

The total expression for the *dc* current is given by [20]

$$j_x = \frac{e\beta\zeta}{|B|}|E_0|^2 \left[n_+\mu_+(\omega) - n_-\mu_-(\omega)\right], \tag{37}$$

with $\beta = 1$ for parabolic and $\beta = 1/2$ for linear dispersion. $|E_0|^2$ is the complex amplitude of the incident radiation, $n_\pm$ is the carrier density and $\mu_\pm$ the electron mobility for each spin branch. $\zeta$ stands for the strength of spin orbit interaction.

The oscillations of the photocurrent observed in experiments enter this picture as oscillations of carrier densities $n_\pm$ and mobilities $\mu_\pm$. Therefore, it is convenient to decompose Eq. (37) into two terms $j_n$ and $j_\mu$. The former one is
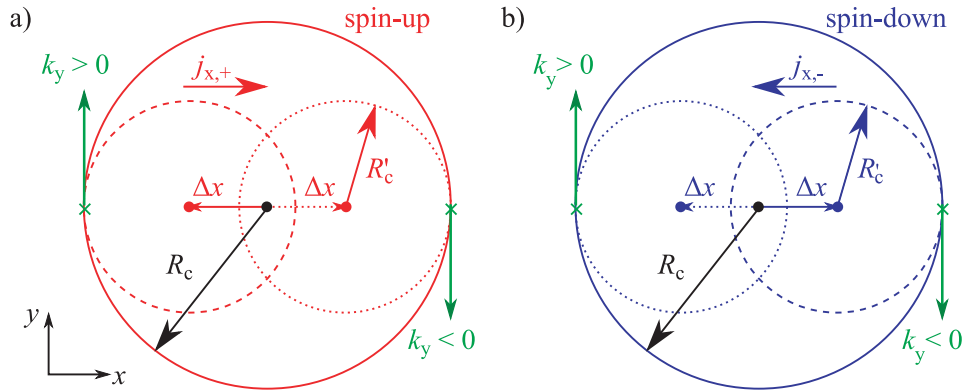


**Figure 29:** Cyclotron orbits of two dimensional (a) spin-up and (b) spin-down electrons in an external magnetic field. The solid circles with cyclotron radius $R_c$ correspond to the cyclotron orbit without electron-phonon scattering. Dashed and dotted circles with cyclotron radius $R'_c$ depict cyclotron orbits for electrons scattered by phonons for two possible scattering events: $k_y > 0$ and $k_y < 0$. Due to the reduction of $R_c$ by electron-phonon scattering the electrons shift in real space by $\Delta x = |R_c - R'_c|$, yielding two electron fluxes $j_{x,+}$ and $j_{x,-}$ for spin-up and -down. Note, that $x$ and $y$ are arbitrarily chosen directions.

related to the spin polarization $S_z = \frac{n_+ - n_-}{2(n_+ + n_-)}$ of the system, namely to the difference in spin-up and -down subband population. This is also known as zero bias spin separation [5]. The latter contribution originates from the difference of mobilities $\mu_+(\omega) - \mu_-(\omega)$. Hence, Eq. (37) can be rewritten as

$$j_x = j_n + j_\mu, \tag{38}$$

with

$$j_n = \frac{2e\beta\zeta}{|B|}|E_0|^2 S_z n\mu(\omega) \tag{39}$$

and

$$j_\mu = \frac{e\beta\zeta}{|B|}|E_0|^2 n \frac{\mu_+(\omega) - \mu_-(\omega)}{2}. \tag{40}$$

Herein, $n = n_+ + n_-$ and $\mu(\omega) = [\mu_+(\omega) + \mu_-(\omega)]/2$. In the following these two contributions will briefly be discussed.

The spin polarization $S_z$ determines $j_n$ the first contribution of Eq. (38). It is dependent on the density of states $\nu_0(E)$ and originates from the de Haas-van Alphen effect. Assuming $\hbar\omega_c \ll E_F$ and $E_F \gg \frac{\hbar}{\tau_q}$, with quantum scattering time $\tau_q$, the density of states can be expressed as [82, 84]

$$\nu_0(E) = \frac{m_c}{2\pi\hbar^2}\left[1 \pm 2\exp\left(\frac{-\pi}{\omega_c\tau_q}\right)\cos\left(2\pi\beta\frac{E}{\hbar\omega_c}\right)\right]. \tag{41}$$

Herein, $\pm$ stands for linear (+) and parabolic (-) dispersion. $\beta$ is defined as in Eq. (37). Equation (41) describes the density of states without taking into account the Zeeman splitting of bands. For spin splitted Landau Levels the density of states is given by $\nu_\pm(E) = \nu_0(E \mp \Delta E_Z/2)$ for each spin branch. This is sketched in Fig. 4 (b). In Eq. (41) the cosine factor represents the oscillatory parts and $\exp\left(\frac{-\pi}{\omega_c\tau_q}\right)$ determines the amplitude of oscillations. Equation (41) only considers oscillating contributions of the first order term in the small parameter $\exp\left(\frac{-\pi}{\omega_c\tau_q}\right)$ - higher order terms are neglected.

The spin polarization $S_Z$ [85] can be written in terms of Eq. (41) as

$$S_Z = -\frac{1}{4\beta E_F}\left[\Delta E_Z \pm \right.$$
$$\left. \frac{2\hbar\omega_c}{\pi}\mathcal{T}_1\exp\left(\frac{-\pi}{\omega_c\tau_q}\right)\sin\left(\frac{\pi\Delta E_Z}{\hbar\omega_c}\right)\cos\left(\frac{2\pi\beta E_F}{\hbar\omega_c}\right)\right], \tag{42}$$

with $\pm$ for linear (+) and parabolic (-) dispersion. Here again the cosine factor represents the oscillatory part and $\exp\left(\frac{-\pi}{\omega_c\tau_q}\right)$ the amplitude of oscillations. The sine factor takes into account the relative positions of the Zeeman split Landau levels and the factor $\mathcal{T}_1$ considers the smearing of the carrier distribution function at nonzero temperatures by [86]

$$\mathcal{T}_1 = \frac{2\pi^2 k_B T_e}{\hbar\omega_c \sinh\left(2\pi^2 k_B T_e/\hbar\omega_c\right)}, \tag{43}$$

where $T_e$ is the electron gas temperature.

The second term $j_\mu$ of Eq. (38) is defined by the difference in carrier mobilities of the spin branches and is related to the Shubnikov-de Haas effect. In line with Refs. [87,88] the mobility for frequency $\omega$ in the vicinity of $\omega_c$ is given by

$$\mu_\pm(\omega) = \frac{|e|\tau/2m_c}{1+(\omega-\omega_c)^2\tau^2} \times \left[1\pm\right.$$
$$\left.\mathcal{T}_1 \exp\left(\frac{-\pi}{\omega_c\tau_q}\right)\cos\left(\frac{2\pi\beta E_\pm}{\hbar\omega_c}\right)f_1(\omega\tau,\omega_c\tau)\right], \tag{44}$$

where $E_\pm = E_F \mp \Delta E_Z/2$ is the Fermi energy in each spin subband, $\pm$ stands for linear (-) and parabolic (+) dispersion and $f_1$ is a smooth function of $\omega\tau$ and $\omega_c\tau$. The factor $\mathcal{T}_1$ and $\beta$ are the same as above (see Eqs. (43) and (37)).

Equation (44) contains both the classical cyclotron resonance part, which is proportional to $\frac{\tau}{1+(\omega-\omega_c)^2\tau^2}$, as well as the oscillating part, which originates from the consecutive crossing of Fermi energy and Landau levels (see Section 2.5).

### 6.2.2  Analysis of the Photocurrents

The theoretical equations of Section 6.2.1 allow a comparison of calculated photocurrents with measured ones presented in Section 6.1. In order to analyze the oscillations of the photocurrent the individual contributions $j_n$ and $j_\mu$ are calculated using Eqs. (39) and (40) with oscillatory parts according to Eqs. (42) and (44). For this the parameters are chosen close to those determined in the experiments. In the following three samples will be analyzed which are typical for normal parabolic, inverted parabolic and linear dispersion: the 8 nm HgCdTe QW Hall bar sample #2, the 8 nm HgTe QW square sample #5 and the 6.6 nm HgTe QW Hall bar sample #4.
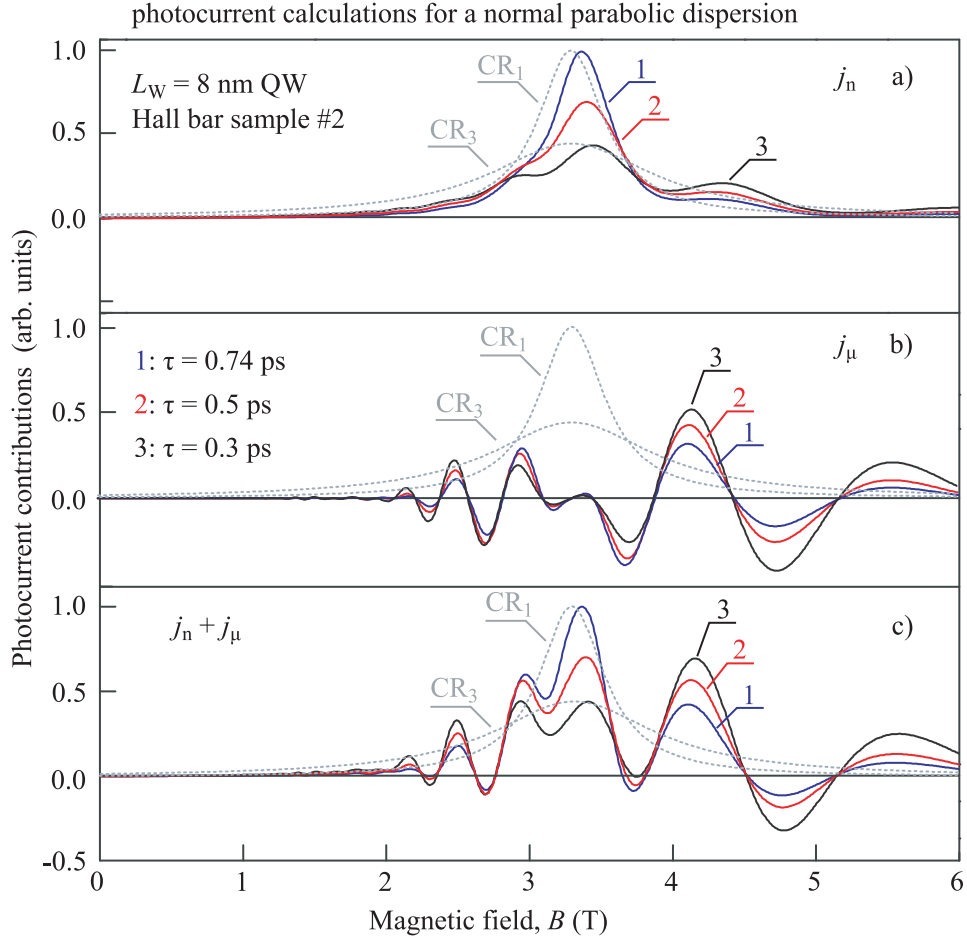
photocurrent calculations for a normal parabolic dispersion



**Figure 30:** Panel (a) and (b) depict the individual contributions $j_n$ and $j_\mu$ of the total photocurrent which is presented in (c). The parameters are chosen close to those of the 8 nm HgCdTe QW Hall bar sample #2, see Fig. 24: $m/m_0 = 0.034$, $n = 75 \times 10^{10}$ cm$^{-2}$, $g$ = -36.5 and $\tau_q$ = 0.13 ps. Curves 1, 2 and 3 are calculated for $\tau$ = 0.74, 0.5 and 0.3 ps, respectively. Gray dotted curves correspond to the CR absorption profile calculated according to Eq. (45).

*Calculations for a Parabolic Dispersion*   Figure 30 (a) and (b) show the two calculated photocurrent contributions $j_n$ and $j_\mu$ for the 8 nm QW Hall bar sample #2 with a normal parabolic band structure. The total photocurrent $j = j_n + j_\mu$ is presented in (c). Curves 1, 2 and 3 correspond to different transport scattering times $\tau$, namely 0.74, 0.5 and 0.3 ps, respectively. Note,

that all curves are given in arbitrary units and are normalized in the same way. The gray lines depict the corresponding cyclotron resonance absorption profiles calculated according to

$$\mathcal{CR} \propto \frac{\tau}{1 + (\omega - \omega_c)^2 \tau^2}. \tag{45}$$

It is also given in arbitrary units.

Panel (a) and (b) demonstrate that the two contributions $j_n$ and $j_\mu$ have a significantly different behavior on the magnetic field, which makes it possible to distinguish between the two contributing terms: $j_n$ mainly follows the smooth CR absorption profile with a distinct maximum almost at CR position $B_c$ (see Fig. 30 (a)). Outside the resonance position it decreases strongly, demonstrating only marginal oscillations. This is in agreement with Eqs. (32) and (33) of Chapter 5. By contrast, $j_\mu$ strongly oscillates with several changes of sign. These can even be observed for magnetic fields larger than $B_c$. Furthermore, $j_\mu$ vanishes at the CR position (see Fig. 30 (b)).

A comparison of the total photocurrent (see Fig. 30 (c)) with the measured photosignal (see in Fig. 24 (a)) shows that the main features are reproduced. Both figures show pronounced oscillations with sign inversions of the current ($j_\mu$). The oscillations are enhanced in the range of cyclotron resonance ($j_n$), but are also observable for $B > B_c$ ($j_\mu$). Thus, both terms contribute to the total current, although $j_\mu$ seems to dominate.

The same calculations were performed with adjusted parameters for the 8 nm HgTe QW square sample #5, which has an inverted parabolic band structure. The results for $j_n$ and $j_\mu$ are presented in Fig. 31. Herein, $j_n$ also has a maximum near $B_c$ and decreases rapidly outside the vicinity of CR. The calculations reveal no oscillations for $j_n$. On the other hand $j_\mu$ is zero at CR position and exhibits oscillations in the range of the CR absorption profile.

A comparison of Fig. 31 for $j_n$ and $j_\mu$ with the experimental findings depicted in Fig. 25 (a) clearly shows that both terms contribute: the measured signal shows pronounced oscillations with sign inversions ($j_\mu$) as well as an enhancement in the vicinity of CR ($j_n$).

When the temperature is increased the oscillatory contributions of Eqs. (42) and (44) are suppressed. This is due to the drastic dependency of $\mathcal{T}_1$ on the
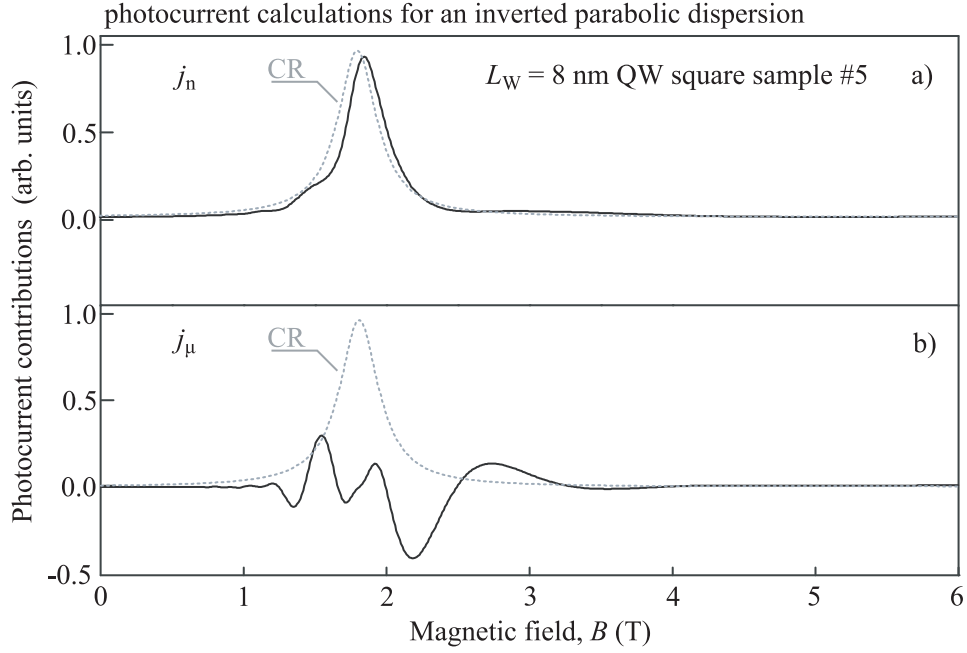
**Figure 31:** Panel (a) and (b) depict the individual contributions $j_n$ and $j_\mu$ of the total photocurrent. The parameters are chosen close to those of the 8 nm HgTe QW square sample #5, see Fig. 25: $m/m_0 = 0.02$, $n = 24$ $\times 10^{10}$ cm$^{-2}$, $g = $ -41.5 and $\tau = 0.68$ ps, $\tau_q = 0.13$ ps. Gray dotted curves correspond to the CR absorption profile calculated according to Eq. (45).

effective temperature $T_e$: when $T_e$ is increased $\mathcal{T}_1$ decreases exponentially by the sinh($T_e$) term in the denominator. Hence, only the smooth part of $j_n$ contributes to the total current for high temperatures. This is nicely observed in the experiment (see Fig. 25 (c)).

It should be noted that the total calculated current $j = j_n + j_\mu$ did not take into account other current generation mechanism e.g., the spin dependent excitation mechanism [5]. Neither are higher order terms of the small parameter $\exp\left(\frac{-\pi}{\omega_c \tau_q}\right)$ considered even though the Shubnikov-de Haas oscillations of $R_{xx}$ in Figs. 24 and 25 clearly reveal traces of the second harmonic. Hence, for a more detailed comparison of theory and experiment these additional mechanism and higher order terms have to be included in the theoretical description.
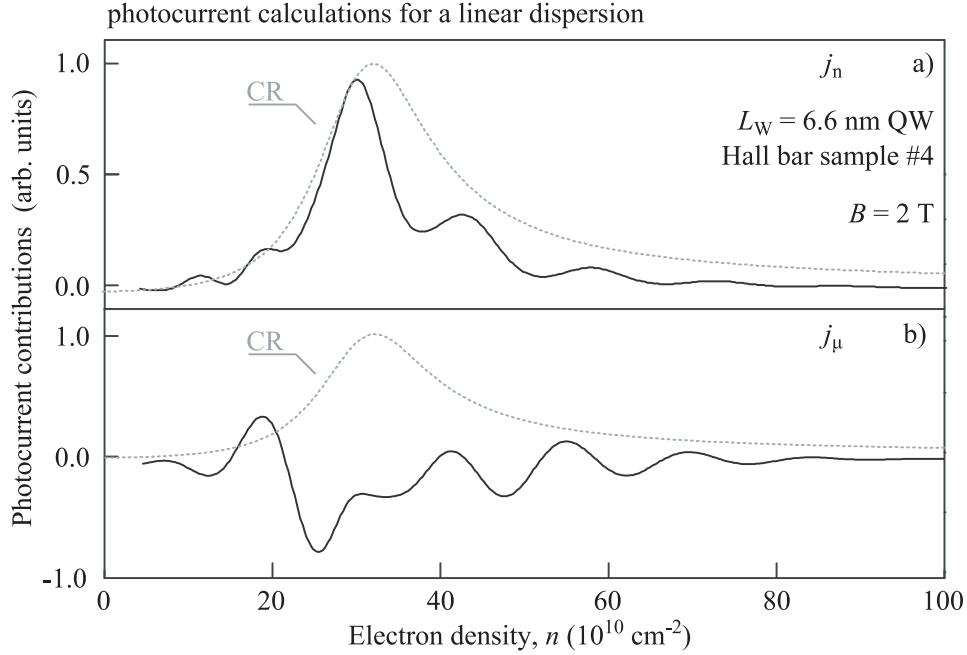
photocurrent calculations for a linear dispersion

**Figure 32:** Panel (a) and (b) depict the individual contributions $j_n$ and $j_\mu$ of the total photocurrent as a function of the carrier density $n$, varied by a gate voltage. The parameters are related to those of the studied 6.6 nm QW Hall bar structure #4: $v_{DF} = 7.6 \times 10^5$ m/s (close to the value obtained experimentally in Chapter 5), $\tau = 0.8$ ps and $\tau_q = 0.41$ ps for $n = 10 \times 10^{10}$ cm$^{-2}$. Gray dotted curves correspond to the CR absorption profile calculated with Eq. (46).

*Calculations for a Dirac Fermion System*    A distinguishing feature of CR assisted photocurrents in structures with a linear energy spectrum compared to a parabolic one is that CR related effects can also be detected upon carrier density variation. This has its origin in the dependency of the cyclotron frequency on the Fermi energy $E_F$ (compare Section 5.3). It can be included into the calculations of $j_n$ and $j_\mu$ by considering the carrier density dependency of the conductivity $\sigma(\omega)$, given by [20]

$$\sigma(\omega) = \frac{e^2 n^* \tau^*}{2 m_c^* \left[ 1 + \left( \omega - \omega_c^* \sqrt{n^*/n} \right)^2 \tau^{*2} n^*/n \right]} \tag{46}$$

which is valid in the vicinity of cyclotron resonance. Herein, the parameters $\omega_c^*$, $m_c^*$, and $\tau^*$ are the corresponding values for a certain carrier density $n^*$.

Figure 32 depicts the theoretical calculations of the photocurrent contributions for a Dirac-like dispersion as a function of the carrier density $n$. The used parameters are similar to those of the 6.6 nm QW Hall bar sample #4 for a magnetic field $B = 2$ T. The calculated contribution $j_n$ in panel (a) shows a distinct maximum almost at CR position and gentle oscillations. The second contribution $j_\mu$ in panel (b) shows a more pronounced oscillating behavior than $j_n$ with a smooth enhancement, mainly for negative currents, close to the position of CR. When calculating the two current contributions for a static magnetic field of 1.5 T the position of the distinct maximum of $j_n$ shifts to smaller carrier densities (not shown). For $j_\mu$ the enhancement of the oscillations is shifted to smaller carrier densities, too.

This dependency is also observed in the experiments as shown in Fig. 28. For the measured curve at $B = 2$ T the maximum photosignal is detected for a carrier density of $n_c = 34 \times 10^{10}$ cm$^{-2}$. For 1.5 T the maximum position shifts to $n_c = 19 \times 10^{10}$ cm$^{-2}$. Figure 28 (c) shows the relationship $B(n_c)$ for all applied magnetic fields $B$. The data show a $B \propto \sqrt{n_c}$ dependency, which is in agreement with Eq. (29) for systems with a linear dispersion. Moreover, Fig. 28 (a) and (b) shows that the measured photosignals can nicely be enveloped by the calculated CR absorption profiles (gray lines, calculated by using Eq. (46)).

### 6.2.3   Analysis of the Photoresistance

Finally the oscillations in the photoresistance will be addressed, which are related to the Shubnikov-de Haas effect. Its microscopic origin can be found in the electron gas heating due to the absorption of THz radiation which causes a change of the electron mobility (compare Section 2.3). The electron gas can be described by an effective temperature $T_e$. At cyclotron resonance conditions the resonant absorption leads to a heating of the electron gas and to an increase of $T_e$ according to

$$T_e = T_0 + \frac{a}{1 + (\omega - \omega_c)^2 \tau^2}, \tag{47}$$

where $a$ is proportional to the radiation intensity and $T_0$ is the lattice temperature. The longitudinal resistance of QWs with a parabolic energy spectrum

is given by the standard expression [86]

$$R_{xx} \propto 2\mathcal{T}_1 \exp\left(-\frac{\pi}{\omega_c \tau_q}\right) \cos(2\pi \frac{E_F}{\hbar \omega_c}) \cos(\pi \frac{E_Z}{\hbar \omega_c}) +$$
$$\mathcal{T}_2 \exp\left(-\frac{2\pi}{\omega_c \tau_q}\right) \cos(4\pi \frac{E_F}{\hbar \omega_c}) \cos(2\pi \frac{E_Z}{\hbar \omega_c}). \tag{48}$$

Herein, the first and second term on the right-hand side correspond to the first and second order term in the small parameter $\exp\left(\frac{-\pi}{\omega_c \tau_q}\right)$. $\mathcal{T}_l$ with $l = 1, 2$ is given by

$$\mathcal{T}_l = \frac{2l\pi^2 k_B T_e}{\hbar \omega_c \sinh\left(2l\pi^2 k_B T_e / \hbar \omega_c\right)}. \tag{49}$$

and takes into account the effective temperature $T_e$ of the electron gas. Hence, the Shubnikov-de Haas oscillations smear out when the electron gas is heated as $\mathcal{T}_l$ exponentially decreases with increasing $T_e$.

Figure 33 (a) shows the calculated longitudinal resistance $R_{xx}$ according to Eq. (48) for the 8 nm HgTe QW square sample #5. Three different effective temperatures $T_e$ were considered. The suppression of the SdH oscillations can nicely be seen in the vicinity of CR position: the oscillations for the lowest effective temperature $T_{e,3}$ have the largest amplitude; these amplitudes get notably smaller for higher temperatures $T_{e,2}$ and $T_{e,1}$.

Figure 33 (b) shows the calculated photoresistance $\Delta R_x$ according to $\Delta R_x = R_{xx}(T_e) - R_{xx}(T_0)$ i.e., the difference of the resistance $R_{xx}(T_{e,i})$ for higher effective temperatures ($i = 1, 2, 3$) and the *dark* resistance $R_{xx}(T_0)$ (curve not shown). $\Delta R_x$ shows pronounced oscillations in the vicinity of CR position with multiple sign inversions.

The corresponding experimental result for the photoresistance $\Delta R_x$ is presented in Figure 26 (a). The comparison shows that the main experimental features are well described by the presented model: both show pronounced oscillations with multiple sign inversions and an enhancement of the signal near the CR position.

For high temperatures the oscillations in the photoresistance vanish completely. This is caused by the strong dependency of $\mathcal{T}_l$ on the temperature: when $T_e$ is increased, $\mathcal{T}_l$ decreases drastically as the denominator contains a $\sinh(T_e)$
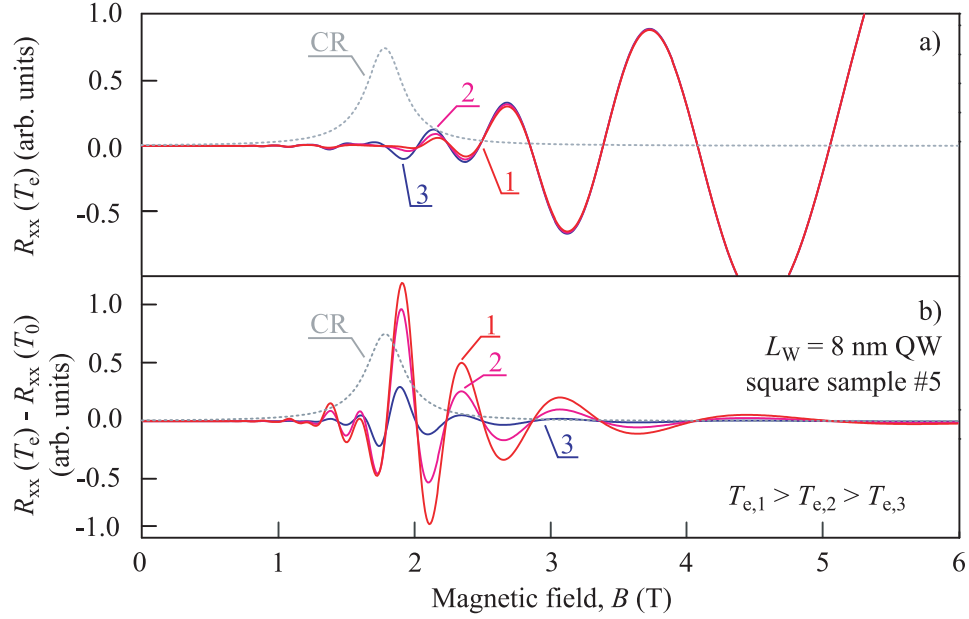
**Figure 33:** (a) Calculated longitudinal resistance $R_{xx}$ for three different effective electron gas temperatures $T_e$ according to Eqs. (47) - (49). Parameters are chosen close to the values of the 8 nm HgTe QW square sample #5: $m/m_0 = 0.026$, $n = 25 \times 10^{10}$ cm$^{-2}$, $g$ = -41.5, $\tau = 0.86$ ps and $\tau_q = 0.16$ ps. (b) Photoresistance $\Delta R_x$, described as the difference of the *dark* longitudinal resistance $R_{xx}(T_0)$ and the $R_{xx}(T_e)$ curves shown in panel (a). Gray curves correspond to the CR absorption profile calculated according to Eq. (45).

term. Therefore, at high temperatures the photoresistance is only caused by the electron gas heating due to cyclotron resonance. This can be seen nicely in Fig. 25 (c) for $T = 40$ K, where the photoresistance just follows the Lorentzian shape of CR absorption.

## 6.3   Brief Summary

In this chapter it was shown that THz radiation under cyclotron resonance conditions can result in quantum oscillations of the photocurrent and the photoresistance at low temperatures. The oscillations were observed as a function of an external applied magnetic field for all three types of dispersions all re-

alized in HgTe QWs: normal and inverted parabolic, as well as linear. A microscopic model was developed which explains the photocurrent generation. It is based on the spin dependent asymmetric electron-phonon scattering. According to the model the current can be decomposed into two contributions. One is caused by the magnetic field induced electron spin polarization $S_z$, analog to the de Haas-van Alphen effect, the second one originates from the difference of the electron mobilities $\mu(\omega)$ in the spin subbands in the presence of a magnetic field. The latter one is related to the Shubnikov-de Haas effect. Both contain oscillatory parts contributing to the total photocurrent and describe all experimental observations well.

# 7 Conclusion

The research carried out in the framework of this thesis clearly demonstrates that in mercury telluride quantum well structures terahertz radiation induced photocurrents can be observed and that they are well suited for the characterization of such systems. These currents are of large amplitude and exhibit different characteristics, comprising oscillations and a strong enhancement if an external magnetic field is applied. It is shown that the currents originate from spin dependent phenomena: the terahertz radiation heats the two dimensional electron (hole) gas of the semiconductor structures. The relaxation of the free carriers is spin dependent and results in an asymmetry of carriers in momentum space, which yields pure spin currents. Due to the application of an external magnetic field, these spin currents can be converted into a net electric current. When the magnetic field is applied perpendicular to the plane of the two dimensional electron (hole) gas, the currents show a strong increase. It is demonstrated that this increase is not solely an enhancement due to resonant absorption of terahertz radiation when the condition for cyclotron resonance is fulfilled, but also due to material properties like strong spin orbit interaction and large Landé factor.

Another important result is that the terahertz radiation induced photocurrents are not only observed for systems with a parabolic energy spectrum, but also for those with a linear Dirac-like one. Herein, the currents show an unique behavior: the effect of cyclotron resonance can be detected upon variation of the carrier density; a phenomenon which is not observable for systems with a parabolic dispersion. This is attributed to the special Landau level splitting in these types of systems. In contrast to conventional semiconductors the Landau level splitting of a system with linear dispersion is not equidistant. As a consequence, the position where the cyclotron resonance condition is fulfilled shows a square root dependency on the carrier density. Hence, the cyclotron resonance assisted currents can be utilized to probe the energy spectrum of two dimensional Dirac fermions. Moreover, as the currents originate from spin dependent effects, they give an access to the electronic and spin properties of these systems e.g., spin polarized electron transport.

All this demonstrates that cyclotron resonance assisted photocurrents are a suitable method for the investigation of topological insulator systems. Therefore, it might be possible to use these currents to distinguish between the Dirac and the insulating states of such systems.

The resonance positions of the mercury telluride quantum well structures of critical width are observed at rather small magnetic fields. This is a consequence of the extraordinary small cyclotron masses of the Dirac fermion system. Hence, these mercury telluride quantum well structures are a promising candidate for the application of frequency selective cyclotron resonance assisted detectors operating in the terahertz range [89].

In structures with high carrier mobility and at low temperatures the photocurrent exhibits magnetic field induced oscillations. Their analysis shows that the current can be decomposed into two contributions: one stems from the periodic change of the carriers' mobility when the magnetic field is varied, the second one results from the oscillations of the total spin polarization of the system. They originate from the consecutive crossing of the Fermi energy with Landau levels when the magnetic field is swept. They are related to the effects of Shubnikov-de Haas and de Haas-van Alphen. An interesting feature of the two current contributions is their behavior at cyclotron resonance position: whereas the first contribution (the Shubnikov-de Haas related one) vanishes at the position of cyclotron resonance, the second one (de Haas-van Alphen) is enhanced.

Last, but not least, the experiments on diluted magnetic semiconductor structures demonstrate the main properties of the magnetogyrotropic photogalvanic effect and provide a solid basis for the analysis of the data observed in the mercury telluride quantum well nanostructures.

# References

[1] M. Dyakonov, ed., *Spin Physics in Semiconductors*. Springer-Verlag, Berlin, 2008.

[2] W. Chen and I. Buyanova, eds., *Handbook of Spintronic Semiconductors*. Pan Stanford Publishing Pte. Ltd., Singapore, 2010.

[3] T. Dietl, D.D. Awschalom, M. Kaminska, and H. Ohno, eds., *Spintronics*. Semiconductors and Semimetals. Academic Press, Amsterdam, 2008.

[4] E.I. Rashba and A.L. Efros, *Efficient electron spin manipulation in a quantum well by an in-plane electric field*, Appl. Phys. Lett. **83**, 5295 (2003).

[5] S.D. Ganichev, V.V. Bel'kov, S.A. Tarasenko, S.N. Danilov, S. Giglberger, Ch. Hoffmann, E.L. Ivchenko, D. Weiss, W. Wegscheider, Ch. Gerl, D. Schuh, J. Stahl, J. De Boeck, G. Borghs, and W. Prettl, *Zero-bias spin separation*, Nature Phys. **2**, 609 (2006).

[6] R. Winkler, *Spin-Orbit Coupling Effects in Two-Deimensional Electron and Hole Systems*. Springer-Verlag, Berlin, 2003.

[7] J.E. Moore, *The birth of topological insulators*, Nature **464**, 194 (2010).

[8] L. Fu, C.L. Kane, and E.J. Mele, *Topological Insulators in Three Dimensions*, Phys. Rev. Lett. **98**, 106803 (2007).

[9] D. Hsieh, Y. Xia, D. Qian, L. Wray, J.H. Dil, F. Meier, J. Osterwalder, L. Patthey, J.G. Checkelsky, N.P. Ong, A.V. Fedorov, H. Lin, A. Bansil, D. Grauer, Y.S. Hor, R.J. Cava, and M.Z. Hasan, *A tunable topological insulator in the spin helical Dirac transport regime*, Nature Lett. **460**, 1101 (2009).

[10] M.Z. Hasan and C.L. Kane, *Colloquium: Topological insulators*, Rev. Mod. Phys. **82**, 3045 (2010).

[11] B.A. Bernevig, T.L. Hughes, and S.C. Zhang, *Quantum Spin Hall Effect and Topological Phase Transition in HgTe Quantum Wells*, Science **314**, 1757 (2006).

[12] M. König, S. Wiedmann, C. Brüne, A. Roth, H. Buhmann, L.W. Molenkamp, X.L. Qi, and S.C. Zhang, *Quantum Spin Hall Insulator State in HgTe Quantum Wells*, Science **318**, 766 (2007).

[13] B. Büttner, C.X. Liu, G. Tkachov, E.G. Novik, C. Brüne, H. Buhmann, E.M. Hankiewicz, P. Recher, B. Trauzettel, S.C. Zhang, and L.W. Molenkamp, *Single valley Dirac fermions in zero-gap HgTe quantum wells*, Nature Phys. **7**, 418 (2011).

[14] Z.D. Kvon, S.N. Danilov, D.A. Kozlov, C. Zoth, N.N. Mikhailov, S.A. Dvoretsky, and S.D. Ganichev, *Cyclotron Resonance of Dirac Fermions in HgTe Quantum Wells*, JETP Lett. **94**, 816 (2011).

[15] P. Olbrich, C. Zoth, P. Vierling, K.-M. Dantscher, G.V. Budkin, S.A. Tarasenko, V.V. Bel'kov, D.A. Kozlov, Z.D. Kvon, N.N. Mikhailov, S.A. Dvoretsky, and S.D. Ganichev, *Giant photocurrents in a Dirac fermion system at cyclotron resonance*, Phys. Rev. B **87**, 235439 (2013).

[16] Z.D. Kvon, K.-M. Dantscher, C. Zoth, D.A. Kozlov, N.N. Mikhailov, S.A. Dvoretsky, and S.D. Ganichev, *Terahertz Electron Transport in a Two-Dimensional Topological Insulator in a HgTe Quantum Well*, JETP Lett. **99**, 290 (2014).

[17] S.D. Ganichev and W. Prettl, *Intense Terahertz Excitation of Semiconductors.* Oxford Univ. Press, 2006.

[18] J.K. Furdyna, *Diluted magnetic semiconductors*, J. Appl. Phys. **64**, R29 (1988).

[19] P. Olbrich, C. Zoth, P. Lutz, C. Drexler, V.V. Bel'kov, Ya.V. Terent'ev, S.A. Tarasenko, A.N. Semenov, S.V. Ivanov, D.R. Yakovlev, T. Wojtowicz, U. Wurstbauer, D. Schuh, and S.D. Ganichev, *Spin-polarized electric currents in diluted magnetic semiconductor*

*heterostructures induced by terahertz and microwave radiation*, Phys. Rev. B **86**, 085310 (2012).

[20] C. Zoth, P. Olbrich, P. Vierlng, K.-M. Dantscher, V.V. Bel'kov, M.A. Semina, M.M. Glazov, L.E. Golub, D.A. Kozlov, Z.D. Kvon, N.N. Mikhailov, S.A. Dvoretsky, and S.D. Ganichev, *Quantum Oscillations of Photocurrents in HgTe Quantum Wells with Dirac and Parabolic Dispersions*, arxiv Cond. Mat. 1407.1162v2 (2014).

[21] A.F. Holleman and N. Wiberg, *Lehrbuch der Anorganischen Chemie.* Walter de Gruyter, Berlin, 1995.

[22] J.-W. Luo and A. Zunger, *Design Principles and Coupling Mechanisms in the 2D Quantum Well Topological Insulator HgTe/CdTe*, Phys. Rev. Lett. **105**, 176805 (2010).

[23] X.-L. Qi, S.C. Zhang, and X.L. Qi, *Topological insulators and superconductors*, Rev. Mod. Phys. **83**, 1057 (2011).

[24] B. Wittmann, S.N. Danilov, V.V. Bel'kov, S.A. Tarasenko, E.G. Novik, H. Buhmann, C. Brüne, L.W. Molenkamp, Z.D. Kvon, N.N. Mikhailov, S.A. Dvoretsky, N.Q. Vinh, A.F.G. van der Meer, B. Murdin, and S.D. Ganichev, *Circular photogalvanic effect in HgTe/CdHgTe quantum well structures*, Semicond. Sci. Technol. **25**, 095005 (2010).

[25] M. Orlita, D.M. Basko, M.S. Zholudev, F. Teppe, W. Knap, V.I. Gavrilenko, N.N. Mikhailov, S.A. Dvoretskii, P. Neugebauer, C. Faugeras, A.-L. Barra, G. Martinez, and M. Potemski, *Observation of three-dimensional massless Kane fermions in a zinc-blende crystal*, Nature Phys. **10**, 233 (2014).

[26] A.V. Ikonnikov, A.A. Lastovkin, K.E. Spirin, M.S. Zholudev, V.V. Rumyantsev, K.V. Maremyanin, A.V. Antonov, V.Ya. Aleshkin, V.I. Gavrilenko, S.A. Dvoretskii, N.N. Mikhailov, Yu.G. Sadofyevc, and N. Samalc, *Terahertz Spectroscopy of Quantum-Well Narrow-Bandgap HgTe/CdTe-Based Heterostructures*, JETP Lett. **92**, 756 (2010).

[27] M.M. Glazov and S.D. Ganichev, *High frequency electric field induced nonlinear effects in graphene*, Physics Reports **535**, 101 (2014).

[28] V.V. Bel'kov, S.D. Ganichev, E.L. Ivchenko, S.A. Tarasenko, W. Weber, S. Giglberger, M. Olteanu, H.-P. Tranitz, S.N. Danilov, P. Schneider, W. Wegscheider, D. Weiss, and W. Prettl, *Magneto-gyrotropic photogalvanic effects in semiconductor quantum wells*, J. Phys.: Condens. Matter **17**, 3405 (2005).

[29] V.V. Bel'kov and S.D. Ganichev, *Magneto-gyrotropic effects in semiconductor quantum wells*, Semicond. Sci. Technol. **23**, 114003 (2008).

[30] E.L. Ivchenko and S.D. Ganichev, *Spin Photogalvanics*, in *Spin Physics in Semiconductors*, M.I. Dyakonov, ed. Springer-Verlag, Wien, 2008.

[31] S.D. Ganichev and W. Prettl, *Spin photocurrents in quantum wells*, J. Phys.: Condens. Matter **15**, R935 (2003).

[32] S.D. Ganichev and L.E. Golub, *Interplay of Rashba/Dresselhaus spin splittings probed by photogalvanic spectroscopy - A review*, Phys. Status Solidi B (2014). doi: 10.1002/pssb.201350261.

[33] N.S. Averkiev, L.E. Golub, and M. Willander, *Spin relaxation anisotropy in two-dimensional semiconductor systems*, J. Phys.: Condens. Matter **14**, R271 (2002).

[34] S. Giglberger, L.E. Golub, V.V. Bel'kov, S.N. Danilov, D. Schuh, Ch. Gerl, F. Rohlfing, J. Stahl, W. Wegscheider, D. Weiss, W. Prettl, and S.D. Ganichev, *Rashba and Dresselhaus Spin-Splittings in Semiconductor Quantum Wells Measured by Spin Photocurrents*, Phys. Rev. B **75**, 035327 (2007).

[35] K. Seeger, *Semiconductor Physics*. Springer-Verlag, Wien, 1973.

[36] J. Kono, *Cyclotron Resonance*, in *Methods in Materials Research*, E.N. Kaufmann, ed. John Wiley & Sons, Inc., New York, 2001.

[37] T. Numai, *Fundamentals of Semiconductor Lasers.* Springer-Verlag, New York, 2004.

[38] H. Ibach and H. Lüth, *Festkörperphysik.* Springer-Verlag, Berlin, 2002.

[39] J.H. Davies, *The Physics of Low-Dimensional Semiconductors.* Cambridge University Press, Cambridge, 1998.

[40] T. Ihn, *Semiconductor Nanostructures.* Oxford University Press, Oxford, 2010.

[41] C. Kittel, *Einführung in die Festkörperphysik.* Oldenburg Verlag, München, 1973.

[42] P. Olbrich, *THz radiation induced spin polarized currents in low dimensional semiconductor structures.* PhD thesis, University of Regensburg, 2010.

[43] F.K. Kneubühl and M.W. Sigrist, *Laser.* Teubner, Leipzig, 1999.

[44] Z.D. Kvon, E.B. Olshanetsky, N.N. Mikhailov, and D.A. Kozlov, *Two-dimensional electron systems in HgTe quantum wells*, Low Temp. Phys. **35**, 6 (2009).

[45] A.V. Ikonnikov, M.S. Zholudev, K.V. Marem'yanin, K.E. Spirin, A.A. Lastovkin, V.I. Gavrilenko, S.A. Dvoretskii, and N.N. Mikhailov, *Cyclotron Resonance in HgTe/CdTe(013) Narrowband Heterostructures in Quantized Magnetic Fields*, JETP Lett. **95**, 406 (2012).

[46] X.-L. Qi and S.C. Zhang, *Topological insulators and superconductors*, Rev. Mod. Phys. **83**, 1057 (2011).

[47] M.K. Kneip, D.R. Yakovlev, M. Bayer, G. Karczewski, T. Wojtowicz, and J. Kossut, *Engineering of spin-lattice relaxation dynamics by digital growth of diluted magnetic semiconductor CdMnTe*, Appl. Phys. Lett. **88**, 152105 (2006).

[48] S.A. Crooker, D.A. Tulchinsky, J. Levy, D.D. Awschalom, R. Garcia, and N. Samarth, *Enhanced Spin Interactions in Digital Magnetic Heterostructures*, Phys. Rev. Lett. **75**, 505 (1995).

[49] J. Jaroszyński, T. Andrearczyk, G. Karczewski, J. Wróbel, T. Wojtowicz, E. Papis, E. Kamińska, A. Piotrowska, D. Popović, and T. Dietl, *Ising Quantum Hall Ferromagnet in Magnetically Doped Quantum Wells*, Phys. Rev. Lett. **89**, 266802 (2002).

[50] U. Wurstbauer, C. Śliwa, D. Weiss, T. Dietl, and W. Wegscheider, *Hysteretic magnetoresistance and thermal bistability in a magnetic two-dimensional hole system*, Nature Phys. **6**, 955 (2010).

[51] U. Wurstbauer, M. Sodaand R. Jakiela, D. Schuh, D. Weiss, J. Zweck, and W. Wegscheider, *Coexistence of ferromagnetism and quantum Hall effect in Mn modulation-doped two-dimensional hole systems*, J. Cryst. Growth **311**, 2160 (2009).

[52] U. Wurstbauer, S. Knott, A. Zolotaryov, D. Schuh, W. Hansen, and W. Wegscheider, *Strong localization effect in magnetic two-dimensional hole systems*, Appl. Phys. Rev. **96**, 022103 (2010).

[53] T. Dietl, *(Diluted) Magnetic Semiconductors*, in *Handbook on Semiconductors*, T.S. Moss, ed. North-Holland, Amsterdam, 1994.

[54] A.V. Ikonnikov, M.S. Zholudev, K.E. Spirin, A.A. Lastovkin, K.V. Maremyanin, V.Ya. Aleshkin, V.I. Gavrilenko, O. Drachenko, M. Helm, J. Wosnitza, M. Goiran, N.N. Mikhailov, S.A. Dvoretski, F. Teppe, N. Diakonova, C. Consejo, B. Chenaud, and W. Knap, *Cyclotron resonance and interband optical transitions in HgTe/CdTe (013) quantum well heterostructures*, Semicond. Sci. Technol. **26**, 125011 (2011).

[55] M.S. Zholudev, A.V. Ikonnikov, F. Teppe, M. Orlita, K.V. Maremyanin, K.E. Spirin, V.I. Gavrilenko, W. Knap, S.A. Dvoretskiy, and N.N. Mihailov, *Cyclotron resonance in HgTe/CdTe/HgCdTe heterostructures in high magnetic fields*, Nanoscale Res. Lett. **7**, 534 (2012).

[56] A.K. Kaveev, G.I. Kropotov, E.V. Tsygankova, I.A. Tzibizov, S.D. Ganichev, S.N. Danilov, P. Olbrich, C. Zoth, E.G. Kaveeva, A.I. Zhganov, A.A. Ivanov, R.Z. Deyanov, and B. Redlich, *Terahertz*

*polarization conversion with quartz waveplate sets*, Appl. Optics **52**, B60 (2013).

[57] Ya.V. Terent'ev, C. Zoth, V.V. Bel'kov, P. Olbrich, C. Drexler, V. Lechner, P. Lutz, M.S. Mukhin, S.A. Tarasenko, A.N. Semenov, V.A. Solov'ev, I.V. Sedova, G.V. Klimko, T.A. Komissarova, S.V. Ivanov, and S.D. Ganichev, *Exchange interaction of electrons with Mn in hybrid AlSb/InAs/ZnMnTe structures*, Appl. Phys. Lett. **99**, 072111 (2011).

[58] C. Drexler, V.V. Bel'kov, B. Ashkinadze, P. Olbrich, C. Zoth, V. Lechner, Ya.V. Terent'ev, D.R. Yakovlev, G. Karczewski, T. Wojtowicz, D. Schuh, W. Wegscheider, and S.D. Ganichev, *Spin polarized electric currents in semiconductor heterostructures induced by microwave radiation*, Appl. Phys. Lett. **97**, 182107 (2010).

[59] V.Ya. Aleshkin, V.I. Gavrilenko, A.V. Ikonnikov, S.S. Krishtopenko, Yu.G. Sadofev, and K.E. Spirin, *Exchange Enhancement of the g Factor in InAs/AlSb Heterostructures*, Semicond. **42**, 828 (2008).

[60] G.A. Khodaparast, M.A. Zudov, J. Kono, Y.H. Matsuda, T. Ikaida, S. Ikeda, N. Miura, T. Slupinski, A. Oiwa, H. Munekata, G.D. Sanders, Y. Sun, and C.J. Stanton, *Cyclotron Resonance of Electrons and Holes in Paramagnetic and Ferromagnetic InMnAs-Based Films and Heterostructures*, J. Supercond. **16**, 107 (2003).

[61] Yu.G. Sadofyev, A. Ramamoorthy, B. Naser, J.P. Bird, S.R. Johnson, and Y.-H. Zhang, *Large g-factor enhancement in high-mobility InAs/AlSb quantum wells*, Appl. Phys. Lett. **81**, 1833 (2002).

[62] G.D. Sanders, Y. Sun, F.V. Kyrychenko, C.J. Stanton, M.A. Zudov G.A. Khodaparast, J. Kono, Y.H. Matsuda, N. Miura, and H. Munekata, *Electronic states and cyclotron resonance in n-type InMnAs*, Phys. Rev. B **68**, 165205 (2003).

[63] S.D. Ganichev, S.A. Tarasenko, V.V. Bel'kov, P. Olbrich, W. Eder, D.R. Yakovlev, V. Kolkovsky, W. Zaleszczyk, G. Karczewski, T. Wojtowicz, and D. Weiss, *Spin Currents in Diluted Magnetic Semiconductors*, Phys. Rev. Lett. **102**, 156602 (2009).

[64] S.A. Tarasenko, *Electron scattering in quantum wells subjected to an in-plane magnetic field*, Phys. Rev. B **77**, 085328 (2008).

[65] S. Stachel, P. Olbrich, C. Zoth, U. Hagner, T. Stangl, C. Karl, P. Lutz, V.V. Bel'kov, S.K. Clowes, T. Ashley, A.M. Gilbertson, and S.D. Ganichev, *Interplay of spin and orbital magnetogyrotropic photogalvanic effects in InSb/(Al,In)Sb quantum well structures*, Phys. Rev. B **85**, 045305 (2013).

[66] H. Diehl, V.A. Shalygin, L.E. Golub, S.A. Tarasenko, S.N. Danilov, V.V. Bel'kov, E.G. Novik, H. Buhmann, C. Brüne, L.W. Molenkamp, E.L. Ivchenko, and S.D. Ganichev, *Nonlinear magnetogyrotropic photogalvanic effect*, Phys. Rev. B **80**, 075311 (2009).

[67] E.L. Ivchenko, *Optical Spectroscopy of Semiconductor Nanostructures*. Alpha Science, Harrow, 2005.

[68] Z.D Kvon, S.N. Danilov, N.N. Mikhailov, S.A. Dvoretsky, W. Prettl, and S.D. Ganichev, *Cyclotron resonance photoconductivity of a two-dimensional electron gas in HgTe quantum wells*, Physica E **40**, 1885 (2008).

[69] K.S. Novoselov, A.K. Geim, S.V. Morozov, D. Jiang, M.I. Katsnelson, I.V. Grigorieva, S.V. Dubonos, and A.A. Firsov, *Two-dimensional gas of massless Dirac fermions in graphene*, Nature **438**, 197 (2005).

[70] A.H. Castro Neto, F. Guinea, N.M.R. Peres, K.S. Novoselov, and A.K. Geim, *The electronic properties of graphene*, Rev. Mod. Phys. **81**, 109 (2009).

[71] F.D.M. Haldane, *Model for a Quantum Hall Effect without Landau Levels: Condensed-Matter Realization of the "Parity Anomaly"*, Phys. Rev. Lett. **61**, 2015 (1988).

[72] V.P. Gusynin and S.G. Sharapov, *Magnetic oscillations in planar systems with the Dirac-like spectrum of quasiparticle excitations. II. Transport properties*, Phys. Rev. B **71**, 125124 (2005).

[73] S. Masubuchi, M. Onuki, M. Arai, T. Yamaguchi, K. Watanabe, T. Taniguchi, and T. Machida, *Photovoltaic infrared photoresponse of the high-mobility graphene quantum Hall system due to cyclotron resonance*, Phys. Rev. B **88**, 121402(R) (2013).

[74] K.E. Spirin, A.V. Ikonnikov, A.A. Lastovkin, V.I. Gavrilenko, S.A. Dvoretskii, and N.N. Mikhailov, *Spin Splitting in HgTe/CdHgTe (013) Quantum Well Heterostructures*, JETP Lett. **92**, 63 (2010).

[75] A. Pfeuffer-Jeschke, F. Goschenhofer, S.J. Cheng, V. Latussek, J. Gerschütz, C.R. Becker, R.R. Gerhardts, and G. Landwehr, *Cyclotron masses of asymmetrically doped HgTe quantum wells*, Physica B **256-258**, 486 (1998).

[76] C. Brüne, C.X. Liu, E.G. Novik, E.M. Hankiewicz, H. Buhmann, Y.L. Chen, X.L. Qi, Z.X. Shen, S.C. Zhang, and L.W. Molenkamp, *Quantum hall effect from the topological surface states of strained bulk HgTe*, Phys. Rev. Lett. **106**, 126803 (2011).

[77] X.C. Zhang, K. Ortner, A. Pfeuffer-Jeschke, C.R. Becker, and G. Landwehr, *Two-dimensional gas of massless Dirac fermions in graphene*, Phys. Rev. B **69**, 115340 (2004).

[78] P. Olbrich, J. Allerdings, V.V. Bel'kov, S.A. Tarasenko, D. Schuh, W. Wegscheider, T. Korn, C. Schüller, D. Weiss, and S.D. Ganichev, *Magnetogyrotropic photogalvanic effect and spin dephasing in (110)-grown GaAs/AlGaAs quantum well structures*, Phys. Rev. B **79**, 245329 (2009).

[79] Z.D. Kvon, D.A. Kozlov, S.N. Danilov, C. Zoth, P. Vierling, S. Stachel, V.V. Bel'kov, A.K. Bakarov, D.V. Dmitriev, A.I. Toropov, and S.D. Ganichev, *Terahertz Radiation-Induced Magnetoresistance Oscillations of a High-Density and High-Mobility Two-Dimensional Electron Gas*, JETP Lett. **97**, 41 (2013).

[80] M. Pakmehr, A. Stier, B.D. McCombe, C. Brüne, H. Buhmann, and L. Molenkamp, *THz magnetophotoresponse and spin-orbit effects in the 2DEG in a HgTe quantum well*, Proc. of EP2DS **20**, ThOE13 (2013).

[81] M. Pakmehr, B.D. McCombe, O. Chiatti, S. Buchholz, S. Fischer, C. Heyn, and W. Hansen, *Effective g-factors in InAs 2DEGs from THz magneto-photoresponse*, Proc. of EP2DS **20**, ThP140 (2013).

[82] I.A. Dmitriev, A.D. Mirlin, D.G. Polyakov, and M.A. Zudov, *Nonequilibrium phenomena in high Landau levels*, Rev. Mod. Phys. **84**, 1709 (2012).

[83] M.G. Vavilov and I.L. Aleiner, *Magnetotransport in a two-dimensional electron gas at large filling factors*, Phys. Rev. B **69**, 035303 (2004).

[84] N.S. Averkiev, L.E. Golub, S.A. Tarasenko, and M. Willander, *Theory of magneto-oscillation effects in quasi-two-dimensional semiconductor structures*, J. Phys. Cond. Matt. **13**, 2517 (2001).

[85] Yu.A. Bychkov, *The influence of impurities on the de Haas-van Alphen effect*, JETP **12**, 971 (1961).

[86] S.A. Tarasenko, *The Effect of Zeeman Splitting on Shubnikov-De Haas Oscillations in Two-Dimensional Systems*, Phys. Sol. State **44**, 1769 (2002).

[87] I.A. Dmitriev, A.D. Mirlin, and D.G. Polyakov, *Cyclotron-Resonance Harmonics in the ac Response of a 2D Electron Gas with Smooth Disorder*, Phys. Rev. Lett. **91**, 226802 (2003).

[88] O.E. Raichev, *Magnetic oscillations of resistivity and absorption of radiation in quantum wells with two populated subbands*, Phys. Rev. B **78**, 125304 (2008).

[89] E.R. Brown, M.J. Wengler, and T.G. Phillips, *Absolute response and noise equivalent power of cyclotron resonanceassisted InSb detectors at submillimeter wavelengths*, J. Appl. Phys. **58**, 2051 (1985).

# Acknowledgment